CARRIER DYNAMICS IN SILICON AND GERMANIUM NANOCRYSTALS

A DISSERTATION SUBMITTED TO
THE DEPARTMENT OF PHYSICS
AND THE INSTITUTE OF ENGINEERING AND SCIENCE
OF BILKENT UNIVERSITY
IN PARTIAL FULFILLMENT OF THE REQUIREMENTS
FOR THE DEGREE OF
DOCTOR OF PHILOSOPHY

By
Cem Sevik
January, 2008

I certify that I have read this thesis and that in my opinion it is fully adequate, in scope and in quality, as a dissertation for the degree of doctor of philosophy.

Assist. Prof. Dr. Ceyhun Bulutay(Supervisor)

I certify that I have read this thesis and that in my opinion it is fully adequate, in scope and in quality, as a dissertation for the degree of doctor of philosophy.

Prof. Dr. Atilla Aydınlı

I certify that I have read this thesis and that in my opinion it is fully adequate, in scope and in quality, as a dissertation for the degree of doctor of philosophy.

Prof. Dr. Raşit Turan

I certify that I have read this thesis and that in my opinion it is fully adequate, in scope and in quality, as a dissertation for the degree of doctor of philosophy.

Assoc. Prof. Dr. Resul Eryiğit

I certify that I have read this thesis and that in my opinion it is fully adequate, in scope and in quality, as a dissertation for the degree of doctor of philosophy.

Assoc. Prof. Dr. Oğuz Gülseren

Approved for the Institute of Engineering and Science:

Prof. Dr. Mehmet B. Baray
Director of the Institute

ABSTRACT

CARRIER DYNAMICS IN SILICON AND GERMANIUM NANOCRYSTALS

Cem Sevik
PhD. in Physics
Supervisor: Assist. Prof. Dr. Ceyhun Bulutay
January, 2008

This is a computational work on the Si and Ge nanocrystals (NCs) embedded in wide band gap host matrices. As the initial task, extensive *ab initio* work on the structural and electronic properties of various NC host matrices, namely, SiO_2, GeO_2, Si_3N_4, and Al_2O_3 are preformed. The structural parameters, elastic constants, static and optical dielectric constants are obtained in close agreement with the available results. Furthermore, recently reported high density cubic phase of SiO_2 together with GeO_2 and SnO_2 are studied and their stable high-dielectric constant alloys are identified.

Based on the *ab initio* study of host matrices, two related high field phenomena, vital especially for the electroluminescence in Si and Ge NCs, are examined. These are the hot carrier transport through the SiO_2 matrix and the subsequent quantum-confined impact ionization (QCII) process which is responsible for the creation of electron-hole pairs within the NCs. First, the utility and the validity of the *ab initio* density of states results are demonstrated by studying the high field carrier transport in bulk SiO_2 up to fields of 12 MV/cm using the ensemble Monte Carlo technique. Next, a theoretical modeling of the impact ionization of NCs due to hot carriers of the bulk SiO_2 matrix is undertaken. An original expression governing the QCII probability as a function of the energy of the hot carriers is derived.

Next, using an atomistic pseudopotential approach the electronic structures for embedded Si and Ge NCs in wide band-gap matrices containing several thousand atoms are employed. Effective band-gap values as a function of NC diameter reproduce very well the available experimental and theoretical data. To further check the validity of the electronic structure on radiative processes, direct photon emission rates are computed. The results for Si and Ge NCs as a function of diameter are in excellent agreement with the available *ab initio* calculations for small NCs.

In the final part, non-radiative channels, the Auger recombination (AR) and carrier multiplication (CM) in Si and Ge NCs are investigated again based on the atomistic pseudopotential Hamiltonian. The excited electron and excited hole type AR and CM and biexciton type AR lifetimes are calculated for different sized and shaped NCs embedded in SiO_2 and Al_2O_3. Asphericity is also observed to increase the AR and CM rates. An almost monotonous size-scaling and satisfactory agreement with experiment for AR lifetime is obtained considering a realistic interface region between the NC core and the host matrix. It is further shown that the size-scaling of AR can simply be described by slightly decreasing the established bulk Auger constant for Si to 1.0×10^{-30}cm^{6}s^{-1}. The same value for germanium is extracted as 1.5×10^{-30}cm^{6}s^{-1} which is very close to the established bulk value. It is further shown that both Si and Ge NCs are ideal for photovoltaic efficiency improvement via CM due to the fact that under an optical excitation exceeding twice the band gap energy, the electrons gain lion's share from the total excess energy and can cause a CM. Finally, the electron-initiated CM is predicted to be enhanced by couple orders of magnitude with a 1 eV of excess energy beyond the CM threshold leading to subpicosecond CM lifetimes.

Keywords: Si and Ge Nanocrystals, High-Field Transport, Radiative Recombination, Auger Recombination, Carrier Multiplication, Quantum Confined Impact Ionization, Electronic Structure, High-k Oxides.

ÖZET

SİLİSYUM VE GERMANYUM NANOÖRGÜLERDE TAŞIYICI DİNAMIĞİ

Cem Sevik
Fizik, Doktora
Tez Yöneticisi: Yard. Doç. Dr. Ceyhun Bulutay
Ocak, 2008

Bu çalışma, Si ve Ge nanoörgülerin (NÖ'lerin) sayısal hesaplamaları hakkındadır. Başlangıç olarak SiO_2, GeO_2, Si_3N_4, Ge_3N_4 ve Al_3O_3 gibi NÖ matrislerinin elektronik ve yapısal özellikleri temel prensipler yöntemiyle incelenmiştir. Bunun sonucunda, yapısal özellikler, elastik sabitler, statik ve optik dielektrik sabitler için mevcut çalışmalar ile oldukça uyumlu değerler elde edilmiştir. Ayrıca, SiO_2'nun henüz yayımlanmış yüksek yoğunluklu kübik fazı GeO_2 ve SnO_2 da ele alınarak calışılmış ve bu malzemelerin yüksek dielektrik sabitli duragan alaşım formları elde edilmiştir.

NÖ matrisleri hakkındaki temel ilkeler hesaplamalarına dayanarak, Si ve Ge NÖ'lerdeki elektronışıması için oldukça önemli olan iki yüksek elektrik alan olgusu incelenmiştir. Bu olgular, SiO_2 matrisi içerisinde yüksek enerjili yük taşınımı ve NÖ içinde elektron-deşik çiftlerinin oluşumunda rolü olan kuvantum tuzaklı darbe iyonizasyonudur (KTDI). İlk olarak, temel ilkeler yöntemiyle hesaplanmış durum yoğunluklarının geçerliliğini ve yararlılığını test etmek amacı ile SiO_2 yüksek enerjili tasıyıcı taşınımı 12 MV/cm elektrik alan değerine kadar Toplu Monte Carlo yöntemi ile tetkik edilmiştir. Daha sonra, yığık SiO_2 içerisindeki yüksek enerjili taşıyıcılar tarafından tetiklenen NÖ darbe iyonizasyonunun teorik bir modellemesi ele alınmıştır. Neticede, NÖ içerisinde KTDI oranını yüksek enerjili taşıyıcıların enerjisinin bir fonksiyonu olarak veren orjinal bir ifade türetilmiştir.

Daha sonra, geniş-bant aralıklı yarıiletkenler içerisine gömülü, birkaç bin atomdan oluşan, Si ve Ge NÖ'lerin elektronik yapısı atomistik görünürpotansiyel yöntemi ile çalışılmıstır. NÖ çapının fonksiyonu olarak hesaplanmış etkin bant aralığı değerlerinin mevcut deneysel ve teorik sonuçlar ile oldukça uyumlu olduğu görülmüştür. Elektronik yapının radyasyonlu ışıma üzerindeki etkisini belirlemek amacı ile direk foton yayma oranları hesaplanmış ve hem Si hem de Ge için mevcut temel ilkeler veriler ile son derece benzer sonuçlar elde edilmiştir.

NÖ'nün çekirdek bölgesi ile matris arasındaki arayüzün gerçekçi bir şekilde modellenmesi, yarıçapa göre neredeyse yeknesak artan ve deney ile hemen hemen uyumlu sonuçlar elde etmemizi sağlamıştır. Ayrıca, Si NÖ'ler için yarıçapa göre Auger geribirleşimi yaşam süresi'nin, yığık örgü Auger sabitini $1.0\times10^{-30}\text{cm}^6\text{s}^{-1}$ alarak basit bir şekilde elde edilebileceği gösterilmiş ve Ge için bu değer $1.5\times10^{-30}\text{cm}^6\text{s}^{-1}$ olarak saptanmıştır. NÖ bant aralığından iki kat fazla optik aydınlatma altında, elektronların uyarma enerjisinin arslan payını alarak iletkenlik bandına geçtiği saptanmış ve bu elektronların tetiklediği taşıyıcı katlanması yaşam sürelerinin hesaplanması sonucunda, bu iki NÖ'nun fotovoltaik uygulamalarda verimliliği arttırma amaçlı kullanımının çok uygun olduğu gözlenmiştir. Son olarak, uyarılma enerjisinin eşik değerinin yanlızca 1 eV üzerinde TK oranının oldukça yükseldiği ve yaşam süresinin birkaç-picosaniye değerlerine kadar gerilediği görülmüştür.

Anahtar sözcükler: Si ve Ge Nanoörgüleri, Yüksek Elektrik Alanı Altında Taşınım, Radyasyonlu Işıma, Auger Geribirleşimi, Taşıyıcı Katlanması, Kuvantum Tuzak Darbe İyonizasyonu, Elektronik Yapı, Yüksek-k Oksitler.

Acknowledgement

I would like to express my gratitude to my supervisor Assist. Prof. Dr. Ceyhun Bulutay for not only his instructive comments in the supervision of my thesis but also constitutive contrubution to my life and my personality.

I would like to thank Prof. R. Eryiğit, T. Gürel, Prof. O. Gülseren, D. Çakır and Dr. T. Yıldırım for their useful advices for *ab initio* studies. This work has been supported by the European FP6 Project SEMINANO with the contract number NMP4 CT2004 505285 and by the Turkish Scientific and Technical Council TÜBİTAK with the project number 106T048. The computations were performed in part by the TR-Grid e-Infrastructure Project of TÜBİTAK.

I would also like to thank to Prof. Raşit Turan and Prof. Atilla Aydınlı for their useful supports during the SEMINANO project.

I am very happy and proud of making wonderful friends in Bilkent University, I will always remember them.

I am very grateful for my wife Olcay, for her love and patience during the PhD period.

To my wife and mom.

Contents

List of Figures

List of Tables

Chapter 1

Introduction

Due to its indirect band gap bulk silicon is a very inefficient emitter, even at liquid helium temperatures. Within the last decade several approaches were developed towards improving the efficiency of light emission from Si-based structures. In spirit, all were based on the lifting of the lattice periodicity that introduces an uncertainty in the k-space and therefore altering the indirect nature of this material. Some examples are: SiGe or Si-SiO_2 superlattices [1, 2] or Si nanocrystal (NC) assemblies [3] (see Fig. 1.1). Recently, intensive electroluminescence (EL) from Si implanted SiO_2 [4] and Si implanted sapphire [5] layers were observed. Besides, EL from Ge-implanted SiO_2 [6, 7] layers and Ge implanted SiN_x [8] layers were also predicted. Applications of NC-based structures in laser emitters, [9, 10, 11, 12] EL devices, [13, 14] switching elements, [15] and solar batteries [16] have been announced in the recent past. Moreover, the search for new-generation photovoltaics has gained momentum and hence the subject of direct photon absorption in NCs [17] is of prime interest. The largest quantum yield that has been achieved under optical excitation of Si NCs is of the order of 50% and is already comparable with that of direct band-gap quantum dots assemblies.

In spite of these exciting properties of NCs, their transport and emission mechanisms are still unclear. A theoretical understanding of these exciting properties first of all requires a detailed and accurate electronic structure tool which can then be used to predict certain optoelectronic properties as well as other

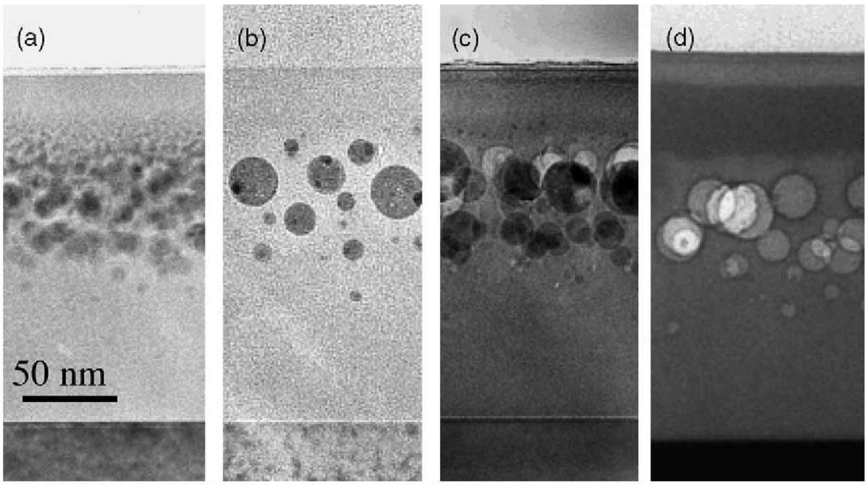

Figure 1.1: TEM micrographs of SiO_2 films implanted with a fluence of 1×10^{17} Ge ions cm^{-2} after annealing for at 1000 °C for (a) 15 min, (b) 30 min, (c) 45 min and (d) 60 min, obtained by E. S. Marstein *et al.* [18]

quantum processes such as quantum confined impact ionization (QCII), Auger recombination (AR) and carrier multiplication (CM). However, such a task becomes formidable in the case of NCs: the *ab initio* approaches [19] are currently out of consideration as there are 1,000-20,000 atoms within the active region of these structures. On the other hand the standard multiband $\mathbf{k}\cdot\mathbf{p}$ approaches [20] are neither accurate for NCs nor applicable directly to indirect band-gap semiconductors such as in Si and Ge based NCs. Based on these facts, the most useful method to search NCs is the recently proposed linear combination of bulk bands (LCBB) recipe by the Zunger group from NREL (USA) [21, 22]. The LCBB has been used for self-assembled quantum dots [23, 22], superlattices [24, 25] and high-electron mobility transistors [26], and very recently on the aggregation of Si NCs [27].

Quantum processes such as radiative recombination, QCII, AR and CM have strong effect on carrier dynamics, emission and absorption mechanisms in NCs. One of the most important one especially responsible for exciton generation in quantum dots and NCs is the QCII. This process is responsible for the introduction of confined excitons in silicon NC devices which is a key luminescence mechanism. Another important processes AR and CM are responsible for the nonradiative annihilation and creation of confined excitons in NCs. The rate of these two processes affects many aspects of the performance of nanoscale devices. The latter has been demonstrated in a very recent experimental study by significantly increasing the solar cell efficiency in colloidal Si NCs due to CM which enables multiple exciton generation in response to a single absorbed photon [28]. Similarly, the inverse process, AR is also operational and it introduces a competing mechanism to CM which can potentially diminish the solar cell efficiency and in the case of light sources it degrades the performance by inflating the nonradiative carrier relaxation rate [29]. A recent paper by Trojánek *et al.* [30] reports that the photoluminescense decay time for Si NC is about 105 ps. This is the characteristic time scale for the nonradiative AR process. As it is significantly shorter than the time of the radiative emission (approximately 20 to 30 nanoseconds [31, 32]), its main implication is that AR should inhibit the NC laser, LED operations. Without any doubt, it is also detrimental for solar cell applications as the created electron-hole pairs disappear without contributing to the photocurrent.

1.1 This Work

Aiming for a clear and realistic characterization of the fundamental processes such as QCII, AR and CM in embedded Si and Ge NCs, first we start with the *ab initio* calculations of electronic and structural properties of the NC host matrices. Our analysis includes wide band-gap crystalline oxides and nitrides such as SiO_2 (α-quartz, α- and β-cristobalite and stishovite), GeO_2 (α-quartz, and rutile) Al_2O_3 (α-phase), Si_3N_4 (α- and β-phases), and Ge_3N_4 (α- and β-phases). Electronic structure and the elastic properties of these important insulating oxides and nitrides are obtained with high accuracy based on density functional theory within the local density approximation. We also perform detailed calculations about new high-k cubic phase of SiO_2, GeO_2, SnO_2 and their ternary alloys. This part of the thesis work has been published in Journal of Material Science [33], Physical Review B [34] and Materials Sciences in Semiconductor Processing [35].

Next, in Chapter 3, we start by characterizing the hot electron transport in oxides within the ensemble Monte Carlo (EMC) framework including all major scattering mechanism such as acoustic, polar and non-polar optical phonon scatterings. Afterwards, we derive an analytical expression for the QCII probability in NCs that can become an instrumental result in assessing EL in the presence of other competing scattering mechanisms. The effect of QCII on bulk transport quantities is also discussed. This part of the thesis work has been published in Physica E [36] and Physica Status Solidi C [37].

In Chapter 4, embedded Si and Ge NCs in wide band-gap matrices are studied theoretically using an atomistic pseudopotential approach. From small clusters to large NCs containing on the order of several thousand atoms are considered. The energy spectrum and real-space wavefunctions of each state are produced and employed in the calculation of the AR and CM. For the comparison purposes with the nonradiative processes, radiative recombination lifetime for Si and Ge NCs as a function of diameter are computed. Our results are in excellent agreement with the very reliable *ab initio* calculations which is only available for small NCs [38].

Finally in Chapter 5, we provide an atomistic theoretical account of CM and AR in *embedded* Si and Ge NCs which reveals their size, shape and host matrix dependence. Unlike most previous treatments, the NCs are considered to be embedded into different wide band-gap host matrices. The electron- and hole-initiated types of AR and CM and biexciton-type of AR are considered based on an atomistic pseudopotential model. This part of the thesis work has been submitted to Physical Review B as a Rapid Communication.

Chapter 6 contains our conclusions and main achievements in this thesis. The two Appendix sections at the end provide the technical details of the theoretical derivations on the QCII and related bulk carrier-initiated Coulombic excitations and give some background information and further theoretical details on AR in the bulk and NCs. Extensive literature survey on each individual topic is given at the beginning of each chapter. Special emphasis is given to the comparison of our results with the experimental and theoretical data, whenever possible.

Chapter 2

Ab initio Study of the Nanocrystal Host Crystal Lattices

To completely investigate the electronic and transport properties of embedded Si and Ge nanocrystals (NCs) it is obligatory to have a thorough mastering of the host matrices into which these NCs are embedded. Therefore as a first part of the thesis, we performed an extensive theoretical study for NC host matrices which are wide bandgap crystalline oxides and nitrides, namely, SiO_2, GeO_2, Al_2O_3, Si_3N_4, and Ge_3N_4. In addition to the NC host matrices we also considered the recently reported inverse silver oxide phase of SiO_2 that possesses a high dielectric constant (high-k) as well as lattice constant compatibility to Si. Moreover, we explored the closely-related oxides, GeO_2, SnO_2 and their alloy formations with the same inverse silver oxide structure. The details of these two studies are presented in this Chapter collocated as follows: in Sec. 2 we provide details of our *ab initio* computations and our first-principles results for the structural, electronic properties of the NC host lattices, Sec. 3 includes the same details about high-k inverse silver oxide structures.

2.1 *Ab initio* study of the nanocrystal host crystal lattices

As the first task of the thesis, we performed an extensive *ab initio* study for NC host matrices which are wide bandgap crystalline oxides and nitrides, namely, SiO_2, GeO_2, Al_2O_3, Si_3N_4, and Ge_3N_4. Their important polymorphs are considered which are for SiO_2: α-quartz, α- and β-cristobalite and stishovite, for GeO_2: α-quartz, and rutile, for Al_2O_3: α-phase, for Si_3N_4 and Ge_3N_4: α- and β-phases (see Fig. 2.1). This Chapter presents a comprehensive account of both electronic structure and the elastic properties of these important insulating oxides and nitrides obtained with high accuracy based on density functional theory within the local density approximation. Two different norm-conserving *ab initio* pseudopotentials have been tested and shown to agree in all respects with the only exception arising for the elastic properties of rutile GeO_2. The agreement with experimental values, when available, is seen to be highly satisfactory. The uniformity and the well convergence of this approach enable an unbiased assessment of important physical parameters within each material and among different insulating oxide and nitrides. The computed static electric susceptibilities are observed to display a strong correlation with their mass densities. There is a marked discrepancy between the considered oxides and nitrides with the latter having sudden increase of density of states away from the respective band edges. This is expected to give rise to excessive carrier scattering which can practically preclude bulk impact ionization process in Si_3N_4 and Ge_3N_4.

2.1.1 Introduction

Insulating oxides and nitrides are indispensable materials for diverse applications due to their superior mechanical, thermal, chemical and other outstanding high temperature properties. Furthermore, in the electronic industry these wide band gap materials are being considered for alternative gate oxides [39] and in the field of integrated optics they provide low-loss dielectric waveguides [40]. Recently the subject of wide bandgap oxides and nitrides have gained interest within the context of nanocrystals which offer silicon-based technology for light emitting devices and semiconductor memories [14]. These nanocrystals are embedded in an insulating matrix which is usually chosen to be silica [41, 42, 43, 44]. However, other wide bandgap materials are also employed such as germania [45, 46], silicon nitride [47, 48, 49], and alumina [50, 51, 52]. As a matter of fact, the effect of different host matrices is an active research topic in this field.

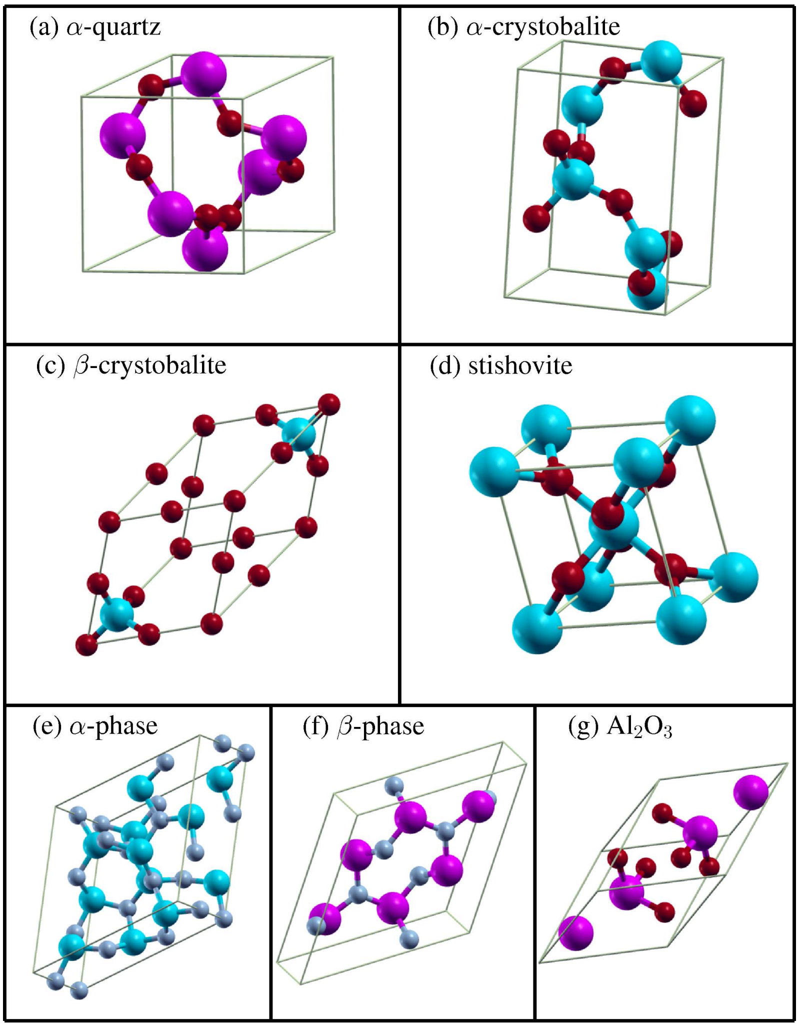

Figure 2.1: Ball and stick model of (a) α-quartz XO_2, (b) α-crystobalite XO_2, (c) β-crsytobalite XO_2, (d) stishovite XO_2, (e) α-phase X_3N_4, (f) β-phase X_3N_4, and (g) Al_2O_3. X refers to Si or Ge.

Among these insulating oxides and nitrides technologically most important ones are SiO_2, Al_2O_3, Si_3N_4. The activity around GeO_2 is steadily increasing. Another closely-related material, Ge_3N_4 has attracted far less attention up to now even though it has certain interesting properties [53]. The major obstacle has been the sample growth. However, a very recent study reported an *in situ* Ge_3N_4 growth on Ge, demonstrating high thermal stability and large band offsets with respect to the Ge system [54]. In our comprehensive treatment, we present the *ab initio* structural and electronic properties of all these materials considering their common polymorphs; these are for SiO_2: α-quartz, α- and β-cristobalite and stishovite phases, for GeO_2: α-quartz, and rutile phases, for Si_3N_4 and Ge_3N_4: α- and β-phases and for Al_2O_3: α-phase. For amorphous and inherently imperfect matrices, these perfect crystalline phases serve as important reference systems. Moreover, due to their distinct advantages, *epitaxial* host lattices are preferred over the amorphous ones for specific applications.

With an eye on these technological applications, we focus on several physical properties of these lattices. The elastic constants play an important role on the strain profile of the embedded core semiconductor. Using Eshelby's continuum elastic consideration [55] the radial and tangential stress fields of the nanocrystal can be determined [56]; these in turn, affect the optical properties [43]. The static and optical dielectric constants of these lattices introduce nontrivial local field effects that modify the absorption spectra of an isolated nanocrystal when embedded inside one of these matrices [57]. Based on the simple effective medium theory which has been tested by *ab initio* calculations [58], one can assess which host lattice and nanocrystal combination would possess the desired optical properties. Because of the dielectric mismatch between the nanocrystal core and the surrounding lattice, image charges will be produced [59]. These image charges should be taken into account in characterizing nanocrystal excitons [3]. Another promising application is the visible and near infrared electroluminescence from Si and Ge nanocrystals [14]. The electroluminescence is believed to be achieved by the recombination of the electron hole pairs injected to nanocrystals under high bias [14]. In this context the bulk state impact ionization process which can also give rise to electroluminescence is considered to be detrimental leading to dielectric breakdown.

For high-field carrier transport, the crucial physical quantity was identified to be the valence and conduction band density of states (DOS) for each of the crystalline polymorph [60]. Based on these technology-driven requirements we compute the elastic constants, band structures, dielectric permittivities and electronic DOS of these aforementioned crystal polymorphs. Our *ab initio* framework is based on the density functional theory [61, 62], using pseudopotentials and a plane wave basis [19]. With the exception of Ge_3N_4 which was far less studied, vast amount of theoretical work is already available spread throughout the literature based on a variety of techniques [63, 64, 65, 66, 67, 68, 69, 70, 71, 72]. Our first-principles study here enables a uniform comparison of important physical parameters within each material and among different insulating oxides and nitrides.

2.1.2 Details of *Ab initio* Computations

Structural and electronic properties of the polymorphs under consideration have been calculated within the density functional theory [61, 62], using the plane wave basis pseudopotential method as implemented in the ABINIT code [19][1]. The results are obtained under the local density approximation (LDA) where for the exchange-correlation interactions we use the Teter-Pade parameterization [73], which reproduces Perdew-Zunger [74] (which reproduces the quantum Monte Carlo electron gas data of Ceperley and Alder [75]). We tested the results under two different norm-conserving Troullier and Martins [76] type pseudopotentials, which were generated by A. Khein and D.C. Allan (KA) and Fritz Haber Institute (FHI). For both pseudopotentials, the valence configurations of the constituent atoms were chosen as N($2s^2p^3$), O($2s^2p^4$), Al($3s^23p^1$), Si($3s^23p^2$), and Ge($4s^24p^2$). The number of angular momenta of the KA (FHI) pseudopotentials and the chosen local channel were respectively, for N: 1, p (3, d), for O: 1, p (3, d), for Al: 2, d (3, d), for Si: 2, d (3, d), and for Ge: 1, p (3, s). Our calculated values for these two types of pseudopotentials were very similar, the only exceptional case being the elastic constants for rutile GeO_2. Dielectric permitivity and the

---

[1] We are grateful to Prof. R. Eryiğit for his valuable technical guidance with ABINIT.

fourth-order tensor of elastic constants of each crystal are determined by starting from relaxed unit cell under the application of finite deformations within density functional perturbation theory [77] as implemented in ABINIT and ANADDB extension of it. Another technical detail is related with the element- and angular momentum-resolved partial density of states (PDOS). To get a representative PDOS behavior we need to specify the spherical regions situated around each relevant atomic site. The radii of these spheres are chosen to partition the bond length in proportion to the covalent radii of the constituent atoms. This resulted in the following radii: for the α-quartz SiO_2, $r_{Si} = 0.97$ Å, $r_O = 0.65$ Å, for the rutile GeO_2, $r_{Ge} = 1.16$ Å, $r_O = 0.69$ Å, for the α-Al_2O_3, $r_{Al} = 1.32$ Å, $r_O = 0.56$ Å, and for the β-Si_3N_4, $r_{Si} = 1.03$ Å, $r_N = 0.70$ Å. It should be pointed that even though such an approach presents a good relative weight of the elements and angular momentum channels, it inevitably underestimates the total DOS, especially for the conduction bands. Other details of the computations are deferred to the discussion of each crystal polymorph.

2.1.3 First-principles Results

First, we address the general organization and the underlying trends of our results. The lattice constants and other structural informations of all crystals are listed in Table 2.1. Table 2.2 contains the bond lengths and bond angles of the optimized oxide polymorphs. These results can be used to identify the representation of each polymorph within the amorphous oxides [78]. The elastic constants and dielectric permittivity tensor of each crystal are tabulated in Table 2.3 and Table 2.4, respectively. Very close agreement with the existing experimental data and previous calculations can be observed, which gives us confidence about the accuracy and convergence of our work. Employing KA pseudopotentials, the band structure for the crystals are displayed along the high-symmetry lines in Figs. 2.2, 2.4, 2.6, 2.7 together with their corresponding total DOS. Such an information is particlulary useful in the context of high-field carrier transport. These results are in good agreement with the previous computations [64, 71, 70, 67]. For all

---

[1] We are grateful to Prof. O. Gülseren for his valuable technical guidance in this part.

Table 2.1: Structural information on crystals.

Crystal	Crystal Structure	Lattice Constants (Å)	Space Group	Molecules Per Prim. Cell	Density (gr/cm^3)
α-quartz SiO_2	Hexagonal	$a = 4.883^1\ 4.854^2\ 4.913^3$ $c = 5.371^1\ 5.341^2\ 5.405^3$	$P3_221$	3	2.698
α-cris. SiO_2	Tetragonal	$a = 4.950^1\ 4.939^2\ 4.973^3$ $c = 6.909^1\ 6.894^2\ 6.926^3$	$P4_12_12$	4	2.372
β-cris. SiO_2	Cubic	$a = 7.403^1\ 7.330^2\ 7.160^3$	$Fd3m$	2	1.966
Stishovite SiO_2	Tetragonal	$a = 4.175^1\ 4.145^2\ 4.179^4$ $c = 2.662^1\ 2.643^2\ 2.665^4$	$P4_2/mnm$	2	4.298
α-quartz GeO_2	Hexagonal	$a = 4.870^1\ 4.861^2\ 4.984^6$ $c = 5.534^1\ 5.520^2\ 5.660^6$	$P3_221$	3	4.612
Rutile GeO_2	Tetragonal Tetragonal	$a = 4.283^1\ 4.314^2\ 4.4066^7$ $c = 2.782^1\ 2.804^2\ 2.8619^7$	$P4_2/mnm$	2	6.655
α-Al_2O_3	Rombohedral	$a = 4.758^1\ 4.762^5$ $c = 12.98^1\ 12.896^5$	$R\bar{3}c$	2	3.992
α-Si_3N_4	Hexagonal	$a = 7.732^1\ 7.766^9$ $c = 5.603^1\ 5.615^9$	C_{3v}^4	4	3.211
β-Si_3N_4	Hexagonal	$a = 7.580^1\ 7.585^{10}$ $c = 2.899^1\ 2.895^{10}$	C_{6h}^2	2	3.229
α-Ge_3N_4	Hexagonal	$a = 7.985^{\mathrm{a}}$ $c = 5.786^{\mathrm{a}}$	C_{3v}^4	4	5.691
β-Ge_3N_4	Hexagonal	$a = 7.826^{\mathrm{a}}$ $c = 2.993^{\mathrm{a}}$	C_{6h}^2	2	5.727

[a] This Work KA
[b] This Work FHI
[c] Ref. [79]
[d] Ref. [80]
[f] Ref. [81]
[g] Ref. [82, 21]
[e] Ref. [66]
[i] Ref. [67]
[j] Ref. [72]

of the considered polymorphs the conduction band minima occur at the Γ point whereas the valence band maxima shift away from this point for some of the phases making them indirect band gap matrices (see Table 2.5). However, the direct band gap values are only marginally above the indirect band gap values. These LDA band gaps are underestimated which is a renown artifact of LDA for semiconductors and insulators [83]. In this work we do not attempt any correction procedure to adjust the LDA band gap values.

We present in Figs. 2.3, 2.5, 2.8 the element- and angular momentum-resolved PDOS. A common trend that can be observed in these various lattices is that their valence band maxima are dominated by the p states belonging to O atoms; in the case of Si_3N_4 and Ge_3N_4 they are the N atoms. For the conduction band edges, both constituent elements have comparable contribution. This parallels the observation in amorphous SiO_2 where due to large electronegativity difference between Si and O, the bonding orbitals have a large weight on O atoms whereas the lowest conduction band states with antibonding character have a significant contribution from the Si atoms [84].

Table 2.2: Bond lengths and bond angles (in degrees) of SiO_2 and GeO_2 polymorphs where x represents a Si or a Ge atom.

Crystal		x-O (Å)	x-O (Å)	O-x-O	O-x-O	O-x-O	O-x-O	x-O-x	x-O-x
α-quartz SiO_2	This Work	1.613	1.618	110.75	109.32	109.07	108.47	140.55	
	Exp.^{1}	1.605	1.614	110.50	109.20	109.00	108.80	143.7	
α-quartz GeO_2	This Work	1.693	1.699	113.03	110.62	107.94	106.16	130.56	
α-cris. SiO_2	This Work	1.597	1.596	111.59	110.08	109.03	108.02	146.02	
	Exp.^{2}	1.603	1.603	111.40	110.00	109.00	108.20	146.5	
β-cris. SiO_2	This Work	1.603		109.47				180	
	Exp.^{3}	1.611		107.80				180.00	
Stishovite SiO_2	This Work	1.804	1.758	98.47	81.53			130.76	98.47
	Exp.^{4}	1.760	1.810					130.60	
Rutile GeO_2	This Work	1.848	1.824	99.34	80.66			99.34	130.33

[a] Ref. [85]
[b] Ref. [86]
[c] Ref. [87]
[d] Ref. [88]

From another perspective, the band structures and the associated DOS reveal that there is a marked discrepancy between the valence and conduction band edges where for the former there occurs a sharp increase of DOS just below the band edge. As the probabilities of most scattering processes are directly proportional to DOS [89], in the case of high-field carrier transport the electrons should encounter far less scatterings and hence gain much higher energy from the field compared to holes. In this respect Si_3N_4 and Ge_3N_4 are further different from the others where for both conduction and valence bands the DOS dramatically increases (cf. Fig. 2.7) so that the carriers should suffer from excessive scatterings which practically precludes the bulk impact ionization for this material.

Another common trend can be investigated between the density of each polymorph and the corresponding static permittivity, ϵ_s. Such a correlation was put forward by Xu and Ching among the SiO_2 polymorphs [64]. We extend this comparison to all structures considered in this work and rather use $\epsilon_s - 1 = 4\pi\chi_e$ which is propational to the electric susceptibility, χ_e. It can be observed from Fig. 2.9 that the trend established by SiO_2 polymorphs is also followed by β-Si_3N_4

and α-Al_2O_3.

Table 2.3: Elastic constants and bulk modulus for each crystal.

Crystal	(GPa)	C_{11}	C_{12}	C_{13}	C_{14}	C_{33}	C_{44}	C_{66}	B
α-quartz SiO_2	KA	76.2	11.9	11.2	-17.0	101.7	54.0	32.1	35
	FHI	79.5	9.73	9.54	-18.9	101.7	55.5	34.9	35
	Exp.[1]	87.0	7.00	13.0	-18.0	107.0	57.0	40.0	38
	Exp.[2]	87.0	7.00	19.0	-18.0	106.0	58.0		40
α-Cris. SiO_2	KA	49.30	5.26	-11.41		44.78	74.15	26.85	12
β-Cris. SiO_2	KA	194.0	135.0				82.67		155
	FHI	196.1	134.2				85.40		155
Stishovite SiO_2	KA	447.7	211.0	203.0		776.0	252.0	302.0	306
	FHI	448.8	211.1	191.0		752.0	256.5	323.0	302
	Exp.[3]	453.0	211.0	203.0		776.0	252.0	302.0	308
α-quartz GeO_2	KA	66.7	24.3	23.1	-3.00	118.7	41.3	21.2	41
	FHI	63.8	25.7	26.2	-0.81	120.2	35.3	19.1	42
	Exp.[4]	66.4	21.3	32.0	-2.20	118.0	36.8	22.5	42
	Exp.[2]	64.0	22.0	32.0	-2.00	118.0	37.0	21.0	42
Rutile GeO_2	KA	405.9	235.3	189.2		672.4	206.0	314.4	292
	FHI	349.2	197.2	185.1		617.5	171.8	274.8	258
	Exp.[5]	337.2	188.2	187.4		599.4	161.5	258.4	251
α-Al_2O_3	KA	493.0	164.1	130.1		485.8	155.5	164.4	258
	Exp.[6]	497.0	164.0	111.0		498.0	147.0		251
β-Si_3N_4	KA	421.8	197.8	116.6		550.7	100.2	112.0	250
	Exp.[7]	433.0	195.0	127.0		574.0	108.0	119.0	259
	Exp.[8]	439.2	181.8	149.9		557.0	114.4	135.9	265
β-Ge_3N_4	KA	364.3	184.9	111.7		486.3	80.4	89.7	225

[a] Ref. [90]
[b] Ref. [91]
[c] Ref. [92]
[d] Ref. [81]
[e] Ref. [21]
[f] Ref. [93]
[g] Ref. [94]
[h] Ref. [95]

On the other hand, Ge-containing structures while possessing a similar trend among themselves, display a significant shift due to much higher mass of the this atom. This dependence on the atomic mass needs to be removed by finding a more suitable physical quantity. We should mention that such a correlation does not exist between the volume per primitive cell of each phase and the static permittivity. After these general comments, now we concentrate on the results of each lattice individually.

Table 2.4: Dielectric permittivity tensor.

Crystal	$\epsilon^0_{xx} = \epsilon^0_{yy}$	ϵ^0_{zz}	$\epsilon^\infty_{xx} = \epsilon^\infty_{yy}$	ϵ^∞_{zz}
α-quartz SiO_2	4.643	4.847	2.514	2.545
α-cris. SiO_2	4.140	3.938	2.274	2.264
β-cris. SiO_2	3.770	3.770	2.078	2.078
Stishovite SiO_2	10.877	8.645	3.341	3.510
α-quartz GeO_2	5.424	5.608	2.864	2.947
Rutile GeO_2	10.876	8.747	3.679	3.945
α-Al_2O_3	10.372	10.372	3.188	3.188
β-Si_3N_4	8.053	8.053	4.211	4.294
β-Ge_3N_4	8.702	8.643	4.558	4.667

2.1.3.1 SiO_2

The α-quartz SiO_2 is one of the most studied polymorphs as it is the stable phase at ambient pressure and temperature [65, 69], furthermore its short-range order is essentially the same as the amorphous SiO_2 [84]. α-quartz SiO_2 has a hexagonal unit cell containing three SiO_2 molecules. A plane-wave basis set with an energy cutoff of 60 Hartree was used to expand the electronic wave functions at the special k-point mesh generated by 10×10×8 Monkhorst-Pack scheme [96]. The band structure of α-quartz SiO_2 has been calculated by many authors (see, for instance [63, 64]). Our calculated band structure and total DOS shown in Fig. 2.2(a) are in agreement with the published studies [64].

Table 2.5: Indirect (E_g) and direct ($E_g(\Gamma)$) LDA Band Gaps for each crystal.

Crystal	VB Max.	CB Min.	E_g (eV)	$E_g(\Gamma)$ (eV)
α-quartz SiO_2	K	Γ	5.785	6.073
α-cris. SiO_2	Γ	Γ	5.525	5.525
β-cris. SiO_2	Γ	Γ	5.317	5.317
Stishovite SiO_2	Γ	Γ	5.606	5.606
α-quartz GeO_2	K	Γ	4.335	4.434
Rutile GeO_2	Γ	Γ	3.126	3.126
α-Al_2O_3	Γ	Γ	6.242	6.242
α-Si_3N_4	M	Γ	4.559	4.621
β-Si_3N_4	A-Γ	Γ	4.146	4.365
α-Ge_3N_4	M	Γ	3.575	3.632
β-Ge_3N_4	A-Γ	Γ	3.447	3.530

The indirect LDA band gap for this crystal is 5.785 eV from the valence band maximum at K to the conduction band minimum at Γ. The direct LDA band gap at Γ is slightly larger than the indirect LDA band gap as seen in Table 2.5. Calculated values of the elastic constants and bulk modulus listed in Table 2.3 are in good agreement with the experiments. Apart from C_{12}, the elastic constants are within 10% of the experimental values. The discrepancy in C_{12} can be explained by the fact that C_{12} is very soft and this type of deviation also exists among experiments which is also the case for C_{14}.

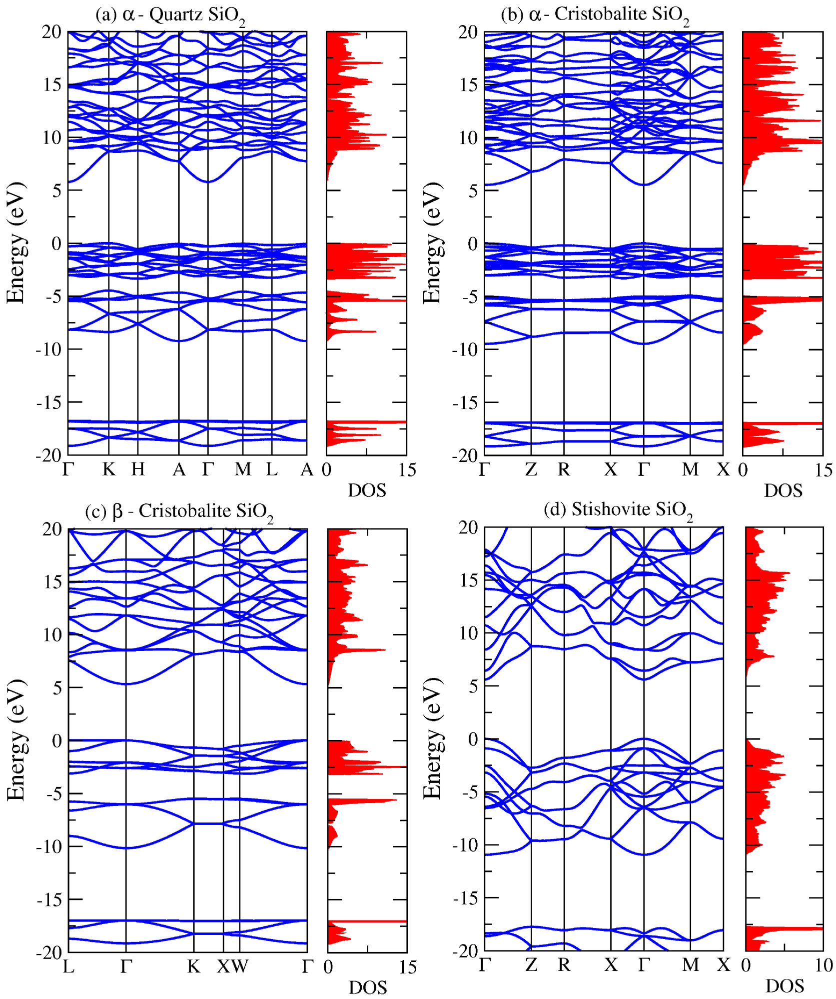

Figure 2.2: LDA band structure and total DOS (electrons/eV cell) of (a) α-cristobalite SiO_2, (b) α-quartz SiO_2, (c) β-cristobalite SiO_2, and (d) stishovite SiO_2.

The α-cristobalite SiO_2 has a tetragonal unit cell containing four SiO_2 molecules. In the course of calculations an absolute energy convergence of 10^{-4} Ha was obtained by setting a high plane wave energy cutoff as 60 Ha and 10×10×8 k-point sampling. Figure 2.2(b) shows the band structure of α-cristobalite SiO_2 with the 5.525 eV direct band gap at Γ. The bulk modulus of 12 GPa is the smallest among all the host lattice polymorphs considered in this work.

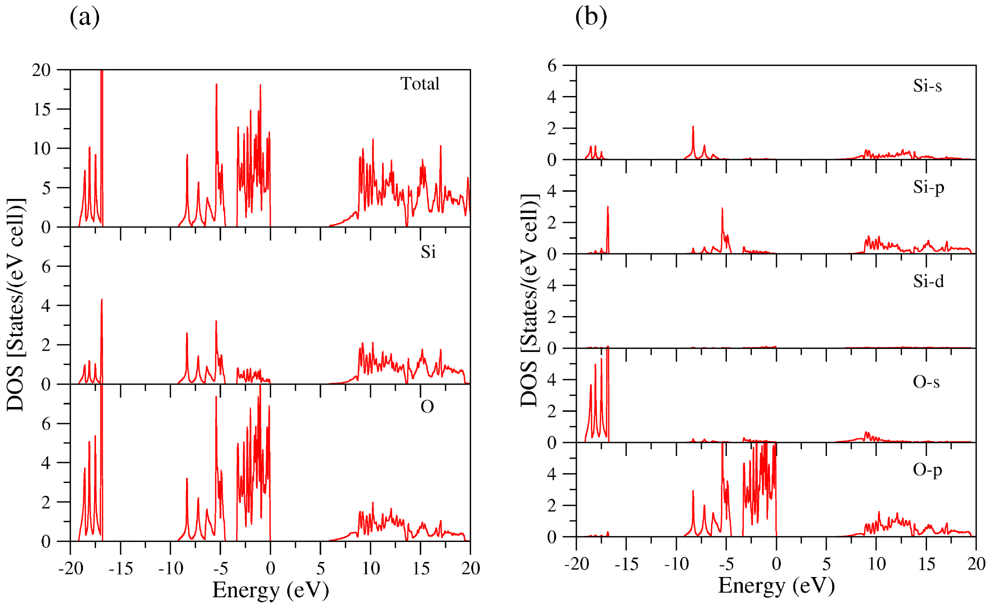

Figure 2.3: DOS of α-quartz SiO_2 (a) Element-resolved; total, PDOS of Si, PDOS of O. (b) Angular momentum-resolved; Si s electrons, Si p electrons, Si d electrons (not visible at the same scale), O s electrons, O p electrons.

Regarding β-cristobalite, its actual structure is somewhat controversial, as a number of different symmetries have been proposed corresponding to space groups $Fd3m$, $I\bar{4}2d$, and $P2_13$ [69]. Recently, incorporating the quasiparticle corrections the tetragonal $I\bar{4}2d$ phase was identified to be energetically most stable [97]. However, we work with the structure having the space group of $Fd3m$ that was originally proposed by Wyckoff [98] and which is widely studied primarily due to its simplicity [63, 65]. This phase has a cubic conventional cell with two molecules. We used 60 Ha plane wave energy cutoff and $10\times10\times10$ k-point sampling. Figure 2.2(c) shows the band structure of β-cristobalite SiO_2 with the 5.317 eV direct band gap at Γ. Unlike their band structures, total DOS of α- and and β-cristobalite SiO_2 are very similar (cf. Fig. 2.2(c)). This similarity can be explained by the fact that their local structures are very close. On the other hand there is a considerable difference between the DOS spectra of the α-quartz SiO_2 and the β-cristobalite SiO_2. In Table 2.3, we present elastic constants of the β-cristobalite SiO_2 calculated by two types of pseudopotentials, FHI and KA. There is no considerable difference between them. Dielectric constants of β-cristobalite SiO_2 are the smallest among the five polymorphs of SiO_2 studied here (see Table 2.4).

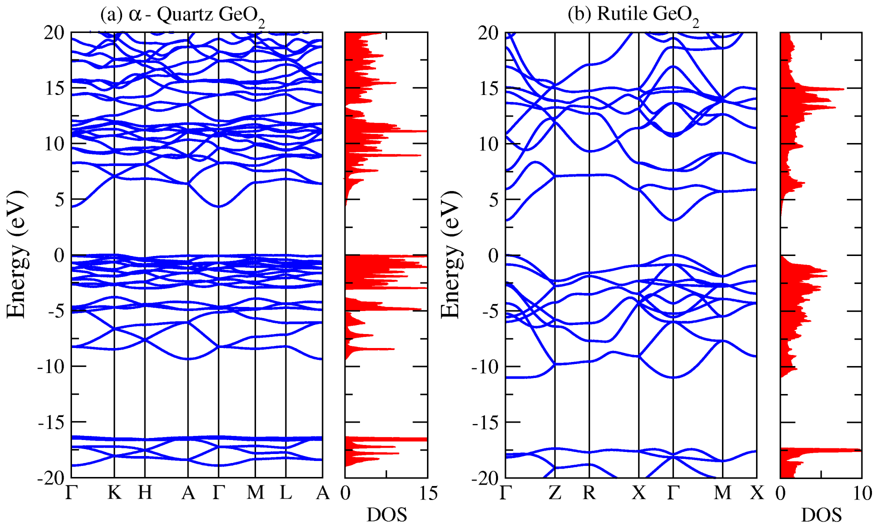

Figure 2.4: LDA band structure and total DOS of (a) α-quartz GeO_2, (c) rutile GeO_2.

Stishovite is a dense polymorph of SiO_2 with octahedrally coordinated silicon, unlike the previous phases [69]. It has a tetragonal cell with two molecules. Calculations were done by using 60 Ha plane wave energy cutoff and $8\times8\times10$ k-point sampling. The band structure of stishovite with a wide single valence band is markedly different from that of the previous three crystalline phases of SiO_2 having two narrow upper valence bands. The cause of this increased valence bandwidth is the lack of separation between bonding and nonbonding states [71]. Hence, the total DOS for stishovite shows no gap at the middle of the valence band (see Fig. 2.2(d)). Our calculations yield a direct LDA band gap of 5.606 eV at Γ. As seen in Table 2.3, the differences between our computed elastic constants and the experimental values are less than 3%; this is an excellent agreement for LDA. Its bulk modulus is the largest among all the host lattice polymorphs considered in this work. Moreover, dielectric constants of stishovite is the largest of the five polymorphs of SiO_2 considered in this work (see Table 2.4).

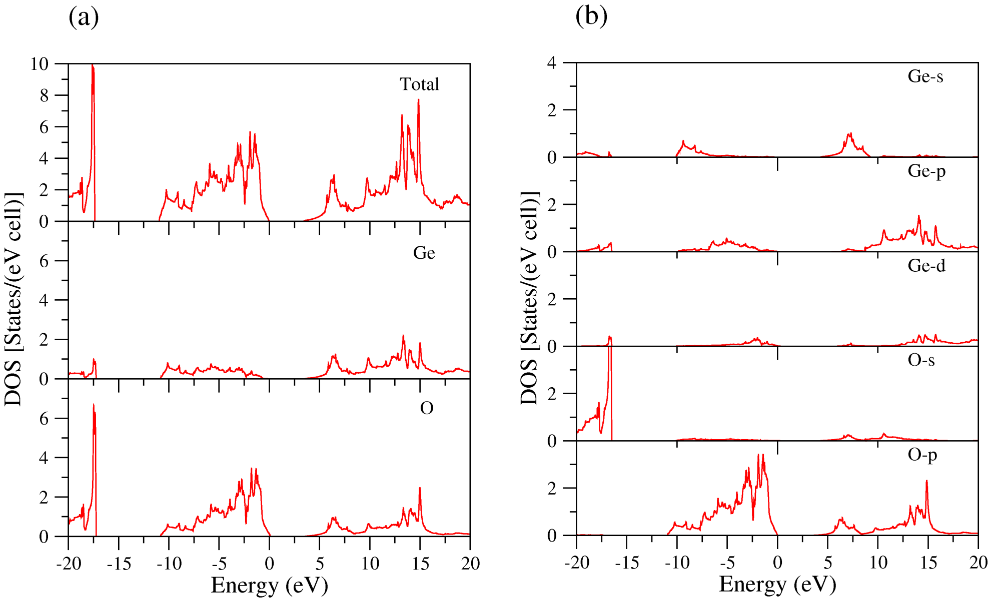

Figure 2.5: DOS of rutile GeO_2 (a) Element-resolved; total PDOS of Ge, PDOS of O. (b) Angular momentum-resolved; Ge *s* electrons, Ge *p* electrons, Ge *d* electrons, O *s* electrons, O *p* electrons.

2.1.3.2 GeO$_2$

For α-quartz GeO_2 we used the same energy cutoff and k-point sampling as with α-quartz SiO_2, which yields excellent convergence. The band structure of the α-quartz GeO_2 is displayed in Fig. 2.4(a). The similarity of the band structures of the α-quartz GeO_2 and the α-quartz SiO_2 is not surprising as they are isostructural. Similarly their total DOS resemble each other (cf. Fig. 2.4(a)). The indirect LDA band gap for this phase is 4.335 eV from the valence band maximum at K to the conduction band minimum at Γ. The direct band gap at Γ is slightly different from indirect band gap as seen in Table 2.5. This gap is smaller than that of the α-quartz SiO_2. The perfect agreement between calculated elastic constants of the α-quartz GeO_2 and experimental values [91, 81] can be observed in Table 2.3.

The rutile structure of GeO_2, also known as argutite [99] is isostructural with the stishovite phase of SiO_2. The same energy cutoff and k-point sampling values as for stishovite yield excellent convergence. The direct LDA band gap at Γ

for rutile-GeO_2 is less than that of stishovite with a value of 3.126 eV. The two upper valence bands are merged in the total DOS (see Fig. 2.4(b)) as in the case of stishovite. The increased valence bandwidth in the band structure can be explained by the same reason as in the case of stishovite. The results of the elastic constants calculated with KA type pseudopotential shown in Table 2.3 deviate substantially from the experiment whereas the agreement with the FHI pseudopotentials is highly satisfactory. The similarity of the dielectric constants of rutile GeO_2 and stishovite can be observed in Table 2.4.

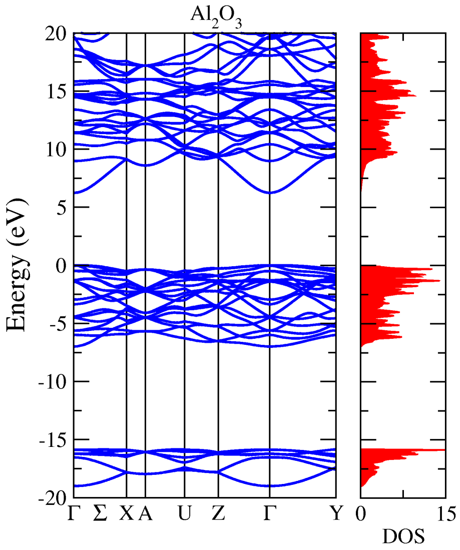

Figure 2.6: LDA band structure of and total DOS of α-Al_2O_3.

2.1.3.3 Al_2O_3

Al_2O_3 is regarded as a technologically important oxide due to its high dielectric constant and being reasonably a good glass former after SiO_2 [39]. The α-Al_2O_3 (sapphire) has the rhombohedral cell with two molecules. Computations about Al_2O_3 were done by using 60 Ha plane wave energy cutoff and a total of 60 k-points within the Brillouin zone. Fig. 2.6 shows the computed band structure and total DOS of the α-Al_2O_3. These are in excellent agreement with the previous calculation [66, 68]. For Al_2O_3, minimum of the conduction band is at Γ and maximum of the valence band is at a point along $\Gamma - X$ close to the Γ point. The corresponding LDA band gap is 6.242 eV. Because of the very small difference between the direct and indirect band gaps, Al_2O_3 is considered as a direct band gap insulator. Measured band gap of this crystal is 8.7 eV. However the precise value of the gap of Al_2O_3 is still elusive because of the existence of an excitonic peak near the absorbtions edge [100]. As seen in Table 2.3, computed values of the elastic constant and bulk modulus of Al_2O_3 are in excellent agreement with the experiments. As a furher remark, the α-Al_2O_3 unit cell can be described as hexagonal or rhombohedral depending on the crystallographical definition of the space group $R\overline{3}C$. During our first-principles calculations it has been defined as rhombohedral in which case C_{14} vanishes. Although the sign of C_{14} is experimentally determined to be negative for the hexagonal-Al_2O_3, previous calculations reported a positive value [101]. To check this disagreement we have calculated the elastic constant of the hexagonal-Al_2O_3 and found it to be around -3.0.

2.1.3.4 Si_3N_4 and Ge_3N_4

The research on silicon nitride has largely been driven by its use in microelectronics technology to utilize it as an effective insulating material and also as diffusion mask for impurities. Recently it started to attract attention both as a host embedding material for nanocrystals [47, 48, 49] and also for optical waveguide applications [40]. The α- and β-Si_3N_4 have hexagonal conventional cells with four and two molecules, respectively. We used 60 Ha plane wave energy cutoff and $6\times6\times8$ k-point sampling. The computed band structures of these two phases shown in Figs. 2.7 (a) and (b) are identical to those reported by Xu and Ching [67]. The top of the valence band for β-Si_3N_4 is along the Γ-A direction, and for α-Si_3N_4 it is at the M point. The bottom of the conduction band for two phases are at the Γ point. The direct and indirect LDA band gaps of these two phases are respectively, 4.559 eV, 4.621 eV for α-Si_3N_4 and 4.146 eV, 4.365 eV for the β-Si_3N_4. The general band structure of two phases are very similar, except that the α-Si_3N_4 has twice as many bands because the unit cell is twice as large. The total DOS of these two phases shown in Figs. 2.7(a) and (b) are only marginally different. Calculated values of the elastic constants and bulk modulus of β-Si_3N_4

listed in Table 2.3 are in excellent agreement with the quoted experiments. Those for the α-Si_3N_4 which is thermodynamically less stable with respect to β-phase [102] were left out due to excessive memory requirements for the desired accuracy.

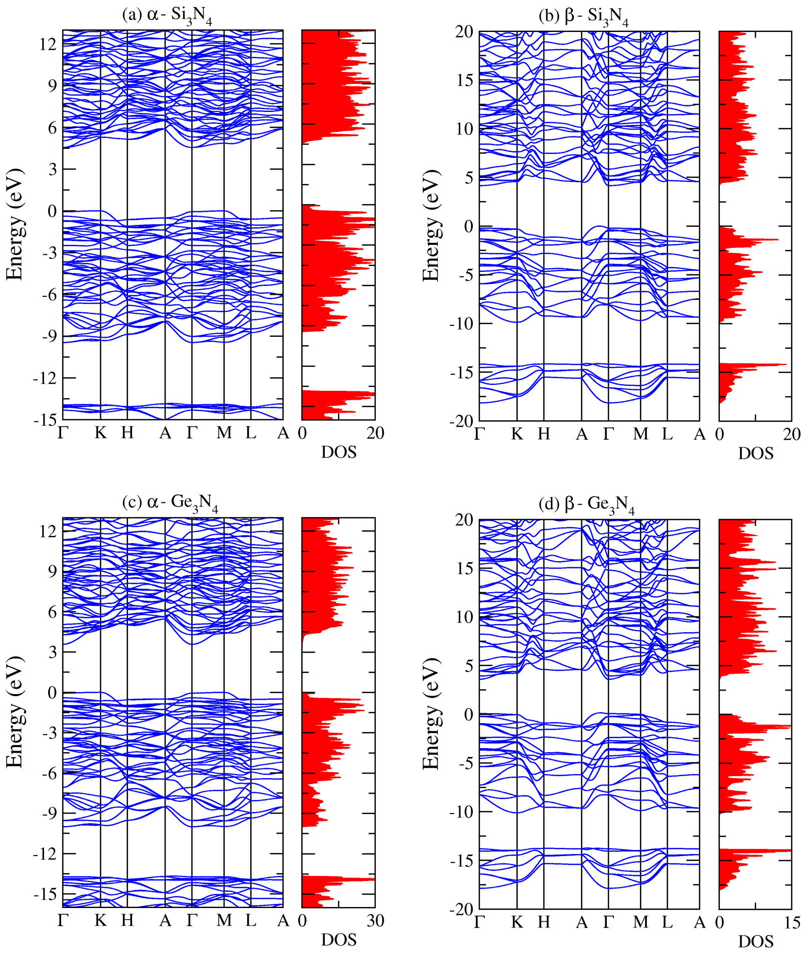

Figure 2.7: LDA band structure and total DOS of (a) α-Si_3N_4, (b) β-Si_3N_4, (c) α-Ge_3N_4 and (d) β-Ge_3N_4.

Ge_3N_4 is the least studied material among the oxides and nitrides considered in this work. Recently its high-pressure γ-phase has attracted some theoretical interest [103]. However, the available Ge_3N_4 samples contain a mixture of α and β-phases as in the case of Si_3N_4 and these are the polymorphs that we discuss in this work. The band structures of both of these phases of Ge_3N_4 (cf. Fig. 2.7) are very similar to those of Si_3N_4. Regarding the elastic constants of β-Ge_3N_4, our theoretical results listed in Table 2.3 await experimental verification. In terms

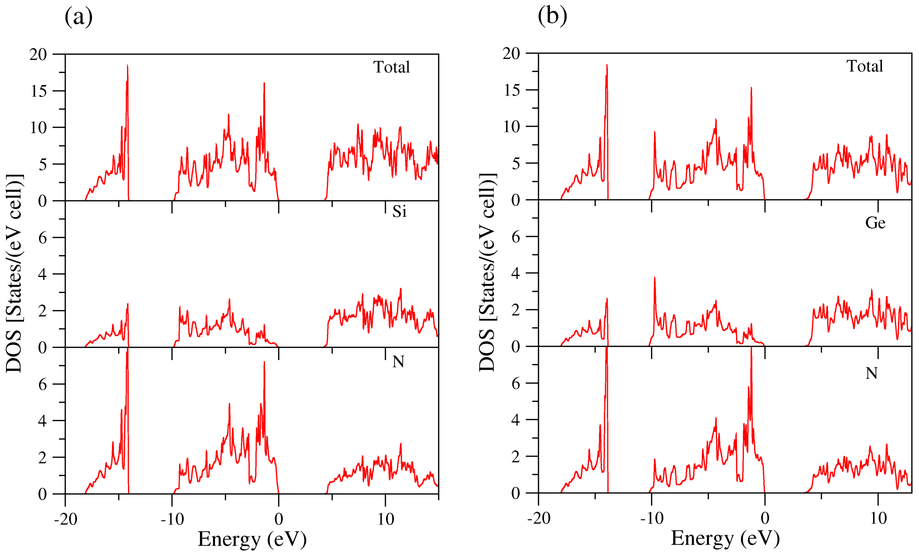

Figure 2.8: Element-resolved DOS of (a) β-Si_3N_4; total, PDOS of Si, PDOS of N, (b) β-Ge_3N_4; total, PDOS of Ge, PDOS of N.

of density, the β phases of Si_3N_4 and Ge_3N_4 fill the gap between the α-quartz and stishovite/rutile phases of their oxides. As can be observed from Fig. 2.9

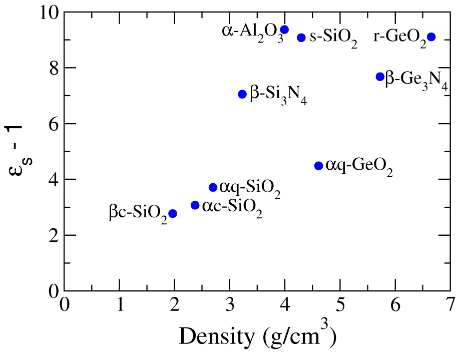

Figure 2.9: Density versus direction-averaged static electric susceptibility.

their electric susceptibility versus density behavior strengthens the correlation established by the remaining polymorphs. Finally it can be noted that β-Ge_3N_4 has the largest high-frequency dielectric constant (ϵ_∞) among all the materials considered in this work.

2.2 High-dielectric constant and wide band gap inverse silver oxide phases of the ordered ternary alloys of SiO_2, GeO_2 and SnO_2

High-dielectric constant and wide band gap oxides have important technological applications. The crystalline oxide polymorphs having lattice constant compatibility to silicon are particularly desirable. One recently reported candidate is the inverse silver oxide phase of SiO_2. First-principles study of this system together with its isovalent equivalents GeO_2, SnO_2 as well as their ternary alloys are performed. Within the framework of density functional theory both generalized gradient approximation (GGA) and local density approximation (LDA) are employed to obtain their structural properties, elastic constants and the electronic band structures. To check the stability of these materials, phonon dispersion curves are computed which indicate that GeO_2 and SnO_2 have negative phonon branches whereas their ternary alloys $Si_{0.5}Ge_{0.5}O_2$, $Si_{0.5}Sn_{0.5}O_2$, and $Ge_{0.5}Sn_{0.5}O_2$ are all stable within LDA possessing dielectric constants ranging between 10 to 20. Furthermore, the lattice constant of $Si_{0.5}Ge_{0.5}O_2$ is virtually identical to the Si(100) surface. The *GW* band gaps of the stable materials are computed which restore the wide band gap values in addition to their high dielectric constants.

2.2.1 Introduction

High-dielectric constant and wide band gap oxides are of general interest for the next-generation gate oxides for silicon-based electronics [39] and also as host matrices for nonvolatile flash memory applications [104]. Amorphous oxides have been generally preferred as they are good glass-formers which tend to minimize the number of dangling bonds at the interface. In this respect, poly-crystalline oxides are undesirable as the grain boundaries cause higher leakage currents and possible diffusion paths for dopants [39]. On the other hand, *crystalline* oxide grown epitaxially on silicon [105] can be favorable as it will result in high interface quality provided that it is lattice-matched to Si.

Very recently, Ouyang and Ching [106] have reported a high-density cubic polymorph of SiO_2 in the inverse Ag_2O structure, named by them as the i-phase, possessing both high dielectric constant, as in stishovite phase, and the lattice constant compatibility to Si(100) face which make it very attractive for electronic applications. In this part of the thesis, we report our contribution to this search for the crystalline high-dielectric constant oxides with the i-phases of GeO_2 and SnO_2 as well as their ordered ternary alloys with SiO_2. This pursuit is in line with the International Technology Roadmap for Semiconductors where computational synthesis of novel high-dielectric materials is emphasized [107]. We employ the well-established *ab initio* framework based on the density functional theory within the GGA and LDA using pseudopotentials and a plane wave basis [108].

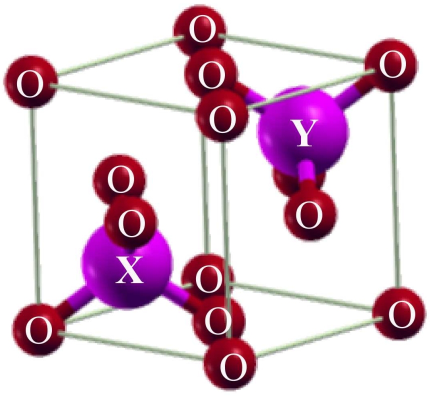

Figure 2.10: Ball and stick model of the i-phase ordered ternary alloy $X_{0.5}Y_{0.5}O_2$.

2.2.2 Computational Details

The unit cell for the ordered ternary alloy $X_{0.5}Y_{0.5}O_2$ in the inverse Ag_2O structure is shown in Fig. 2.10. Structural and electronic properties of the i-phase structures under consideration have been calculated within the density functional theory [108], using the plane wave basis pseudopotential method as implemented in the ABINIT code [19]. The results are obtained under the the GGA and

LDA where for the exchange-correlation interactions we use the Teter-Pade parameterization [73], which reproduces Perdew-Zunger [74] (which reproduces the quantum Monte Carlo electron gas data of Ceperley and Alder [75]).

We tested the LDA results under two different norm-conserving Troullier and Martins [76] type pseudopotentials, which were generated by A. Khein and D.C. Allan (KA) and Fritz Haber Institute (FHI); for either set, the *d* electrons were not included in the valence configuration. Our calculated values for these two types of pseudopotentials were very similar. In the course of both GGA and LDA computations, the plane wave energy cutoff and k-point sampling were chosen to assure a 0.001 eV energy convergence for all i-phase crystals. In the case of SiO_2 this demands a 65 Ha plane wave energy cutoff and 10×10×10 *k*-point sampling. Phonon dispersions and phonon density of states were computed by the PHON program [109] using a $2 \times 2 \times 2$ supercell of 48 atoms to construct the dynamical matrix[1]. The required forces were extracted from ABINIT. The corrected band gap values are computed by obtaining self-energy corrections to the DFT Kohn-Sham eigenvalues in the *GW* approximation [110]. All parameters used during the *GW* calculation were chosen to assure a 0.001 eV energy convergence.

2.2.3 Results

Table 2.6: First-principles LDA and GGA structural data for i-phase crystals.

Crystal		a (Å)	Density (gr/cm^3)	x-O (Å)	y-O (Å)
SiO_2	LDA	3.734	3.830	1.617	
	GGA	3.801	3.633	1.646	
GeO_2	LDA	3.916	5.781	1.696	
	GGA	4.053	5.215	1.755	
SnO_2	LDA	4.180	6.864	1.808	
	GGA	4.452	5.671	1.928	
$Ge_{0.5}Si_{0.5}O_2$	LDA	3.836	4.843	1.697	1.625
	GGA	3.923	4.528	1.762	1.635
$Ge_{0.5}Sn_{0.5}O_2$	LDA	4.042	6.416	1.688	1.813
	GGA	4.250	5.522	1.748	1.932
$Sn_{0.5}Si_{0.5}O_2$	LDA	3.970	5.590	1.818	1.620
	GGA	4.114	5.015	1.935	1.628

---

[1] We are grateful to Prof. O. Gülseren for his valuable technical guidance in this part.

2.2.3.1 General

Using XO_2 and $X_{0.5}Y_{0.5}O_2$ as the generic notation, the O-X-O and O-Y-O bond angles are 109.47° and the X-O-X and X-O-Y bond angles are 180° according to the crystal construction of this cubic i-phase (cf. Fig. 2.10). Other structural information such as the lattice constants and bond lengths of all i-phase crystals are listed in Table 2.6. The Si(100) surface lattice constant is about 3.83 Å, therefore according to LDA results $Si_{0.5}Ge_{0.5}O_2$ is of particular interest as it can be epitaxially grown on Si without any strain. According to our well-converged calculations $Si_{0.5}Ge_{0.5}O_2$ has a lower total energy compared to both SiO_2 and GeO_2, the latter itself is unstable as will be shown later; this can be taken as some indication of immunity to the phase separation of this ternary alloy into its binary compounds.

Table 2.7: Elastic constants and bulk modulus for each crystal.

Crystal		C_{11}(GPa)	C_{12}(GPa)	C_{44}(GPa)	B(GPa)
SiO_2	LDA	383.6	260.0	243.0	301
	GGA	354.3	232.1	227.9	273
GeO_2	LDA	297.0	231.2	175.6	253
SnO_2	LDA	208.9	185.5	113.9	193
$Ge_{0.5}Si_{0.5}O_2$	LDA	349.4	253.2	200.0	285
	GGA	292.8	203.9	161.8	234
$Ge_{0.5}Sn_{0.5}O_2$	LDA	255.4	210.8	106.3	226
$Sn_{0.5}Si_{0.5}O_2$	LDA	277.5	217.4	103.9	237
	GGA	238.3	183.0	202.8	201

2.2.3.2 Stability

The LDA and GGA results of the three independent elastic constants and bulk modulus for all crystals are tabulated in Table 2.7. An important concern is the stability of these cubic phases. The requirement of mechanical stability on the elastic constants in a cubic crystal leads to the following constraints: $C_{11} > C_{12}$, $C_{11} > 0$, $C_{44} > 0$, and $C_{11} + 2C_{12} > 0$. The elastic constants calculated by both LDA and GGA shown in Table 2.7 satisfy these stability conditions. Furthermore, we compute the LDA and GGA phonon dispersion curves of these structures using the PHON program [109]. First, to verify the validity of the results of the PHON program we compute the phonon dispersions of the SiO_2 and GeO_2 by using both

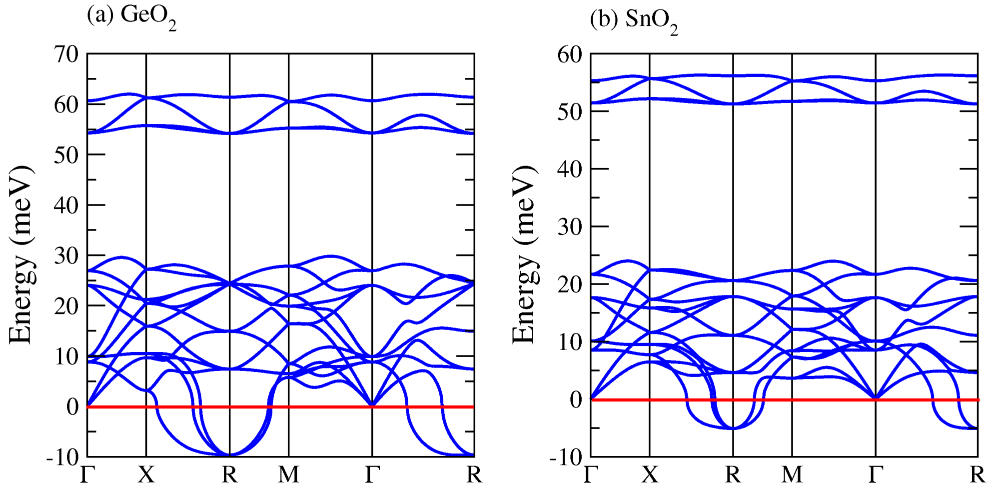

Figure 2.11: LDA phonon dispersions of the unstable crystals: (a) GeO_2, (b) SiO_2.

PHON and ANADDB extension of the ABINIT code [19]. There exists a good agreement between two calculations. Next, we calculate the phonon dispersions of the all i-phase crystals via PHON program with forces obtained from LDA and GGA. It is observed that SiO_2 is at least locally stable whereas GeO_2 and SnO_2 contains negative phonon branches which signal an instability of these phases (see Fig. 2.11). As for their alloy, $Ge_{0.5}Sn_{0.5}O_2$, according to LDA this material is stable whereas within GGA it comes out as unstable. For the stable structures the LDA phonon dispersions and the associated phonon DOS are shown in Fig. 2.12.

Table 2.8: LDA and GGA dielectric permittivity tensor for the stable crystals.

Crystal		$\epsilon^0_{xx} = \epsilon^0_{yy} = \epsilon^0_{zz}$	$\epsilon^\infty_{xx} = \epsilon^\infty_{yy} = \epsilon^\infty_{zz}$
SiO_2	LDA	9.857	3.285
	GGA	9.970	3.303
$Ge_{0.5}Si_{0.5}O_2$	LDA	11.730	3.416
	GGA	14.383	3.585
$Ge_{0.5}Sn_{0.5}O_2$	LDA	19.415	3.527
$Sn_{0.5}Si_{0.5}O_2$	LDA	12.883	3.360
	GGA	18.096	3.711

For the stable systems, the static and high-frequency dielectric constants are listed in Table 2.8. The static dielectric constants falling in the range between 10 to 20 suggest that these are moderately high dielectric constant crystals. It can be observed that GGA yields systematically higher values for the dielectric constants of these structures. Employing KA pseudopotentials, the LDA band

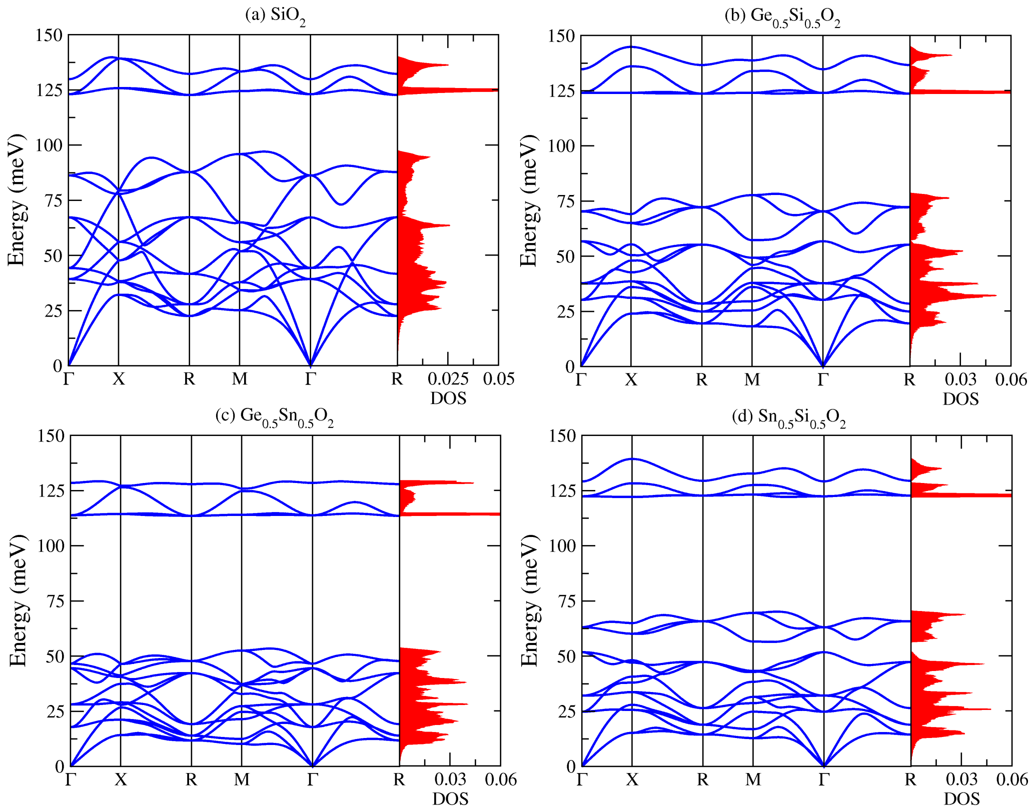

Figure 2.12: LDA phonon dispersions and the phonon DOS (a. u.) of the stable crystals: (a) SiO$_2$, (b) Ge$_{0.5}$Si$_{0.5}$O$_2$, (c) Ge$_{0.5}$Sn$_{0.5}$O$_2$, and (d) Si$_{0.5}$Sn$_{0.5}$O$_2$.

structure for the crystals are displayed along the high-symmetry lines in Fig. 2.13 including the electronic DOS. The widths of the valence bands get progressively narrowed from Fig. 2.13(a) to (d), i.e., from SiO$_2$ to Sn$_{0.5}$Si$_{0.5}$O$_2$. For all of the i-phase crystals under consideration including the unstable ones the conduction band minima occur at the Γ point whereas the valence band maxima are located at R point making them indirect band gap semiconductors. As tabulated in Table 2.9, the direct band gap values are only marginally above the indirect band gap values. Again GGA systematically yields narrower band gaps compared to LDA.

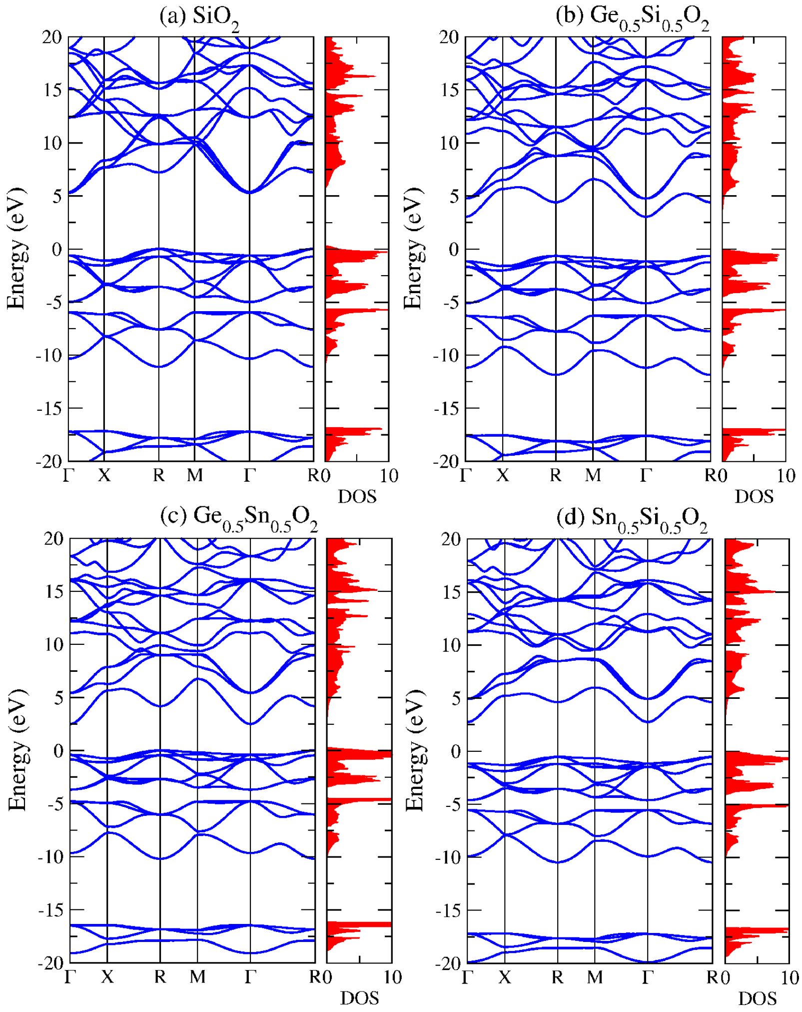

Figure 2.13: LDA electronic band structure and DOS (States/eV cell) of i-phase (a) SiO_2, (b) $Ge_{0.5}Si_{0.5}O_2$, (c) $Ge_{0.5}Sn_{0.5}O_2$, and (d) $Sn_{0.5}Si_{0.5}O_2$.

2.2.3.3 GW Band Gap Correction

A renown artifact of LDA is that for semiconductors and insulators band gaps are underestimated [108]. In this part of our work, the corrected band gap values are also provided by *GW* approximation. As there are different *GW* implementations we briefly highlight the particular methodology followed in the ABINIT code. First, a converged ground state calculation (at fixed lattice parameters and atomic positions) is done to get self-consistent density and potential, and Kohn-Sham

Table 2.9: Indirect (E_g) and direct ($E_{g,\Gamma}$) band gaps for each i-phase crystal within LDA, GGA, and for the stable structures the *GW* approximation (GWA).

Crystal		E_g (eV)	$E_{g,\Gamma}$ (eV)
SiO_2	LDA	5.269	5.870
	GGA	4.584	5.155
	GWA	7.283	7.964
GeO_2	LDA	2.402	2.511
SnO_2	LDA	2.285	2.670
$Ge_{0.5}Si_{0.5}O_2$	LDA	3.666	4.179
	GGA	2.558	3.005
	GWA	5.943	6.513
$Ge_{0.5}Sn_{0.5}O_2$	LDA	2.487	2.900
	GGA	0.767	0.865
	GWA	4.533	4.972
$Sn_{0.5}Si_{0.5}O_2$	LDA	3.292	3.900
	GGA	1.763	2.304
	GWA	5.484	6.153

eigenvalues and eigenfunctions at the relevant band extrema k-points as well as on a regular grid of k-points. Next, on the basis of these available Kohn-Sham data, the independent-particle susceptibility matrix χ_0 is computed on a regular grid of q-points, for at least two frequencies (usually, zero frequency and a large pure imaginary frequency - on the order of the plasmon frequency, a dozen of eV). Finally, the Random Phase Approximation susceptibility matrix, χ, the dielectric matrix ϵ and its inverse ϵ^{-1} are computed. On this basis, the self-energy, Σ matrix element at the given k-point is computed to derive the *GW* eigenvalues for the target states at this k-point. Note that this *GW* correction is achieved as a one-shot calculation (i.e., no overall self-consistency) hence, our results technically corresponds to G_0W_0 which has been the standard approach as originally proposal by Hedin [111]. The *GW* correction as can be observed from Table 2.9 restores the wide band gap values; this feature is essential for these materials to provide sufficient confinement to carriers of the narrow band gap semiconductors such as silicon.

2.2.3.4 Final Remarks

We have also considered the i-phase of PbO_2 which turned out to be unstable and hence its *ab initio* data are not included. In this work, we do not consider the thermodynamic stability of these i-phase oxides. However, for technological applications rather than bulk systems the epitaxial growth conditions become more critical [112]. A promising direction can be the finite temperature investigation [113] of these i-phase isovalent structures on Si(100) surfaces using large number of monolayers.

Chapter 3

Modeling of the Hot Carrier Transport Through SiO_2 and the Quantum-Confined Impact Ionization Processes

Injected carriers from the contacts to delocalized bulk states of the oxide matrix via Fowler-Nordheim tunneling can give rise to quantum-confined impact ionization (QCII) of the nanocrystal (NC) valence electrons. This process is responsible for the creation of confined excitons in NCs, which is a key luminescence mechanism. For a realistic modeling of QCII in Si NCs, a number of tools are combined: ensemble Monte Carlo (EMC) charge transport, *ab initio* modeling for oxide matrix, pseudopotential NC electronic states together with the closed-form analytical expression for the Coulomb matrix element of the QCII. To characterize the transport properties of the embedding amorphous SiO_2, *ab initio* band structure and density of states of the α-quartz phase of SiO_2 are employed. The confined states of the Si NC are obtained by solving the atomistic pseudopotential Hamiltonian. With these ingredients, realistic modeling of the QCII process involving a SiO_2 bulk state hot carrier and the NC valence electrons is provided.

3.1 Introduction

Due to its indirect band gap, bulk Si is a very inefficient emitter, even at liquid He temperatures. Within the last decade, several approaches were developed towards improving the efficiency of light emission from Si-based structures. In spirit, all were based on the lifting of the lattice periodicity that introduces an uncertainty in the **k**-space and therefore altering the indirect nature of this material. Some examples are: SiGe or Si\SiO$_2$ superlattices [1, 2] or Si nanocrystal (NC) assemblies [3]. Recently, blue electroluminescence (EL) from Si-implanted SiO$_2$ layers and violet EL from Ge-implanted SiO$_2$ layers were observed. An important process responsible for EL occurring in quantum dots and NCs is the quantum-confined impact ionization (QCII). A carrier initially at a high energy in the continuum states of the bulk structure when able to excite a valence band

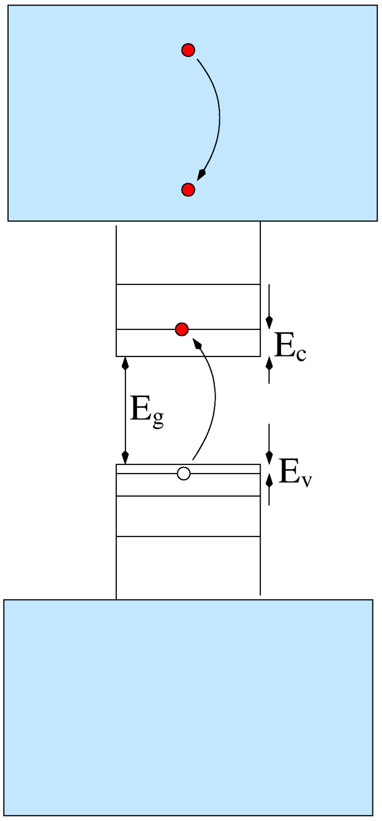

Figure 3.1: Quantum-confined impact ionization in NCs.

electron of a NC across its band gap creates an electron-hole pair (cf. Fig. 3.1). This process is responsible for the introduction of confined excitons in silicon NC LEDs, which is a key luminescence mechanism. In contrast to its crucial role, QCII has not been given the attention it deserves.

To model the QCII process, we start by characterizing the hot electron transport in oxides within the ensemble Monte Carlo (EMC) framework. Our EMC code [114, 115] includes all major scattering mechanism such as acoustic, polar and non-polar optical phonon scatterings. Density of states and band structure of common crystal phases of the SiO_2 used in our Monte Carlo transport calculation were described in Chapter 2 of this thesis. As the main contribution of this part of the thesis, we derive an analytical expression for the QCII probability in NCs that can become an instrumental result in assessing EL in the presence of other competing scattering mechanisms. The effect of QCII on bulk transport quantities is also discussed.

3.1.1 Theoretical Details

Details about first principles calculations can be found in Chapter 2. Here, we demonstrate the utility and the validity of our *ab initio* DOS results by studying the high-field carrier transport in bulk SiO_2 up to fields of 10 MV/cm using the EMC technique. The corresponding scattering rates are intimately related with the band structure and the DOS of SiO_2 for which we use those of the α-quartz phase due to its strong resemblance of the amorphous SiO_2 in terms of both the short-range order and the total DOS [116]. Aiming for very high fields around 10 MV/cm, we also include the impact ionization process within the *bulk* SiO_2 medium; the relevant parameters were taken from the work of Arnold *et al.* [117].

Our modeling for QCII is an extension of the approach by Kehrer *et al.* who have dealt with the high-field impurity breakdown in n-GaAs [118]. We assume the impacting carrier to be an electron, however all of the formulation can be reiterated by starting with an impacting high energy *hole* in SiO_2. Above the mobility edge which is well satisfied for an energetic electron in SiO_2, the bulk

SiO_2 wave function will be delocalized, i.e., of the Bloch form,

$$\psi_b = \frac{1}{\sqrt{V}} u_k(\mathbf{r}) e^{i\mathbf{k}\cdot\mathbf{r}}, \tag{3.1}$$

whereas for the NC wave function we use a simple hydrogenic form [118],

$$\psi_n = \frac{\alpha_v^{3/2}}{\sqrt{\pi}} u_v(\mathbf{r}) e^{-\alpha_v |\mathbf{r}|}. \tag{3.2}$$

Some remarks will be in order, regarding the choice of these wave functions. Even though the embedding medium is usually an *amorphous* oxide, for high-field transport purposes well above the mobility edge, one can safely use crystalline states (i.e., Bloch functions) [116, 117]. On the other hand, the use of hydrogenic wave function which is well suited for the impurity problem was preferred solely due to its analytical convenience. The latter can be relaxed in case a closed-form expression is not aimed for.

Furthermore, we are neglecting the exchange interaction between the impacting electron and the valence nanocrystal electron due to huge energy difference between them[1] [119]. The scattering matrix element which is due to the Coulomb interaction between the two electrons is given by

$$\begin{aligned} M &= \int d^3\mathbf{r_1} \int d^3\mathbf{r_2} \frac{\alpha_c^{3/2}}{\sqrt{\pi}} u_c^*(\mathbf{r_1}) e^{-\alpha_c|\mathbf{r_1}|} \frac{1}{\sqrt{V}} u_{k'}^*(\mathbf{r_2}) e^{-i\mathbf{k}'\cdot\mathbf{r_2}} \\ &\quad \times \frac{e^2}{4\pi\epsilon\epsilon_0} \frac{e^{-\lambda|\mathbf{r_1}-\mathbf{r_2}|}}{|\mathbf{r_1}-\mathbf{r_2}|} \frac{1}{\sqrt{V}} u_k(\mathbf{r_2}) e^{i\mathbf{k}\cdot\mathbf{r_2}} \frac{\alpha_v^{3/2}}{\sqrt{\pi}} u_v(\mathbf{r_1}) e^{-\alpha_v|\mathbf{r_1}|}, \end{aligned} \tag{3.3}$$

yielding

$$\begin{aligned} |M|^2 &= \left[\frac{64 e^4 \alpha_c^3 \alpha_v^3 \alpha^2}{(\epsilon\epsilon_0 V)^2}\right] |F_{cv}|^2 |F_{k'k}|^2 \frac{1}{[|\mathbf{k}-\mathbf{k}'|^2+\lambda^2]^2} \\ &\quad \times \frac{1}{[|\mathbf{k}-\mathbf{k}'|^2+\alpha^2]^4}, \end{aligned} \tag{3.4}$$

where,

$$F_{cv} = \int_{cell} u_c^*(\mathbf{r_1}) u_v(\mathbf{r_1}) d^3\mathbf{r_1}\,, \tag{3.5}$$

$$F_{k'k} = \int_{cell} u_{k'}^*(\mathbf{r_2}) u_k(\mathbf{r_2}) d^3\mathbf{r_2}\,, \tag{3.6}$$

---

[1] We are grateful to Prof. M. Özgür Oktel for pointing out this simplicity.

and $\alpha \equiv \alpha_c + \alpha_v$. By using Fermi's golden rule we can write the probability as,

$$P(k) = \sum_{nc}\sum_{k'} \frac{2\pi}{\hbar}|M|^2 \delta\left[\frac{\hbar^2 k^2}{2m_k} - E_v - E_c - E_g - \frac{\hbar^2 k'^2}{2m_{k'}}\right] f_{NC}\,, \tag{3.7}$$

where E_g is that bandgap of the NC which is absorbed into the value of E_c. Here E_v is taken as positive hole energy. Taking $A^2 \equiv \frac{m_{k'}k^2}{m_k} - \frac{2m_{k'}E_v}{\hbar^2} - \frac{2m_{k'}E_c}{\hbar^2} - \frac{2m_{k'}E_g}{\hbar^2}$ and assuming

$$\sum_{nc} f_{NC} = N_{NC} = n_{NC}V\,, \tag{3.8}$$

where n_{NC} is the density per unit volume and in terms of the NC filling ratio n_{NC} is

$$n_{NC} = \frac{f}{V_{NC}}, \tag{3.9}$$

$$P(k) = \sum_{k'} \frac{4\pi m_{k'}}{\hbar^3}|M|^2 \delta\left[A^2 - k'^2\right] n_{NC}V\,. \tag{3.10}$$

Note that there is no spin summation as the Coulomb interaction preserves spin. Using Eq. B.9 and Eq. 3.8 we can write

$$\begin{aligned} P(k) &= \frac{V}{(2\pi)^3}\int d^3\mathbf{k}' \frac{4\pi m_{k'}}{\hbar^3}\left[\frac{64e^4\alpha_c^3\alpha_v^3\alpha^2}{(\epsilon\epsilon_0 V)^2}\right]|F_{cv}|^2|F_{k'k}|^2\frac{1}{[|\mathbf{k}-\mathbf{k}'|^2+\lambda^2]^2} \\ &\quad\times\frac{1}{[|\mathbf{k}-\mathbf{k}'|^2+\alpha^2]^4}\delta\left[A^2 - k'^2\right] n_{NC}V\,. \end{aligned} \tag{3.11}$$

$$\begin{aligned} P(k) &= -\frac{\pi C}{2k}\frac{1}{3(\alpha^2-\lambda^2)^5}\left[-\frac{9(\alpha^2-\lambda^2)}{(|A|-k)^2+\alpha^2} + \frac{9(\alpha^2-\lambda^2)}{(|A|+k)^2+\alpha^2}\right. \\ &- \frac{3(\alpha^2-\lambda^2)^2}{((|A|-k)^2+\alpha^2)^2} + \frac{3(\alpha^2-\lambda^2)^2}{((|A|+k)^2+\alpha^2)^2} - \frac{(\alpha^2-\lambda^2)^3}{((|A|-k)^2+\alpha^2)^3} \\ &+ \frac{(\alpha^2-\lambda^2)^3}{((|A|+k)^2+\alpha^2)^3} - \frac{3(\alpha^2-\lambda^2)}{((|A|-k)^2+\lambda^2)} + \frac{3(\alpha^2-\lambda^2)}{((|A|+k)^2+\lambda^2)} \\ &+ \left.12\ln\left\{\frac{[(|A|-k)^2+\alpha^2]\,[(|A|+k)^2+\lambda^2]}{[(|A|+k)^2+\alpha^2]\,[(|A|-k)^2+\lambda^2]}\right\}\right]. \end{aligned} \tag{3.12}$$

where,

$$C = \left[\frac{32e^4\alpha_c^3\alpha_v^3\alpha^2 m_{k'}}{\hbar^3\pi^2(\epsilon\epsilon_0)^2}\right]|F_{cv}|^2|F_{k'k}|^2 n_{NC}\,, \tag{3.13}$$

here the screening parameter within Thomas-Fermi approximation is given in cgs units by

$$\lambda = \left[4(3/\pi)^{1/3} \frac{n_0^{1/3}}{a_0} \right]^{1/2} . \tag{3.14}$$

We should note that the direct adoption of the bulk screening model to the case of NCs discards the polarization charges on the NC surface which are supposed to cancel the screening effect within the oxide region [120].

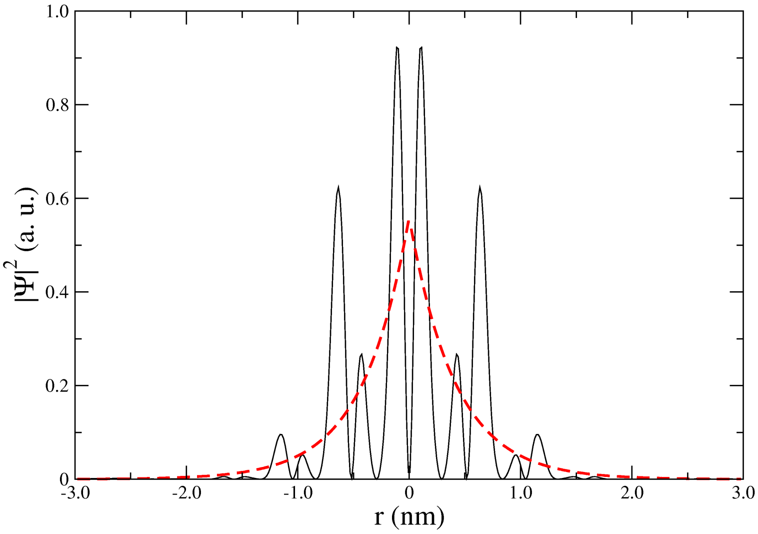

Figure 3.2: Pseudopotential and the fitted hydrogenic wave functions.

The α parameter of the wave function shown in Eq. 3.2 is extracted by fitting it to the wave function obtained from a pseudopotential-based electronic structure calculation for Si NCs [27] both of which are illustrated in Fig. 3.2. The details for the pseudopotential-based electronic structure calculation will be provided in the next Chapter. The effect of the carrier density due to Thomas-Fermi screening length can be observed in Fig. 3.3. As seen in Eq. A.42, NC density and QCII scattering probability are directly proportional as expected.

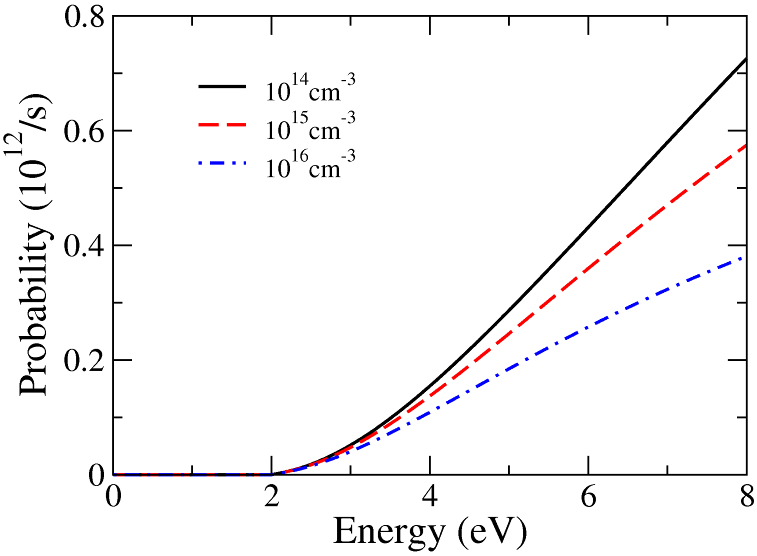

Figure 3.3: QCII probability for carrier densities; 10^{14} cm^{-3}, 10^{15} cm^{-3}, and 10^{16} cm^{-3}.

3.1.2 High Field Transport Results

We simulate the high field transport for both electrons and holes within SiO_2 and observe a marked difference between the two as seen from the average carrier velocity curve in Fig. 3.4 (a). The holes acquire a much slower velocity than the electrons governed by a monotonic behavior. On the other hand, electrons experience a negative differential mobility regime between 1.5 MV/cm to 5 MV/cm. Fig. 3.4 (b) displays the average energy as a function of field. Our results agree quite well with the experimental data [60] for fields up to 7 MV/cm. Beyond this value, the two experiments deviate substantially from each other while the ensemble Monte Carlo results fall between the two. Another important observation is that the energy gained by the holes is well below 0.5 eV even for fields above 10 MV/cm due to excessive scattering which is a consequence of the very large DOS close to the valence band edge. For Si NCs embedded in SiO_2 the EL peak is typically around 2 eV [121]. Based on our results we can conclude that such an energy cannot be imparted by the bulk SiO_2 holes to the NC carriers through the quantum confined impact ionization process. Other mechanisms such as direct tunneling from contacts to NCs may be responsible for the *p*-type EL.

(a) Field vs Velocity for SiO_2

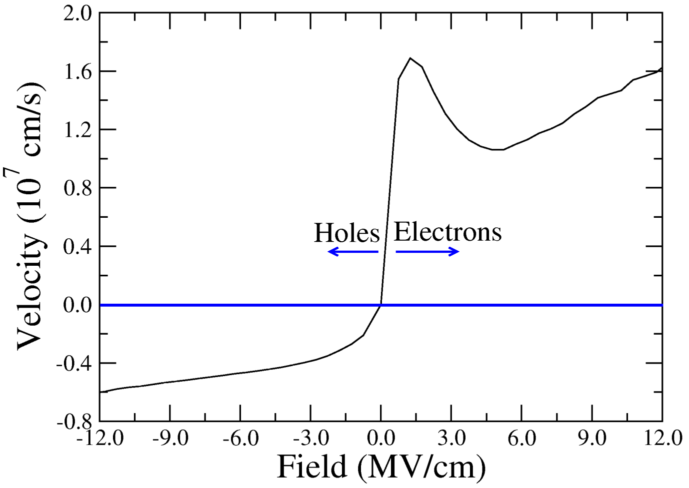

(b) Field vs Energy for SiO_2

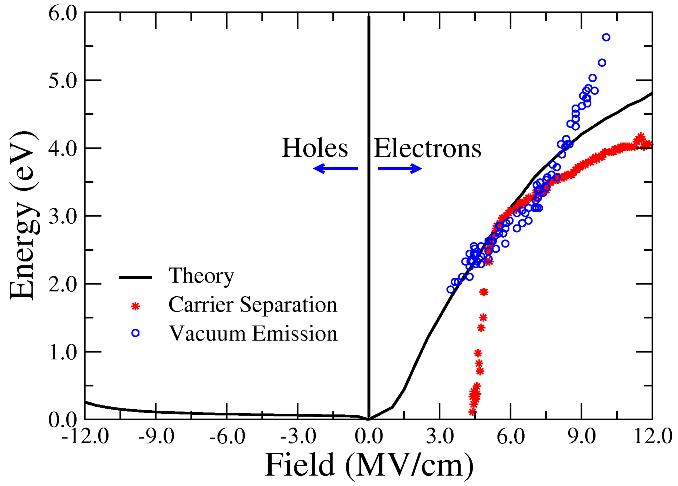

Figure 3.4: For SiO_2 (a) average velocity vs field (b) field vs energy profiles for both electrons and holes.

Turning to electrons which can become indeed hot in SiO_2 matrix, in Fig. 3.5 (a) and (b) we illustrate the temporal evolution of the energy and velocity, respectively at different electric field values. It can be observed that steady state is attained for these hot electrons within about 30 fs. Furthermore, there is a strong velocity overshoot which is the hallmark of hot electrons [115] where nonequilibrium carriers initially enjoy an almost ballistic motion that is eventually brought to equilibrium. We also simulate the high field transport with and without QCII

(a) Time vs Energy for SiO_2

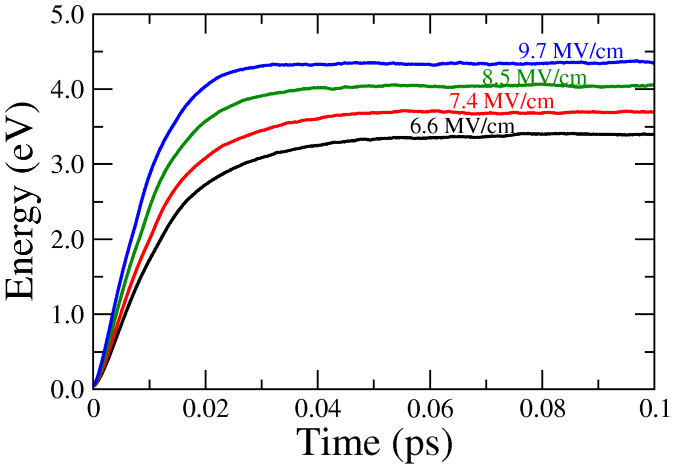

(b) Time vs Velocity for SiO_2

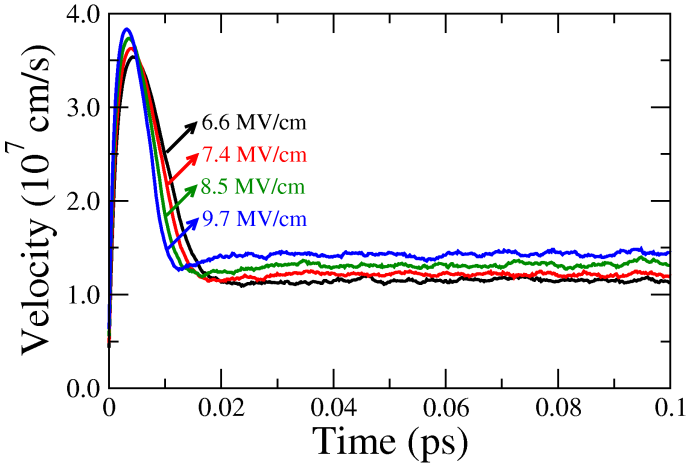

Figure 3.5: Temporal evolution of the ensemble-averaged (a) electron energy and (b) average velocity for different electric field values.

by setting the carrier and NC densities to 10^{15} cm^{-3} and 10^{21} cm^{-3}. It can be inferred from the average energy versus field behavior (see Fig. 3.6 (a)) that QCII does not have significant effect. In Figs. 3.6 (b) and (c) we illustrate the temporal evolution of the average carrier energy and velocity with and without QCII at a fixed electric field value of 8 MV/cm; carrier and NC densities are again chosen as 10^{15} cm^{-3} and 10^{21} cm^{-3}, respectively. It can be observed that steady state is attained for these hot electrons within about 30 fs. Furthermore, there is a no pronounced effect of QCII on the average velocity and energy profiles. This is quite understandable given the dominance of the other scattering mechanisims over QCII.

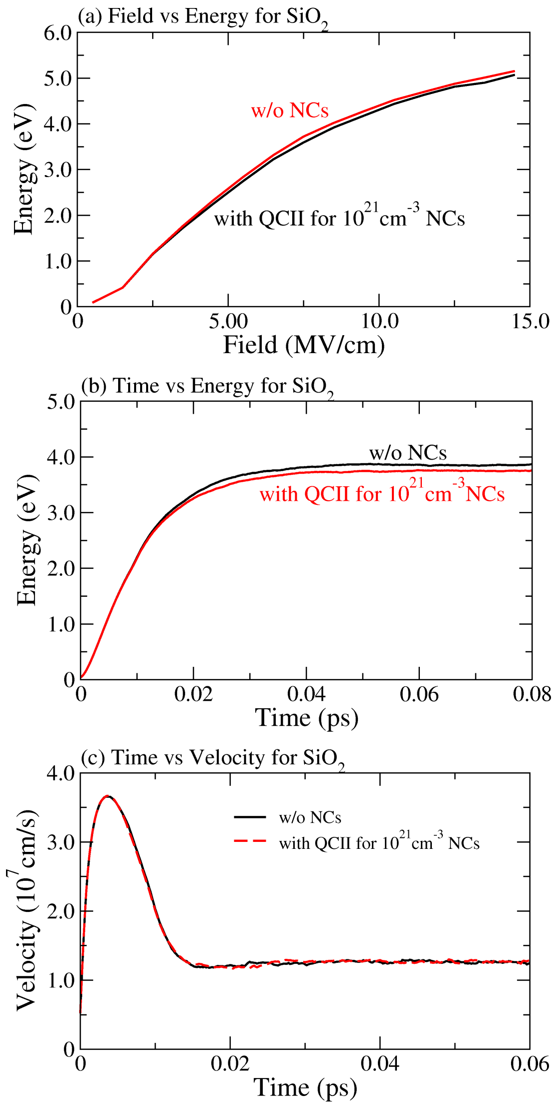

Figure 3.6: For SiO_2 (a) field vs energy, (b) energy vs time and (c) average velocity vs time profiles with and without QCII.

Chapter 4

Pseudopotential-based Atomistic Electronic Structure and Radiative Recombination

Using an atomistic pseudopotential approach the electronic structures for embedded Si and Ge NCs in wide band-gap matrices containing several thousand atoms are employed. From small clusters to large NCs containing on the order of several thousand atoms are considered. Effective band-gap values as a function of NC diameter agree very well the available experimental and theoretical data. To further check the validity of the electronic structure on radiative processes, direct photon emission rates are obtained. Our results for Si and Ge NCs as a function of diameter are in excellent agreement with the available *ab initio* calculations for small NCs. Moreover, our formalism is applicable to much larger NCs as well.

4.1 Introduction

The quantum processes of the semiconductor NCs are related to the optical transition oscillator strength, density of states and real space wavefunctions. To characterize these processes, it is very important to calculate accurate electronic structure of NCs. Here, we follow the approach in Ref. [122] and references therein. As in any such task, the usual trade off between the computational cost and accuracy is operational. The constraints on the former are quite stringent as a NC including the active region of the matrix surrounding itself can contain on the order of ten thousand atoms. As for the latter, not only the accuracy but also the validity of a chosen approach can become questionable. Computationally low-cost approaches like the envelope function in conjunction with 8-band $\mathbf{k}\cdot\mathbf{p}$ are not as accurate for this task and furthermore, they miss some critical symmetries of the underlying lattice [108]. On the other extreme, there lies the density functional theory-based ab initio codes which have been applied to smaller NCs containing less than 1000 atoms which still require very demanding computational resources [123, 57, 58, 124, 125, 126]. The *ab initio* analysis of larger NCs of sizes between 3-10 nm is practically not possible with the current computer power. While this technological hurdle will be gradually overcome in the years to come, there exists other atomistic approaches that can be employed for NC research which can be run on modest platforms and are much simpler to develop, such as the tight binding technique which has been successfully employed by several groups [127, 128, 129]. On the pseudopotential-based approaches, two new recipes were proposed by Wang and Zunger over the last decade [130, 23, 22]. The folded spectrum method [130] relies on standard plane wave basis and direct diagonalization; its speed is granted from being focused on relatively few targeted states. For the study of excitons this approach becomes very suitable whereas for the optical absorption spectra where a large number of states contribute it loses its advantage. Their other recipe is the so-called linear combination of bulk bands (LCBB); it has been used for self-assembled quantum dots [23, 22], superlattices [24, 25] and high-electron mobility transistors [26], and very recently on the nc-Si aggregation stages [27]. In this work, we apply LCBB to the electronic structure and absorption spectra of Si and Ge NCs. An important feature of this work, in contrast to commonly studied hydrogen-passivated NCs is that we consider NCs embedded in a wide band-gap matrix which is usually silica [131]. In principle, other matrices such as alumina or silicon nitride can be investigated along the same lines.

4.2 Theory: Energy Spectrum

For the electronic structure of large-scale atomistic systems Wang and Zunger have developed the LCBB method which is particularly convenient for embedded NCs containing several thousand atoms [23, 22]. The fact that it is a pseudopotential-based method makes it more preferable over the empirical tight binding technique for the study of optical properties as aimed in this work. In this technique the NC wavefunction with a state label j is expanded in terms of the bulk Bloch bands of the constituent core and/or embedding medium (matrix) materials

$$\psi_j(\vec{r}) = \frac{1}{\sqrt{N}} \sum_{n,\vec{k},\sigma} C^{\sigma}_{n,\vec{k},j}\, e^{i\vec{k}\cdot\vec{r}} u^{\sigma}_{n,\vec{k}}(\vec{r})\,, \tag{4.1}$$

where N is the number of primitive cells within the computational supercell, $C^{\sigma}_{n,\vec{k},j}$ is the expansion coefficient set to be determined and σ is the constituent bulk material label pointing to the NC core or embedding medium. $u^{\sigma}_{n,\vec{k}}(\vec{r})$ is the cell-periodic part of the Bloch states which can be expanded in terms of the reciprocal lattice vectors $\{\vec{G}\}$ as

$$u^{\sigma}_{n,\vec{k}}(\vec{r}) = \frac{1}{\Omega_0} \sum_{\vec{G}} B^{\sigma}_{n\vec{k}}\left(\vec{G}\right) e^{i\vec{G}\cdot\vec{r}}\,, \tag{4.2}$$

where Ω_0 is the volume of the primitive cell. The atomistic Hamiltonian for the system is given by

$$\hat{H} = -\frac{\hbar^2\nabla^2}{2m} + \sum_{\sigma,\vec{R}_j,\alpha} W^{\sigma}_{\alpha}(\vec{R}_j)\, \upsilon^{\sigma}_{\alpha}\left(\vec{r} - \vec{R}_j - \vec{d}^{\sigma}_{\alpha}\right)\,, \tag{4.3}$$

where $W^{\sigma}_{\alpha}(\vec{R}_j)$ is the weight function that takes values 0 or 1 depending on the type of atom at the position $\vec{R}_j - \vec{d}^{\sigma}_{\alpha}$, and $\upsilon^{\sigma}_{\alpha}$ is the screened spherical pseudopotential of atom α of the material σ. We use semiempirical pseudopotentials for Si and Ge developed particularly for strained Si/Ge superlattices which reproduces a large variety of measured physical data such as bulk band structures, deformation potentials, electron-phonon matrix elements, and heterostructure valence band offsets [132]. With such a choice, this approach benefits from the empirical pseudopotential method (EPM), which in addition to its simplicity has another advantage over the more accurate density functional *ab initio* techniques that run into well-known band-gap problem [108] which is a disadvantage for the correct prediction of the excitation energies.

The formulation can be casted into the following generalized eigenvalue equation [22, 26]:

$$\sum_{n,\vec{k},\sigma} H_{n'\vec{k}'\sigma',n\vec{k}\sigma}\, C^{\sigma}_{n,\vec{k}} = E \sum_{n,\vec{k},\sigma} S_{n'\vec{k}'\sigma',n\vec{k}\sigma}\, C^{\sigma}_{n,\vec{k}}\,, \tag{4.4}$$

where

$$H_{n'\vec{k}'\sigma',n\vec{k}\sigma} \equiv \left\langle n'\vec{k}'\sigma'|\hat{T}+\hat{V}_{\rm xtal}|n\vec{k}\sigma\right\rangle\,,$$

$$\left\langle n'\vec{k}'\sigma'|\hat{T}|n\vec{k}\sigma\right\rangle = \delta_{\vec{k}',\vec{k}}\sum_{\vec{G}}\frac{\hbar^2}{2m}\left|\vec{G}+\vec{k}\right|^2 B^{\sigma'}_{n'\vec{k}'}\left(\vec{G}\right)^* B^{\sigma}_{n\vec{k}}\left(\vec{G}\right)\,,$$

$$\begin{aligned}\left\langle n'\vec{k}'\sigma'|\hat{V}_{\rm xtal}|n\vec{k}\sigma\right\rangle &= \sum_{\vec{G},\vec{G}'} B^{\sigma'}_{n'\vec{k}'}\left(\vec{G}\right)^* B^{\sigma}_{n\vec{k}}\left(\vec{G}\right)\\ &\quad\times\sum_{\sigma'',\alpha} V^{\sigma''}_{\alpha}\left(\left|\vec{G}+\vec{k}-\vec{G}'-\vec{k}'\right|^2\right)\\ &\quad\times W^{\sigma''}_{\alpha}\left(\vec{k}-\vec{k}'\right)e^{i\left(\vec{G}+\vec{k}-\vec{G}'-\vec{k}'\right)\cdot\vec{d}^{\sigma''}_{\alpha}}\,,\end{aligned}$$

$$S_{n'\vec{k}'\sigma',n\vec{k}\sigma} \equiv \left\langle n'\vec{k}'\sigma'|n\vec{k}\sigma\right\rangle\,.$$

Here, the atoms are on regular sites of the underlying Bravais lattice: $\vec{R}_{n_1,n_2,n_3} = n_1\vec{a}_1 + n_2\vec{a}_2 + n_3\vec{a}_3$ where $\{\vec{a}_i\}$ are its direct lattice vectors of the Bravais lattice. Both the NC and the host matrix are assumed to possess the same lattice constant and the whole structure is within a supercell which imposes the periodicity condition $W\left(\vec{R}_{n_1,n_2,n_3}+N_i\vec{a}_i\right) = W\left(\vec{R}_{n_1,n_2,n_3}\right)$, recalling its Fourier representation $W\left(\vec{R}_{n_1,n_2,n_3}\right) \rightarrow \sum\tilde{W}(q)e^{i\vec{q}\cdot\vec{R}_{n_1,n_2,n_3}}$, implies $e^{i\vec{q}\cdot N_i\vec{a}_i} = 1$, so that $\vec{q}\rightarrow\vec{q}_{m_1,m_2,m_3} = \vec{b}_1\frac{m_1}{N_1}+\vec{b}_2\frac{m_2}{N_2}+\vec{b}_3\frac{m_3}{N_3}$, where $\{\vec{b}_i\}$ are the reciprocal lattice vectors of the *bulk* material. Thus the reciprocal space of the supercell arrangement is not a continuum but is of the grid form composed of points $\{\vec{q}_{m_1,m_2,m_3}\}$, where $m_i = 0, 1, \ldots, N_i - 1$.

An important issue is the choice of the host matrix material. If the NC is surrounded by vacuum, this corresponds to the free-standing case. However, the dangling bonds of the surface NC atoms lead to quite a large number of interface states which adversely contaminate especially the effective band-gap region of the NC. In practice NCs are embedded into a wide band-gap host matrix which is usually silica [131]. However, the pseudopotential for oxygen is nontrivial in the case of EPM [133] and furthermore, lattice constant of $\mathrm{SiO_2}$ is not matched to either of the core materials introducing strain effects. Therefore, we embed the Si and Ge NCs into an *artificial* wide band-gap medium which for the former reproduces the proper band alignment of the $\mathrm{Si/SiO_2}$ system. To circumvent the strain effects which are indeed present in the actual samples, we set the lattice constant and crystal structure of the matrix equal to that of the core material. The pseudopotential form factors of the wide band-gap matrices for Si and Ge can easily be produced starting from those of the core materials [122].

4.3 Theory: Radiative Recombination

An excellent test for the validity of the electronic structure is through the computation of the direct photon emission. The radiative lifetime for the transition between HOMO and LUMO is obtained via time-dependent perturbation theory utilizing the momentum matrix element as first undertaken by Dexter [134]. However, to take into account local field effects we have used the expression offered by Califano *et al.* [135]:

$$\frac{1}{\tau_{fi}} = \frac{4}{3}\frac{n}{c^2}F\alpha\omega_{fi}^3\left|r_{fi}\right|^2 \tag{4.5}$$

where $\alpha = e^2/\hbar c$ is the fine structure constant, $n = \sqrt{\epsilon_{\text{out}}}$ is the refractive index of the surrounding medium, $F = 3\epsilon_{\text{out}}/\left(\epsilon_{\text{NC}} + 2\epsilon_{\text{out}}\right)$ is the screening factor within the real-cavity model [136, 137], ω_i is the frequency of the emitted photon, c is the speed of light, and $\left|r_{fi}\right|^2 = \langle i|p|f\rangle/m_0\omega_{fi}$ is the dipole length element between the initial and final states. We can rewrite the Eq. 4.5 as,

$$\frac{1}{\tau_{fi}} = \frac{16\pi^2}{3}nF^2\frac{e^2}{h^2m_0^2c^3}(E_f - E_i)\left|\langle i|p|f\rangle\right|^2 . \tag{4.6}$$

Using the oscillator strength (apart from some coefficients),

$$f^{ee}_{\text{osc},fi} \equiv \frac{\left|\widehat{e}\cdot\overrightarrow{P}_{fi}\right|^2}{E_{fi}}, \quad \text{where} \quad \left|\langle i|p|f\rangle\right| = \frac{2\pi\hbar}{a_{\text{cell}}}\overrightarrow{P}_{fi}, \tag{4.7}$$

the radiative recombination lifetime becomes,

$$\frac{1}{\tau_{fi}} = \frac{16\pi^2}{3} n F^2 \frac{e^2}{a_{\text{cell}}^2 m_0^2 c^3} (E_f - E_i)^2 f_{\text{osc},fi}^{ee}. \tag{4.8}$$

Finally, the Boltzmann average is performed over the states close to the HOMO and LUMO to obtain a thermally averaged radiative lifetime as

$$\frac{1}{\langle \tau_r \rangle} = \frac{\sum_{fi} \frac{1}{\tau_{fi}} e^{-(E_{fi}-E_g)/k_B T}}{\sum_{fi} e^{-(E_{fi}-E_g)/k_B T}}. \tag{4.9}$$

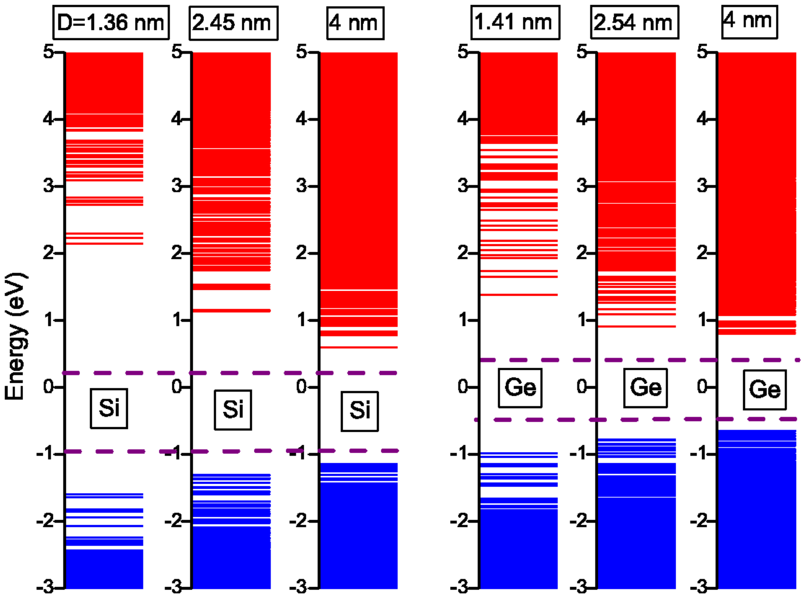

Figure 4.1: Pseudopotential atomistic energy spectra of Si and Ge NCs for different diameters. The dashed lines indicate the conduction band minimum and valence band maximum for the bulk semiconductors.

4.4 Results

The evolution of resultant electronic spectra with respect to size for embedded Si and Ge NCs is shown in Fig. 4.1. The quantum size effect is clearly visible from this figure as the HOMO (highest occupied molecular orbital) and LUMO (lowest unoccupied molecular orbital) approach the bulk valence band maximum and the conduction band minimum of the core materials (indicated by dashed lines), respectively.

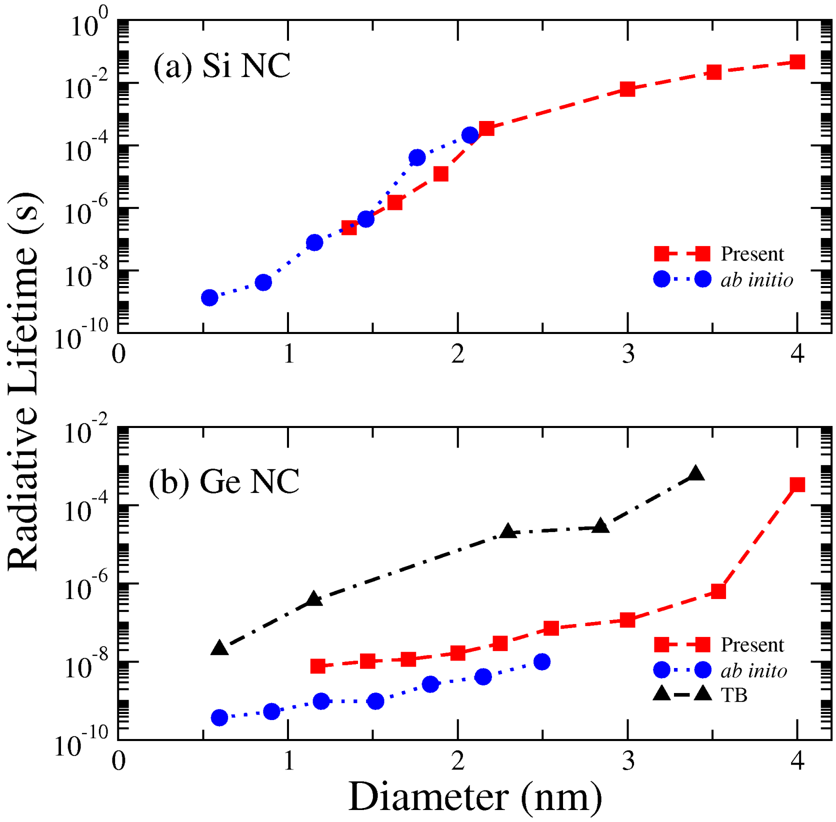

Figure 4.2: The variation of the radiative lifetime with respect to diameter for Si and Ge NCs. Our data is compared with the existing *ab initio* and tight-binding results in the literature.

Our results for the radiative lifetime in Si and Ge NCs as a function of diameter are shown in Fig. 4.2. These are in excellent agreement with the very reliable *ab initio* calculations for small NCs [38]. However, our formalism is applicable to much larger NCs as well. This is also the case with the tigh-binding approach as undertaken by Niquet *et al.* [138]. It should be noted that the radiative lifetime is reduced logarithmically as the NC size is reduced turning the indirect band-gap bulk materials into efficient radiators. In the next Chapter, we shall observe that the nonradiative processes (Auger recombination and carrier multiplication) are still much more efficient than the radiative process. As another remark, for larger NCs the level spacings become comparable to phonon energies. Therefore, the direct recombination as considered here, needs to be complemented by the phonon-assisted recombination beyond approximately 3-4 nm diameters.

Chapter 5

Auger Recombination and Carrier Multiplication in embedded Si and Ge Nanocrystals

Carrier multiplication (CM) and Auger recombination (AR) are the two most important Coulombic excitations in NCs. For Si and Ge NCs embedded in wide band-gap matrices, CM and AR lifetimes are computed exactly in a three-dimensional real space grid using empirical pseudopotential wave functions. Our results support the recent experimental data and also lead to further predictions. We extract simple Auger constants valid for NCs up to a size of at least 4 nm. We show that both Si and Ge NCs are ideal for photovoltaic efficiency improvement via CM due to the fact that under an optical excitation exceeding twice the band gap energy, the electrons gain lion's share from the total excess energy and can cause a CM. Finally, we predict the electron-initiated CM to be enhanced by couple orders of magnitude with a 1 eV of excess energy beyond the CM threshold leading to subpicosecond CM lifetimes.

5.1 Introduction

NCs can turn the indirect band-gap bulk materials into light emitters [14] or offer increased efficiencies in solar cells [139]. The latter has been demonstrated in a very recent experimental study by significantly increasing the solar cell efficiency in colloidal Si NCs due to carrier CM which enables multiple exciton generation in response to a single absorbed photon [28]. Similarly, the inverse process, AR is also operational and it introduces a competing mechanism to CM which can potentially diminish the solar cell efficiency and in the case of light sources it degrades the performance by inflating the nonradiative carrier relaxation rate [29].

In the case of the NCs, quantum-confinement enhances the AR and CM rates compared to bulk by advancing the Coulomb interaction and relaxing the translational momentum conservation [140]. Therefore, AR and CM are held largely responsible for the carrier generation and recombination occurring in quantum dots and NCs. This becomes a major obstacle particularly in the case of Si and Ge NCs, aiming for Si- and Ge-based light sources and promoting the realm of Si photonics [14]. For other semiconductor NCs as well, the AR and CM process plays a major role in carrier relaxation as demonstrated by a large number of experimental studies such as in CdS and CdSe quantum dots [141, 142, 143]. Similarly for Si NCs, the recent experimental studies addressing the importance of AR has become substantial [144, 10, 145, 146, 147, 11, 148]. Walters *et al.* have proposed a novel scheme that circumvents AR by the sequential tunneling of a hole followed by switching the gate bias to enable the tunneling of an electron into a typical NC which gives rise to a very efficient electroluminescence [11]. The same group, in another work has utilized AR as a desirable effect to switch off the photoluminescence in a Si optical NC memory [147].

The utilization and full control of both CM and AR require a rigorous theoretical understanding. Zunger *et al.* have established an empirical pseudopotential many-body approach [149, 150, 151] to calculate the lifetime of the different type of the AR in free standing and hydrogen passivated CdSe NCs (R= 29.25 and 38.46 Å) and found the results which are good agreement with Klimov *et al.* However, the pioneering series of publications on the AR in Si NCs belong to a single group based on an atomistic tight binding approach [152, 153, 154]. Unfortunately, they only considered hydrogen passivated Si NCs without addressing the shape and host matrix effects. Moreover, their results do not reveal a size-scaling for AR but rather a scattered behavior over a wide band of lifetimes in the range from few picoseconds to few nanoseconds as the NC diameter changes from 2 to 4 nm. In the past decade, no further theoretical assessment of AR in Si NCs was put forward. In this context, the Ge NCs have not received any attention although with their narrower effective band gap, they can benefit more from the low-energy part of the solar spectrum in conjunction with CM for increasing the efficiency.

In this Chapter, we provide a theoretical account of CM and AR in Si and Ge NCs which reveals their size, shape and energy dependence. Another important feature of this work, unlike commonly studied hydrogen-passivated NCs is that we consider NCs *embedded* in a wide band-gap matrix which is essential for the solid-state device realizations. Similar to the classification of Wang *et al.* in their theoretical work on Coulombic excitations in CdSe NCs [149], we consider different possibilities of AR as shown in Fig. 5.1. We use the type of the exicted carrier as the discriminating label, hence we have the excited electron (Fig. 5.1(a)) and the excited hole (Fig. 5.1(b)) AR and their biexciton variants (Fig. 5.1(c) and (d)). The latter also correspond to CM taking place in reverse direction. To calculate AR and CM in Si and Ge NCs in the next section, we briefly explain details of AR in Bulk and NC systems to clarify our method used.

5.2 Theory

Both AR and CM require an accurate electronic structure over a wide energy band extending up to at least 3-4 eV below (above) the highest occupied molecular orbital-HOMO (lowest unoccupied molecular orbital-LUMO). Another constraint is to incorporate several thousands of core and host matrix atoms within a supercell (see Fig. 5.2 (a)). To meet these requirements we have employed the linear combination of bulk bands basis within the empirical pseudopotential

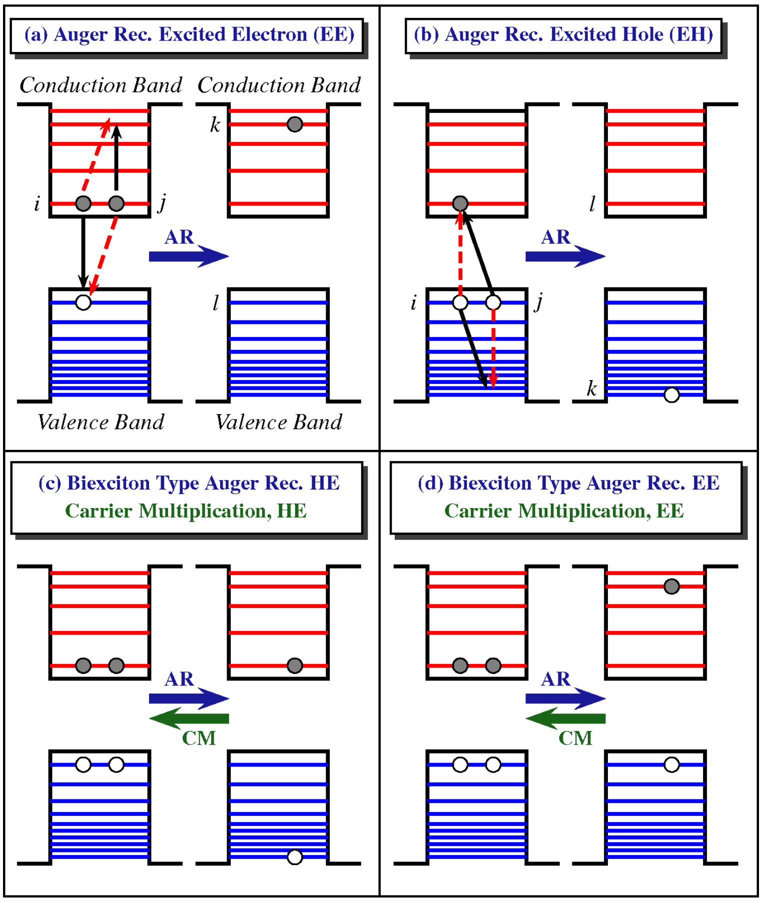

Figure 5.1: Auger recombination and carrier multiplication in nanocrystals.

framework (described in Chapter 4) which can handle thousands-of-atom systems both with sufficient accuracy and efficiency over a large energy window [23]. Details regarding its performance and the implementation such as the wide band-gap host matrix can be found in Ref. [122]. We should mention that Califano *et al.* have successfully employed a very similar theoretical approach in order to explain the hole relaxation in CdSe NCs. [155]

Detailed description of the calculation of AR and CM in NCs can be found in Appendix A. However we also briefly explain our method in this Chapter. After solving the atomistic empirical pseudopotential Hamiltonian for the energy levels and the wave functions, the AR and CM probability can be extracted using the

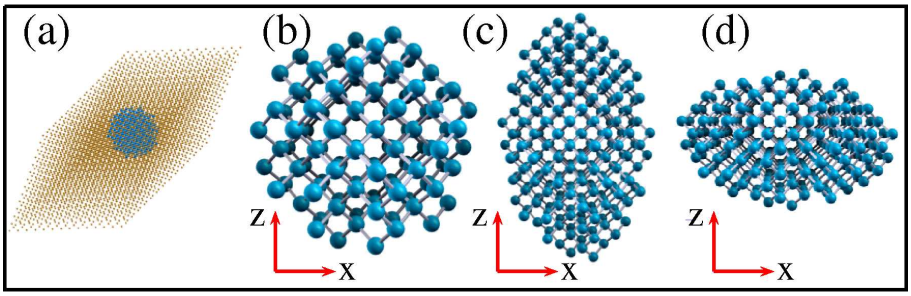

Figure 5.2: (a) Embedded NC in a supercell, core atoms of a (b) spherical, (c) oblate and (d) prolate ellipsoidal NC.

Fermi's golden rule,

$$R = \frac{\Gamma}{\hbar} \sum_{f} \frac{|\langle \psi_i \,| V_c(\mathbf{r_1}, \mathbf{r_2}) |\, \psi_f \rangle|^2}{(E_f - E_i)^2 + (\Gamma/2)^2}, \tag{5.1}$$

where ψ_i and ψ_f are respective initial and final configurations with the corresponding energies E_i and E_f, respectively, and Γ is the level broadening parameter which is taken as 10 meV. However, sensitivity to this parameter is also considered in this work. The spin-conserving screened Coulomb potential is given by $V_c(\mathbf{r_1}, \mathbf{r_2}) = e^2/\epsilon(\mathbf{r_1}, \mathbf{r_2})|\mathbf{r_1} - \mathbf{r_2}|$. Here, for the dielectric function $\epsilon(\mathbf{r_1}, \mathbf{r_2})$ past theoretical investigations [156, 149] have concluded that it is bulklike inside the NC. Therefore, we use [149],

$$\frac{1}{\epsilon(\mathbf{r_1}, \mathbf{r_2})} = \frac{1}{\epsilon_{\text{out}}} + \left(\frac{1}{\epsilon_{\text{in}}} - \frac{1}{\epsilon_{\text{out}}} \right) m(\mathbf{r_1}) m(\mathbf{r_2}), \tag{5.2}$$

as the dielectric function, where, the so-called mask function $m(\mathbf{r})$ is set to 1 when $\mathbf{r}$ inside of the NC and 0 when $\mathbf{r}$ outside of the NC.

Expressing the initial and final states of the AR shown in Fig. 5.1 (a) or (b) by using the Slater determinant, the matrix elements $(\langle \psi_i \,| V_c(|\mathbf{r_1}, \mathbf{r_2}|) |\, \psi_f \rangle)$ can be calculated as

$$\begin{aligned} M(i,j;k,l) \;\; &= \;\; \frac{1}{V^2} \int \int \phi_i^*(\mathbf{r_1}) \phi_j^*(\mathbf{r_2}) V_c(\mathbf{r_1}, \mathbf{r_2}) \\ &\quad \times (\phi_k(\mathbf{r_1}) \phi_l(\mathbf{r_2}) - \phi_k(\mathbf{r_2}) \phi_l(\mathbf{r_1})) d^3 r_1 d^3 r_2, \end{aligned} \tag{5.3}$$

here the labels i, j and k and l refer respectively to the initial and final states which also include the spin and V is volume of the supercell.

These matrix elements, $M(i,j;k,l)$ are computed exactly in a three-dimensional real space grid without resorting to any envelope approximation. The number of final states are determined setting the final state window to $\pm 7\Gamma$ around the exact conserved energy $E_k(= E_j + E_i - E_l)$. For the initial states i and l, Boltzmann average is taken into account due to thermal excitations. The other initial state j is kept fixed at LUMO for the excited electron (EE), and at HOMO for the excited hole (EH) type AR.

5.3 Results

We first apply this formalism to spherical NCs (see Fig. 5.2(b)) having abrupt interfaces. The corresponding AR lifetimes for EE and EH processes are plotted as a function of NC diameter in Fig. 5.4 (a) and (b). The C_{3v} point symmetry of the NCs in the case of abrupt interface between NC core and the matrix causes oscillations in the physical quantities such as the state splittings and the density of states (See Fig. 5.6) with respect to NC diameter [122]. When we account for the interface transition region (See Fig 5.3) between the NC and host matrix [157], we observe that these strong oscillations in the size dependence of AR are highly reduced for Si and Ge NCs (cf. Fig. 5.4). The interface region

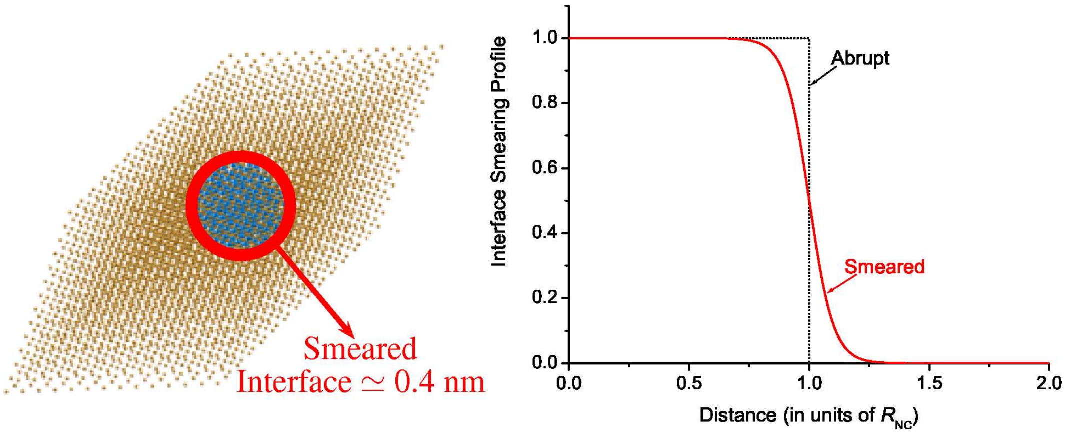

Figure 5.3: Smeared interface of Nanocrystals.

especially affects the excited state wave functions and the final state density of states and it makes our model more realistic for both Si and Ge NCs. As an observation of practical importance, we can reproduce our data remarkably well using the simple expression $1/\tau = Cn^2$, with an Auger coefficient of $C = 1\times10^{-30}$ cm^6s^{-1} for Si NCs and $C = 1.5\times10^{-30}$ cm^6s^{-1} for Ge NCs , where n is the carrier density within the NC (cf. Fig. 5.4).

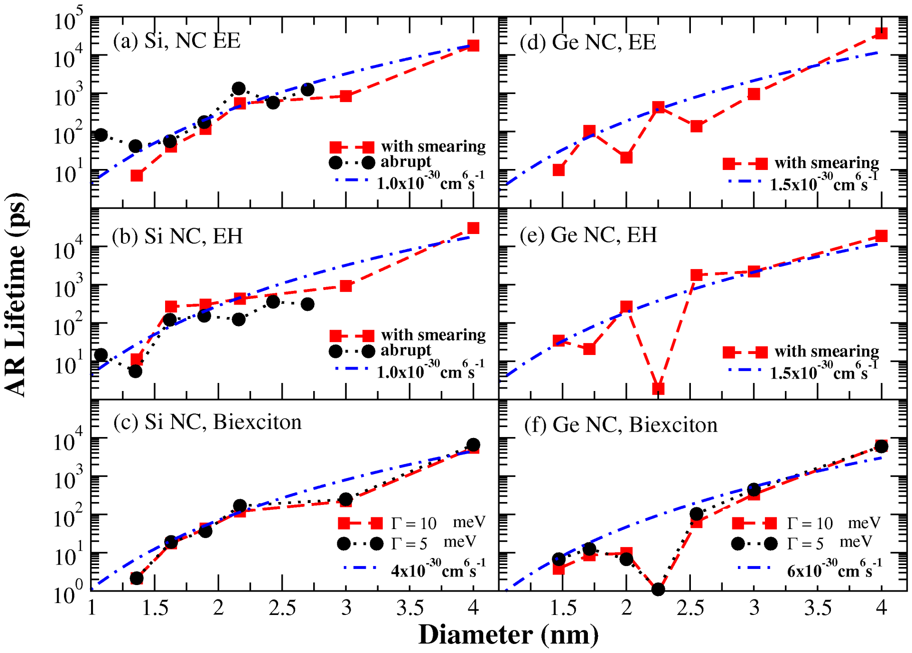

Figure 5.4: AR lifetimes for (a) excited electron, (b) excited hole, and (c) biexciton types in Si NCs, and (d) excited electron, (e) excited hole, and (f) biexciton types in Ge NCs. Square symbols represent AR lifetimes with interface smearing, and dashed lines show AR lifetimes calculated from our proposed C values. Spherical symbols in (a) and (b) represent AR lifetimes in Si NCs with abrupt interfaces.

The other two types of AR shown in Fig. 5.4 (c) and (f) refer to biexciton recombinations. This process becomes particularly important under high carrier densities such as in NC lasers or in solar cells under concentrated sunlight. Its probability can be expressed in terms of EE and EH type AR as [149], $1/\tau_{\text{XX}} = 2/\tau_{\text{EE}} + 2/\tau_{\text{EH}}$ where τ_{EE} and τ_{EH} are EE and EH lifetimes. Fig. 5.4 (c) and (f) compares the computed biexciton type AR for Si and Ge NCs with the expression $1/\tau = Cn^2$ where the value $C = 4\times10^{-30}\text{cm}^6\text{s}^{-1}$ and $6\times10^{-30}\text{cm}^6\text{s}^{-1}$ are used which are obtained from the previous C values extracted for EE and EH processes together with the τ_{XX} expression. For Si NC case, our calculated value at 3 nm diameter agrees reasonably well with the experimental photoluminescense decay time of about 105 ps which was attributed to AR [30]. In Fig. 5.4 (c) and (f), we also demonstrate the fact that a choice of $\Gamma = 5$ meV does not introduce any marked deviation from the case of $\Gamma = 10$ meV as used in this work for both Si and Ge NCs. This parameter test automatically checks the sensitivity to the final state energy window chosen as $\pm 7\Gamma$.

Next, we demonstrate the effects of deviation from sphericity on Si NCs. We consider both oblate (Fig. 5.2(c)) and prolate (Fig. 5.2(d)) ellipsoidal Si NCs described by the ellipticity values of e=0.85 and -0.85, respectively. For the comparison purposes, we preserve the same number of atoms used in spherical NCs of diameters 1.63 and 2.16 nm. The results listed in Table 5.1 indicate that the spherical NC has a lower Auger rate than the aspherical shapes. This can be reconciled as follows: in the case of either prolate or oblate NC, the electronic structure is modified in such a way that the number of final states is increased, furthermore, a coalescence of the states around the HOMO and LUMO occurs. A similar effect was also observed in the asphericity-induced enhancement of Auger thermalization of holes in CdSe NCs [155]. Another important parameter in Coulomb interactions is the choice of the host matrix. The two most common wide band-gap matrices are SiO_2 and Al_2O_3. The host matrix is expected to play two roles: dielectric confinement effects due to different permittivities of the core and the matrix ($\epsilon_{\mathrm{Si}} = 12$, $\epsilon_{\mathrm{SiO_2}} = 4$ and $\epsilon_{\mathrm{Al_2O_3}} = 9.1$) and the electronic confinement effects due to different band gaps. The results tabulated in Table 5.2 show that Al_2O_3 matrix leads to increased AR lifetime which reveals the importance of the

Table 5.1: AR lifetimes for different ellipsoidal shapes of Si NCs with diameters of 1.63 and 2.16 nm.

	Spherical		Prolate		Oblate	
D (nm)	1.63	2.16	1.63	2.16	1.63	2.16
EE (ps)	40.1	540.6	31.5	103.1	36.4	121.3
EH (ps)	267.2	430.1	74.0	76.3	26.1	139.0

Table 5.2: Comparison of AR lifetimes for SiO_2 and Al_2O_3 host matrices.

Diameter (nm)	1.63	2.16	3.00	4.00
SiO_2-EE (ps)	40.1	540.6	838.3	17580.1
Al_2O_3-EE (ps)	43.2	612.4	1177.7	23373.4
SiO_2-EH (ps)	267.2	430.1	922.1	30150.0
Al_2O_3-EH (ps)	206.5	245.1	1907.5	101942.8

dielectric confinement. The deviations from this trend for smaller NCs should be due to electronic structure effects dominating at these sizes. However, we should note that neither of the shape or matrix effects are pronounced.

In their work on the CM in PbSe NCs, Allan and Delerue have deduced that such Coulombic interactions are primarily governed by the state-density function, whereas the breaking of the momentum conservation rule due to the confinement does not lead to an enhancement of these rates [158]. Even though we agree on the importance of the density of states, we believe that such a conclusion undermines the significant role of the Coulomb matrix elements. We illustrate our point by Fig. 5.5, where the average matrix element for Si and Ge NCs are shown. The strong size dependence leading to a variation over several orders of magnitude proves their nontrivial role.

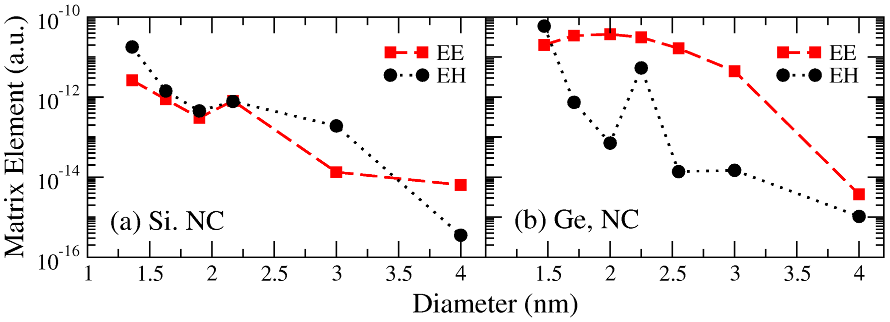

Figure 5.5: Average Coulomb matrix elements for (a) Si and (b) Ge NCs for EE type AR (red squares) and for EH type AR (black spheres).

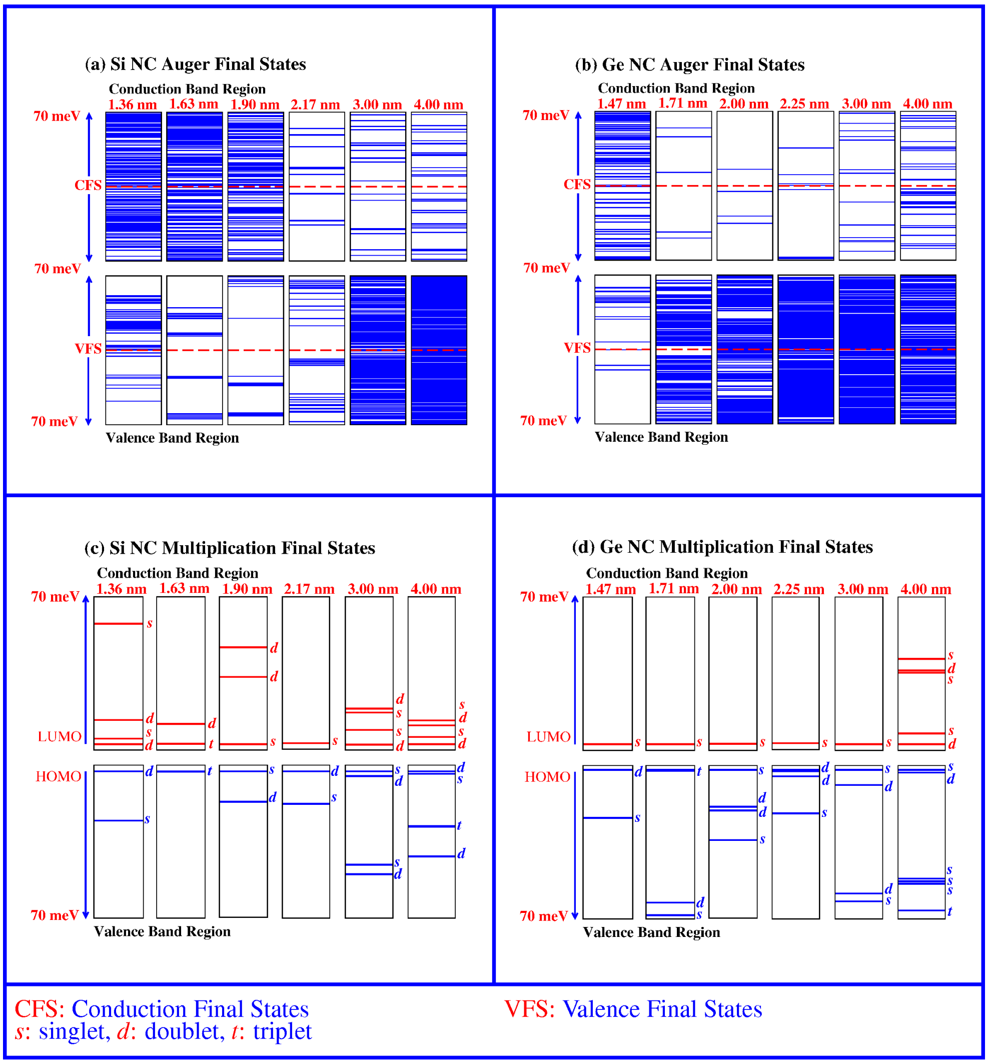

Figure 5.6: Final state configuration for, (a) AR in Si, (b) AR in Ge, (c) CM in Si and (d) CM in Ge NCs. Dashed line in (a) and (b) corresponds to exact conserved energy

Regarding the CM, to calculate the EE (EH) type CM (cf., Fig. 5.1 (c) and (d)) for different diameters of the Si and Ge NCs, first we consider the impacting electrons (holes) having the energy of E_{gap} (threshold energy to initiate a CM event) above (below) the conduction (valence) band edge. As seen in Fig. 5.7, EE and EH type CM lifetimes for Si and Ge NCs decrease from the few ns to about 1 ps as the NC diameter decreases. However, for EE (EH) type CM, the few number of final states at the bottom of the CB (top of the VB) cause a nonmonotonic dependence of CM on size of the NC (See Fig. 5.6 (c) and (d)).

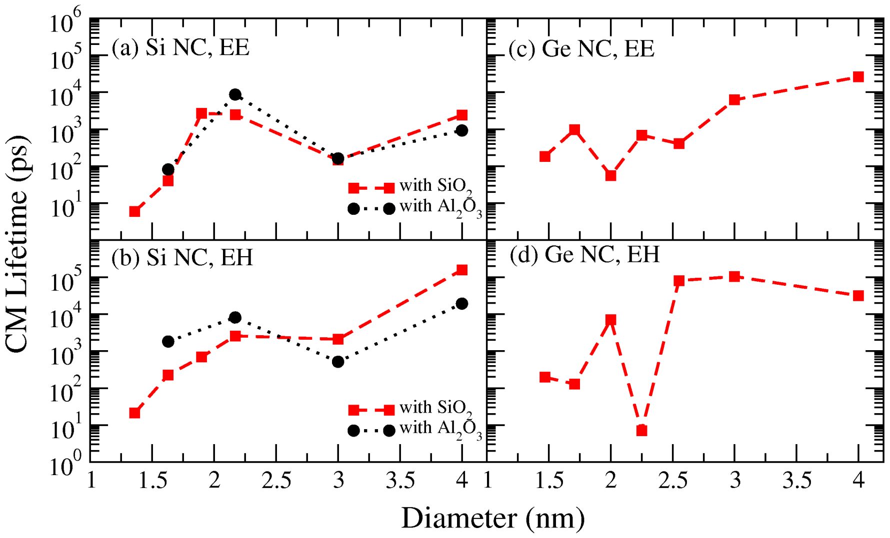

Figure 5.7: CM Lifetime results for (a) EE and (b) EH types in Si NCs embedded in SiO_2 and Al_2O_3, and (c) EE and (d) EH types in Ge NCs embedded in Al_2O_3.

Finally, we investigate the effect of excess energy on the CM under an optical excitation above the effective gap, $E_{\text{gap}} = E_{\text{LUMO}} - E_{\text{HOMO}}$. We assign the excited electron and hole to their final states based on the transition with the largest radiative oscillator strength [122]. In Fig. 5.8 (a) we observe that the electrons receive the lion's share of the total excess energy which is the desired case for the high efficiency utilization of CM in photovoltaic applications [159]. Our threshold value for Si NCs agrees very well with the recent experimental data of 2.4 E_{gap} [28]. In Fig. 5.8 (b) we show the corresponding electron-initiated CM lifetimes as a function of excess energy. It can be observed that CM is enhanced by couple orders of magnitude with a 1 eV of excess energy beyond the CM threshold leading to subpicosecond CM lifetimes. We believe that these theoretical predictions prove the strong potential of both Si and Ge NCs in utilizing CM especially for the photovoltaics and photonics applications.

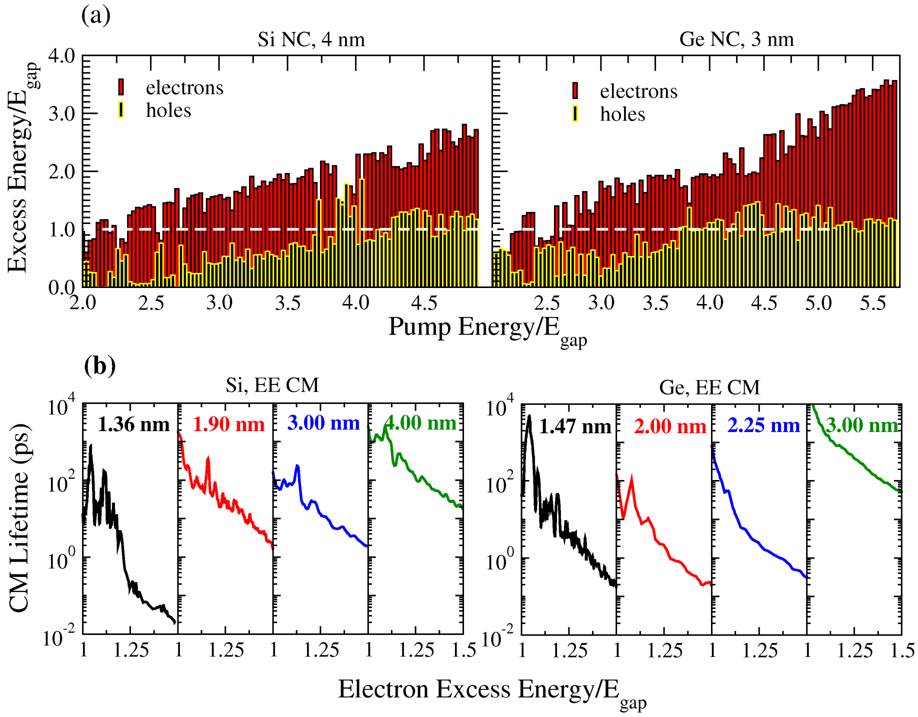

Figure 5.8: (a) Electron and hole excess energy vs pump energy for 4 nm Si and 3 nm Ge NCs, (b) CM lifetime vs electron excess energy for different diameter of Si and Ge NCs.

Chapter 6

Conclusions

Even though the group-IV semiconductors Si and to a lesser extend Ge have been the workhorse of the electronics industry in the twentieth century, the subject of group-IV NCs is just booming, thanks to their added prospects in photonics and microelwctronics. This computational thesis is devoted to the realistic assessment of their mainly radiative and non-radiative properties. Special emphasis is given to the comparison with the available theoretical and especially experimental results. In this final chapter we would like to summarize our conclusions and main achievements.

The media in which these NCs are embedded play a nontrivial role. Therefore, as the initial task to determine the electronical and structural properties of the NC host matrices, a comprehensive first-principles study is performed which is unique in analyzing common polymorphs of the technologically-important insulating oxides and nitrides: SiO_2, GeO_2, Al_2O_3, Si_3N_4, and Ge_3N_4. The structural parameters, elastic constants, static and optical dielectric constants are obtained in close agreement with the available results. The computed dielectric constants are observed to display a strong correlation with their mass densities. For all of the considered polymorphs the conduction band minima occur at the Γ point whereas the valence band maxima shift away from this point for some of the phases making them indirect band-gap matrices. However, the direct band gap values are only marginally above the indirect band gap values. The investigation of band structure and DOS data reveal that the holes in all polymorphs considered and the electrons for the case of Si_3N_4 and Ge_3N_4 should suffer excessive scatterings under high applied field which will preclude bulk impact ionization for these carrier types and polymorphs. This can be especially important for applications vulnerable to dielectric breakdown. In the course of the study related with NC host matrices, elastic constants, electronic band structures and phonon dispersion curves of the i-phase high-k oxides have been obtained with high accuracy. These calculations suggest that the new cubic-phases of GeO_2 and SnO_2 are unstable whereas SiO_2, $Si_{0.5}Ge_{0.5}O_2$, $Si_{0.5}Sn_{0.5}O_2$ are particularly promising due to their high dielectric constants as well as wide band gaps as restored by the *GW* correction. Moreover, they are lattice-matched to Si(100) face, especially for the case of $Si_{0.5}Ge_{0.5}O_2$. We believe that these findings can further boost the research on the crystalline oxides.

Next, the rate of an important high-field process known as quantum confined impact ionization (QCII) is calculated analytically. As our main contribution, we propose a closed-form expression of the QCII probability which is incorporated into the EMC high-field transport framework that involves other major scattering mechanisms. The scattering rates are computed using *ab initio* DOS for SiO_2 matrix as described in Chapter 2. Our results for a range of parameters indicate that QCII has a marginal effect on the carrier average energy and velocity characteristics both in the transient and steady-state regimes. As a possible future work in this direction, the high field phenomena in other NC host lattices, especially Al_2O_3 warrants to be similarly studied. Finally, it needs to be mentioned that we consider the QCII process that yields an electron-hole pair within the NCs. There can be other variants of this specific process (still to be named as QCII) which may have much more dramatic effect on the average carrier transport quantities leading to dielectric breakdown. In the Appendix section, these related processes are mentioned and their matrix elements are worked out analytically.

Moving away from matrices inward towards NCs, using an atomistic pseudopotential approach the electronic structures for embedded Si and Ge NCs in wide band-gap matrices containing several thousand atoms are employed. To check the validity of the electronic structure on radiative processes, direct photon emission rates are obtained. Our results for Si and Ge NCs as a function of diameter are in excellent agreement with the available *ab initio* calculations for small NCs. However, our formalism is applicable to much larger NCs as well. The main observation is that the radiative lifetime gets reduced logaritmically as the NC size is decreased, hence turning the indirect band-gap bulk materials into efficient radiators. However, when compared with the nonradiative processes AR and CM, the radiative channel is still by far inefficient as it remains above nanoseconds. As another remark, for larger NCs (typically above a diameter of 3-4 nm), the phonon-assisted recombination needs to be considered as the energy level spacings become comparable to phonon energies.

Finally, for the first time, the rate of two most important Coulombic excitations, AR and CM, in Si and Ge NCs are computed in a three-dimensional real space grid using the above pseudopotential wave functions. Our results have a very good agreement with the avaliable experimental data. It is shown that AR rates of Si and Ge NCs can be obtained remarkabely well using a simple expression $1/\tau = Cn^2$, with an Auger coefficient of $C = 1 \times 10^{-30}$ $\mathrm{cm^6 s^{-1}}$ for Si NCs and $C = 1.5 \times 10^{-30}$ $\mathrm{cm^6 s^{-1}}$ for Ge NCs. These Auger coefficients can serve for the practical needs in the utilization of this process. Under an optical excitation, final states of the excited electron and hole are obtained based on the transition with the largest radiative oscillator strength. Our results point out that for the efficiency enhancement via CM in Si and Ge NCs the prospects look positive as the hot electrons receive most of the excess energy and they can undergo a CM within few picoseconds with an only 1 eV of excess energy beyond the CM threshold. We believe that these theoretical predictions prove the strong potential of both Si and Ge NCs in utilizing CM especially for the photovoltaics and photonics applications.

Bibliography

[1] A. Zrenner, B. Frochlich, J. Brunner, and G. Abstraiter, Phys. Rev. B, **52**, 16608 (1995).

[2] L. Tsybeskov et. al. Appl. Phys. Lett. **72**, 43 (1998).

[3] L. Brus in : Light Emission in Silicon, Ed. D. J. Lockwood, Semiconductors and Semimetals, Academic Press, New York 1996.

[4] M. Kulakçı, U. Serincan, R. Turan, Semicond. Sci. Tech. **21**, 1527 (2006).

[5] S. Yerci, U. Serincan, I. Doğan, S. Tokay, M. Genisel, A. Aydınlı, R. Turan, Journ. Appl. Phys. **100**, 074301 (2006).

[6] U. V. Desnica, M. Buljan, P. Dubcek, Z. Siketic, I. B. Radovic, S. Bernstorff, U. Serincan, R. Turan, Nuclear Inst. and Meth. Phys. Res. Sec. B **249**, 843 (2006).

[7] S. Foss, T. G. Finstad, A. Dana, A. Aydınlı, Thin Sol. Films **515**, 6381 (2007)

[8] A. Dana, S. Tokay, A. Aydınlı, Mat. Sci. Semi. Proc. **9**, 848 (2006)

[9] V. S. Dneprovskii, V. I. Klimov, D. K. Okorokov, and Yu. V. Vandyshev, Solid State Commun. **81**, 227 (1992).

[10] L. Pavesi, L. Dal Negro, C. Mazzoleni, G. Franzó, and F. Priolo, Nature **408**, 440 (2000).

[11] R. J. Walters, G. I. Bourianoff, and H. A. Atwater, Nature Materials **4**, 143 (2005).

[12] H. Rong, A. Liu, R. Jones, O. Cohen, D. Hak, A. Fang, and M. Paniccia, Nature (London) **433**, 292 (2005); H. Rong, R. Jones, A. Liu, O. Cohen, D. Hak, A. Fang, and M. Paniccia, Nature (London) **433**, 725 (2005).

[13] V. Colvin, M. C. Schlaman, and A. P. Alivisatos, Nature **370**, 354 (1994).

[14] S. Ossicini, L. Pavesi, and F. Priolo, *Light Emitting Silicon for Microphotonics*, (Springer, Berlin, 2003).

[15] A. Sergio Bezerra Sombra, Solid State Commun. **88**, 305 (1993).

[16] A. Hagfeld and M. Graetzel, Chem. Rev. **95**, 49 (1995).

[17] M. Green, Third Generation Photovoltaics, Springer-Verlag, Berlin, (2006).

[18] E.S. Marstein, A.E. Gunnæs, U. Serincan, S. Jørgensen, A. Olsen, R. Turan, T.G. Finstad, Nuclear Inst. and Meth. Phys. Res. Sec. B **207**, 424 (2003).

[19] X. Gonze, J. M. Beuken, R. Caracas, F. Detraux, M. Fuchs, G. M. Rignanese, L. Sindic, M. Verstraete, G. Zerah, F. Jollet, M. Torrent, A. Roy, M. Mikami, P. Ghosez, J. Y. Raty, D. C. Allan, Comput. Mater. Sci. **25**, 478 (2002).

[20] E. O. Kane, in Handbook on Semiconductors, edited by W. Paul, Noth-Holland, Amsterdam, 1982, Vol. 1.

[21] H. Wang and G. Simmons, J. Geophys. Res. **78**, 1262 (1973).

[22] L. -W. Wang and A. Zunger, Phys. Rev. B **59**, 15806 (1999).

[23] L. W. Wang, A. Franceschetti, A. Zunger, Phys. Rev. Lett. **78**, 2819 (1997).

[24] S. Botti and L. C. Andreani, Phys. Rev. B **63**, 235313 (2001).

[25] S. Botti, N. Vast, L. Reining, V. Olevano and L. C. Andreani, Phys. Rev. B **70**, 045301 (2004).

[26] F. Chirico, A. Di Carlo and P. Lugli, Phys. Rev. B **70**, 045314 (2001).

[27] C. Bulutay, Physica E, **38**, 112 (2007).

[28] M. C. Beard, K. P. Knutsen, P. Yu, J. M. Luther, Q. Song,W. K. Metzger, R. J. Ellingson, and A. J. Nozik, Nano Lett. **7**, 2506 (2007).

[29] V. I. Klimov, J. Phys. Chem. B **110**, 16827 (2006).

[30] F. Trojánek, K. Neudert, M. Bittner, and P. Malý, Phys. Rev. B, **72**, 75365 (2005).

[31] Y. H. Xie, W. L. Wilson, H. M. Ross, J. A. Mucha, E. A. Fitzgerald, J. M. Macaulay, T. D. Harris, J. Appl. Phys. **71**, 2403 (1992).

[32] L. W. Wang and A. Zunger, J. Phys. Chem. **98**, 2158 (1994).

[33] C. Sevik, C. Bulutay, J. Mat. Sci., **42**, 6555 (2007).

[34] C. Sevik, C. Bulutay, Phys. Rev. B, **74**, 193201 (2006).

[35] C. Sevik, C. Bulutay, Mat. Sci. Semi. Proc. **9**, 1097 (2006).

[36] C. Sevik, C. Bulutay, Physica E, **38**, 118 (2007).

[37] C. Sevik, C. Bulutay, Phys. Stat. Sol. C, **4**, 635 (2007).

[38] H.-Ch. Weissker, J. Furthmüller, and F. Bechstedt, Phys. Rev. B **69**, 115310 (2004).

[39] J. Robertson, Rep. Prog. Phys. **69**, 327 (2006).

[40] F. Ay and A. Aydinli, Opt. Matl. **26**, 33 (2004).

[41] S. Hayashi, T. Nagareda, Y. Kanzawa, and K. Yamamoto, Jpn. J. Appl. Phys. **32**, 3840 (1993).

[42] F. Iacona, G. Franzó, C. Spinella, J. Appl. Phys. **87**, 1295 (2000).

[43] Y. Q. Wang, G. L. Kong, W. D. Chen, H. W. Diao, C. Y. Chen, S. B. Zhang, and X. B. Liao, Appl. Phys. Lett. **81**, 4174 (2002).

[44] U. Serincan, G. Aygun, and R. Turan, J. Lumin. **113**, 229 (2005).

[45] V. A. Volodin, E. B. Gorokhov, M. D. Efremov, D. V. Marin, and D. A. Orekhov, JETP Lett. **77**, 411 (2003).

[46] E. B. Gorokhov, V. A. Volodin, D. V. Marin, D. A. Orekhov, A. G. Cherkov, A. K. Gutakovskii, V. A. Shvets, A. G. Borisov, and M. D. Efremov, Semiconductors, **39**, 1168 (2005).

[47] V. A. Volodin, M. D. Efremov, and V. A. Gritsenko, Solid State Phenom. **57**-**58**, 501 (1997).

[48] R. F. Steimle, M. Sadd, R. Muralidhar, R. Rao, B. Hradsky, S. Straub, and B. E. White, IEEE Trans. Nanotechnology **2**, 335 (2003).

[49] S. Choi, H. Yang, M. Chang, S. Baek, H. Hwang, S. Jeon, J. Kim, and C. Kim, Appl. Phys. Lett. **86**, 251901 (2005).

[50] P. Tognini, L. C. Andreani, M. Geddo, A. Stella, P. Cheyssac, R. Kofman, A. Migliori, Phys. Rev. B **53**, 6992 (1996).

[51] Q. Wan, C. L. Lin, W. L. Liu, and T. H. Wang, Appl. Phys. Lett. **82**, 4708 (2003); Q. Wan, C. L. Lin, N. L. Zhang, W. L. Liu, G. Yang, T. H. Wang, Appl. Phys. Lett. **82**, 3162 (2003).

[52] D. I. Tetelbaum, A. N. Mikhaylov, O. N. Gorshkov, A. P. Kasatkin, A. I. Belov, D. M. Gaponova, and S. V. Morozov, Vacuum **78**, 519 (2005).

[53] I. Chambouleyron and A. R. Zanatta, J. Appl. Phys. **84** 1 (1998).

[54] S. J. Wang, J. W. Chai, J. S. Pan, A. C. H. Huan, Appl. Phys. Lett. **89**, 022105 (2006).

[55] J. D. Eshelby, Proc. R. Soc. London A **241**, 376 (1957).

[56] S. Balasubramanian, G. Ceder, and K. D. Kolenbrander, J. Appl. Phys. **79**, 4132 (1996).

[57] H.-Ch. Weissker, J. Furthmüller, and F. Bechstedt, Phys. Rev. B **65**, 155328 (2002).

[58] H.-Ch. Weissker, J. Furthmüller, and F. Bechstedt, Phys. Rev. B **67**, 165322 (2003).

[59] N. A. Efremov and S. I. Pokutnii, Soviet Phys. Solid St. **27**, 27 (1985); *ibid.,* **32**, 955 (1990).

[60] M. V. Fischetti and J. M. Higman, *Monte Carlo Device Simulation: Full Band and Beyond*, edited by K. Hess Kluwer, Dordrecht, (1991).

[61] P. Hohenberg and W. Kohn, Phys. Rev. B **136**, 864 (1964).

[62] W. Kohn and L. J. Sham, Phys. Rev. A **140**, 1133 (1965).

[63] Y. P. Li and W. Y. Ching, Phys. Rev. B **31**, 2172 (1985).

[64] Y. Xu and W. Y. Ching, Phys. Rev. B **44**, 11048 (1991).

[65] Tetelbaum D I, Mikhaylov A N, Gorshkov O N, Kasatkin A P, Belov A I, Gaponova D M, and Morozov S V, Vacuum **78**, 519 (2005); F. Liu, S. Garofalini, D. King-Smith, and D. Vanderbilt, Phys. Rev. B **49**, 12528 (1994).

[66] W Y Ching and Y N Xu, J. Am. Ceram. Soc., **77**, 404 (1994).

[67] Y. N. Xu and W. Y. Ching, Phys. Rev. B **51**, 17379 (1995).

[68] S D Mo and W Y Ching, Phys. Rev. B, **57**, 15219 (1998).

[69] T. Demuth, Y. Jeanvoine, J. Hafner, and J.G. Ángyán, J. Phys.: Condens. Matter **11**, 3833 (1999).

[70] B. Holm, R. Ahuja, Y. Yourdshahyan, B. Johansson, and B. I. Lundqvist, Phys. Rev. B **59**, 12777 (1999).

[71] D M Christie and J R Chelikowsky, Phys. Rev. B **62**, 14703 (2000).

[72] J. C. Idrobo, H. Iddir, S. Öğüt, A. Ziegler, N. D. Browning, and R. O. Ritchie, Phys. Rev. B **72**, 241301 (2005).

[73] S. Goedecker, M. Teter, and J. Huetter, Phys. Rev. B **54**, 1703 (1996).

[74] J. P. Perdew and A. Zunger, Phys. Rev. B **23**, 5048 (1981).

[75] D. M. Ceperley and B. J. Alder, Phys. Rev. Lett. **45**, 566 (1980).

[76] N. Troullier and J. L. Martins, Solid State Commun. **74**, 613 (1990); Phys. Rev. B **43**, 1993 (1991); Phys. Rev. B **43**, 8861 (1991).

[77] X. Gonze and C. Lee, Phys. Rev. B **55**, 10355 (1997).

[78] R. M. Van Ginhoven, H. Jónsson, and L. R. Corrales, Phys. Rev. B **71**, 024208 (2005).

[79] R. W. G. Wyckoff, *Crystal Structure* (Interscience, New York, 1965).

[80] W. H. Baur and A. A. Khan, Acta Crystallogr. Sec. B **27**, 2133 (1971).

[81] D. B. Balitskiĭ, O. Yu. Sil'vestrova, V. S. Balitskiĭ, Yu. V. Pisarevskiĭ,D. Yu. Pushcharovskiĭ, and E. Philippot, Crystallogr. Rep. **45**, 145 (2000).

[82] A. A. Bolzan, B. Fong, J. B. Kennedy, and Ch. J. Howard, Acta. Crystallogr. Sect. B: Struct. Sci. **B53**, 373 (1997).

[83] *Theory of the Inhomogenious Electron Gas*, edited by S. Lundqvist and N. H. March (Plenum, New York, 1983), and references therein.

[84] J. Sarnthein, A. Pasquarello, and R. Car, Phys. Rev.Lett. **74** 4682 (1995).

[85] L. Levien and C. T. Prewitt, Am. Mineral. **66**, 324 (1981).

[86] R. T. Downs and D. C. Palmer, Am. Mineral. **79**, 9 (1994).

[87] A. F. Wright and A. J. Leadbetter, Phil. Mag. **31**, 1391 (1975).

[88] M. Sugiyama, S. Endo, and K. Koto, Mineral. J. Japan **13**, 455 (1987).

[89] B K Ridley *Quantum Processes in Semiconductors* (Oxford University Press Oxford, 1999).

[90] J. Mcskimin, P. Andreatch, and R. N. Thurston, J. Appl. Phys. **36**, 1624 (1987).

[91] M. Grimsditch, A. Polian, V. Brazhkin, and D. Balitskiĭ, J. Appl. Phys. **83**, 3018 (1998).

[92] D. J. Weidner, J. D. Bass, A. E. Ringwood, and W. Sinclair, Geophys. Res. Lett. **87**, 4740 (1982).

[93] J. Watchman, Jr., E. E. Teft, D. G. Lam, Jr., and R. P. Stinchfield, J. Res. Natl. Bur. Stand. **64**, 213 (1960).

[94] R. Vogelgesang, M. Grimsditch, and J. S. Wallace, Appl. Phys. Lett. **76**, 982 (2000).

[95] J. A. Wendel and W. A. Goddard III, J. Chem. Phys. **97**, 5048 (1992).

[96] H. J. Monkhorst and J. D. Pack, Phys. Rev. B **13**, 5188 (1976).

[97] L. E. Ramos, J. Furthmüller, and F. Bechstedt, Phys. Rev. B **69**, 085102 (2004).

[98] W. L. Wyckoff, Am. J. Sci. **9**, 448 (1925); **26**, 33 (2004).

[99] W. L. Roberts *et al., Encyclopedia of Minerals*, 2d ed. (New York, Van Nostrand Reinhold, 1990).

[100] R. H. French, J. Am. Ceram. Soc. **73**, 447 (1990).

[101] Y. L. Page and P. Saxe,Phy. Rev. B **65**, 104104 (2002).

[102] J. Weiss, Annu. Rev. Mater. Sci. **11**, 381 (1981).

[103] J. Dong, O. F. Sankey, S. K. Deb, G. Wolf, and P. F. McMillan, Phys. Rev. B **61**, 11979 (2000).

[104] D. W. Kim, T. Kim, S. K. Banerjee, IEEE Trans. Electron Devices, **50**, 1823 (2003); M. She, T. J. King, IEEE Trans. Electron Devices, **50**, 1934 (2003).

[105] Z. Yu, Y. Liang, C. Overgaard, X. Hu, J. Curless, H. Li, Y. Wei, B. Craigo, D. Jordan, R. Droopad, J. Finder, K. Eisenbeiser, D. Marshall, K. Moore, J. Kulik, P. Fejes, Thin Solid Films **462**, 51 (2004).

[106] L. Ouyang and W. Y. Ching, Phys. Stat. Sol. (b), **242**, R64 (2005).

[107] The latest edition of the ITRS roadmap can be found at http://public.itrs.net

[108] R. M. Martin, Electronic Structure, Cambridge University Press, Cambridge, 2004.

[109] D. Alf́le, (1998). Program available at http://chianti.geol.ucl.ac.uk/∼dario/

[110] W. G. Aulbur, L. Jonsson, J. W. Wilkins, Solid State Physics **54**, 1 (2000).

[111] L. Hedin, Phys. Rev. **139**, A796 (1965).

[112] K. J. Hubbard, D. G. Schlom, J. Materials Research **11**, 2757 (1996).

[113] A. Pasquarello, M. S. Hybertsen, and R. Car, Nature (London) **396**,58 (1998).

[114] C. Sevik and C. Bulutay, Appl. Phys. Lett., **83**, 1382 (2003).

[115] C. Bulutay, B. K. Ridley, and N. A. Zakhleniuk, Phys. Rev. B, **68**, 115205 (2003).

[116] J. Sarnthein, A. Pasquarello, and R. Car, Phys. Rev. Lett., **74**, 4682 (1995).

[117] D. Arnold, E. Cartier, and D. J. DiMaria, Phys. Rev. B, **49**, 10278 (1994).

[118] B. Kehrer, W. Quade, and E. Schll, Phys. Rev. B, **51**, 7725 (1995).

[119] J. J. Sakurai, Modern Quantum Mechanics, Addison-Wesley, New York, 1994.

[120] S. Öğüt, R. Burdick, and Y. Saad, and J. R. Chelikowsky, Phys. Rev. Lett., **90**, 127401 (2003).

[121] G. Franzó, A. Irrera, E. C. Moreira, M. Miritello, F. Iacona, D. Sanfilippo, G. Di Stefano, P. G. Fallica, and F. Priolo, Appl. Phys. A, **74**, 1 (2002).

[122] C. Bulutay, Phys. Rev. B **76**, 205321 (2007).

[123] M. Luppi and S. Ossicini, Phys. Rev. B **71**, 035340 (2005).

[124] L. E. Ramos, H.-Ch. Weissker, J. Furthmuller and F. Bechstedt, Phys. Status Solidi B **242**, 3053 (2005).

[125] D. Melnikov and J. R. Chelikowsky, Solid State Commun. **127**, 361 (2003); D. Melnikov and J. R. Chelikowsky, Phys. Rev. B **69**, 113305 (2004).

[126] A. Tsolakidis and R. M. Martin, Phys. Rev. B **71**, 125319 (2005).

[127] F. Trani, G. Cantele, D. Ninno, and G. Iadonisi, Phys. Rev. B **72**, 075423 (2005).

[128] C. Delerue and M. Lannoo, Nanostructures: Theory and Modelling, Springer-Verlag, Berlin, (2004).

[129] S. Y. Ren, Phys. Rev. B **55**, 4665 (1997); S. Y. Ren, Solid State Comm. **102**, 479 (1997).

[130] L. -W. Wang and A. Zunger, J. Chem. Phys. **100**, 2394 (1994).

[131] Iacona, G. Franzo, C. Spinella, J. Appl. Phys. **87**, 1295 (2000).

[132] P. Friedel, M. S. Hybertsen, and M. Schlüter, Phys. Rev. B **39**, 7974 (1989).

[133] J. R. Chelikowsky, Solid State Commun. **22**, 351 (1977).

[134] D. L. Dexter, Solid State Physics (Academic Press Inc., New York), **6**, 358 (1958).

[135] M. Califano, A. Franceshetti, and A. Zunger, Nano Lett. **5**, 2360 (2005).

[136] R. J. Glauber and . Lewenstein Phys. Rev. A **43**, 467 (1991).

[137] C.K. Duan, M.F. Reid, and Z. Wang, Phys. Lett. A **343**, 474 (2005).

[138] Y. M. Niquet, G. Allan, C. Delerue, and M. Lannoo, Appl. Phys. Lett. **77**, 1182 (2000).

[139] M. C. Hanna and A. J. Nozik, J. Appl. Phys. **100**, 074510 (2006).

[140] C. Delerue, G. Allan and M. Lannoo, Semiconductor and Semimetals, **49**, 253 (1998).

[141] V. I. Klimov and D. W. McBranch, Phys. Rev. B, **55**, 13173 (1997).

[142] V. Klimov, P. Haring-Bolivar, and H. Kurz, Phys. Rev. B **53**, 1463 (1996).

[143] V. I. Klimov, A. A. Mikhailovsky, D. W. McBranch, C. A. Leatherdale, and M. G. Bawendi, Science **287**, 1011 (2000).

[144] R. M'ghaïeth, H. Maâref, I. Mihalcescu, and J. C. Vial, Phys. Rev. B **60**, 4450 (1999).

[145] A. Irrera, D. Pacifici, M. Miritello, G. Franzò, F. Priolo, F. Iacona, D. Sanfilippo, G. Di Stefano, and P. G. Fallica, Appl. Phys. Lett. **81**, 1866 (2002).

[146] F. Cichos, J. Martin and C. von Borczyskowski, Phys. Rev. B **70**, 115314 (2004).

[147] R. J. Walters, P. G. Kik, J. D. Casperson, H. A. Atwater, R. Lindstedt, M. Giorgi, and G. Bourianoff, Appl. Phys. Lett. **85**, 2622 (2004).

[148] I. Sychugov, R. Juhasz, J. Linnros, and J. Valenta, Phys. Rev. B **71**, 115331 (2005).

[149] L. W. Wang, M. Califano, A. Zunger, A. Franceschetti, Phys. ReV. Lett. **91**, 056404 (2003).

[150] M. Califano, A. Zunger, A. Franceschetti, Apl. Phys. Lett. **84**, 2409 (2004).

[151] A. Zunger, Phys. Status Solidi B **224**, 727 (2001).

[152] I. Mihalcescu, J. C. Vial, A. Bsiesy, F. Muller, R. Romestain, E. Martin, C. Delerue, M. Lannoo, and G. Allan, Phys. Rev. B **51**, 17605 (1995).

[153] C. Delerue, M. Lannoo, G. Allan, E. Martin, I. Mihalcescu, J. C. Vial, R. Romestain, F. Muller and A. Bsiesy, Phys. Rev. Lett. **75**, 2228 (1995).

[154] M. Lannoo, C. Delerue, and G. Allan, J. Lumin. **70**, 170 (1996).

[155] M. Califano, G. Bester, and A. Zunger, Nano Lett. **3**, 1197 (2003).

[156] G. Allan, C. Delerue, M. Lannoo, and E. Martin, Phys. Rev. B **52**, 11982 (1995).

[157] N. Daldosso *et al.* Phys. Rev. B, **68**, 085327 (2003).

[158] G. Allan and C. Delerue, Phys. Rev. B **73**, 205423 (2006).

[159] J. H. Werner, S. Kolodinski, and H. J. Queisser, Phys. Rev. Lett. **72**, 3851 (1994).

[160] C. Delerue, M. Lannoo, and G. Allan, Phys. Rev. B **68**, 115411 (2003).

[161] L. W. Wang and A. Zunger, Phys. Rev. Lett. **73**, 1039 (1994).

[162] R. Tsu and D. Babic, Appl. Phys. Lett. **64**, 1806 (1994).

[163] M. Lannoo, C. Delerue and G. Allan, Phys. Rev. Lett. **74**, 3415 (1995).

[164] T. D. Krauss and L. E. Brus, Phys. Rev. Lett. **83**, 4840 (1999); **84**, 1638(E) (2000).

[165] V. A. Fonoberov E. P. Pokatilov, and A. A. Balandin Phys. Rev. B **66**, 85310 (2002).

[166] X. Cartoixà and L. W. Wang, Phys. Rev. Lett. **94**, 236804 (2005).

Appendix A

Technical Details for Bulk Carrier-Initiated Impact Ionization Processes in Nanocrystals

In this appendix, we would like to provide the technical details on the manipulations for the quantum-confined impact ionization (See Fig. A.1 (a)) and other related possible processes multiplication (See Fig. A.1 (b)) and direct tunnelling (See Fig. A.1 (c)) in more detail for documentation purposes.

A.0.1 Quantum-Confined Impact Ionization

To explain the derivation of the probability of the quantum confined impact ionization (QCII) (See Fig. A.1 (a)) in nanocrystals (NC) we assume the impacting carrier to be an electron, however all of the formulation can be reiterated by starting with an impacting high energy hole in SiO_2.

Here we assuming that above the mobility edge which is well satisfied for an

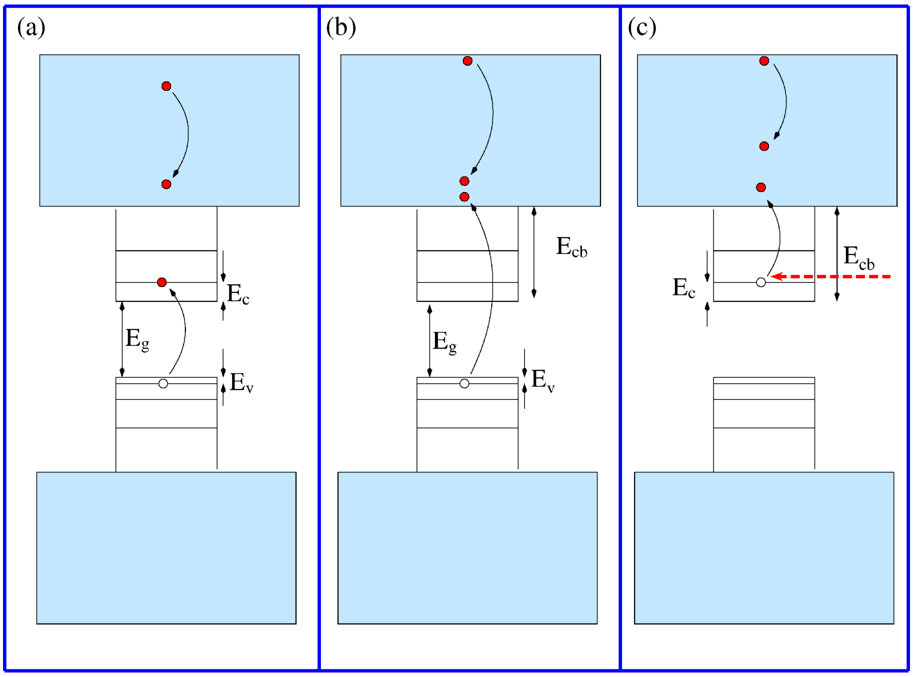

Figure A.1: A schematic illustration of the (a) QCII, (b) multiplication and (c) direct tunnelling processes in nanocrystals.

energetic electron in SiO$_2$ the bulk SiO$_2$ wavefunction is taken as

$$\psi_b = \frac{1}{\sqrt{V}} u_k(\mathbf{r}) e^{i\mathbf{k}\cdot\mathbf{r}}, \tag{A.1}$$

and the nanocrystal wavefunction as

$$\psi_n = \frac{\alpha_v^{3/2}}{\sqrt{\pi}} u_v(\mathbf{r}) e^{-\alpha_v|\mathbf{r}|}. \tag{A.2}$$

Here, we are neglecting the exchange interaction between the impacting electron and the valance nanocrystal electron due to huge energy difference between them [119]. Scattering matrix element can be written as,

$$\begin{aligned} M &= \int d^3\mathbf{r_1} \int d^3\mathbf{r_2} \frac{\alpha_c^{3/2}}{\sqrt{\pi}} u_c^*(\mathbf{r_1}) e^{-\alpha_c|\mathbf{r_1}|} \frac{1}{\sqrt{V}} u_{k'}^*(\mathbf{r_2}) e^{-i\mathbf{k}'\cdot\mathbf{r_2}} \frac{e^2}{4\pi\epsilon\epsilon_0} \frac{e^{-\lambda|\mathbf{r_1}-\mathbf{r_2}|}}{|\mathbf{r_1}-\mathbf{r_2}|} \\ & \frac{1}{\sqrt{V}} u_k(\mathbf{r_2}) e^{i\mathbf{k}\cdot\mathbf{r_2}} \frac{\alpha_v^{3/2}}{\sqrt{\pi}} u_v(\mathbf{r_1}) e^{-\alpha_v|\mathbf{r_1}|}, \end{aligned} \tag{A.3}$$

$$M = \frac{e^2\alpha_c^{3/2}\alpha_v^{3/2}}{4\pi^2\epsilon\epsilon_0 V} \int_{cell} u_c^*(\mathbf{r_1}) u_v(\mathbf{r_1}) d^3\mathbf{r_1} \int_{cell} u_{k'}^*(\mathbf{r_2}) u_k(\mathbf{r_2}) d^3\mathbf{r_2}$$

$$\times \quad \int\int d^3\mathbf{r_1} d^3\mathbf{r_2} e^{-\alpha_c|\mathbf{r_1}|} e^{-i\mathbf{k}'\cdot\mathbf{r_2}} \frac{e^{-\lambda|\mathbf{r_1}-\mathbf{r_2}|}}{|\mathbf{r_1}-\mathbf{r_2}|} e^{i\mathbf{k}\cdot\mathbf{r_2}} e^{-\alpha_v|\mathbf{r_1}|}. \tag{A.4}$$

where we can define

$$F_{cv} = \int_{cell} u_c^*(\mathbf{r_1}) u_v(\mathbf{r_1}) d^3\mathbf{r_1}, \tag{A.5}$$

$$F_{k'k} = \int_{cell} u_{k'}^*(\mathbf{r_2}) u_k(\mathbf{r_2}) d^3\mathbf{r_2}. \tag{A.6}$$

The first overlap is zero for direct band gap semiconductors, however, it does not vanish for Si where u_v derives from valence band maximum states at Γ and u_c derives mainly from conduction band minimum states arount 0.85X. If $\mathbf{r_{12}} = \mathbf{r_1} - \mathbf{r_2}$, $\mathbf{r_2} = \mathbf{r_1} - \mathbf{r_{12}}$, scattering matrix yields,

$$\begin{aligned} M &= \frac{e^2\alpha_c^{3/2}\alpha_v^{3/2}F_{cv}F_{k'k}}{4\pi^2\epsilon\epsilon_0 V} \int\int d^3\mathbf{r_1} d^3\mathbf{r_{12}} e^{-\alpha_c|\mathbf{r_1}|} e^{-i\mathbf{k}'\cdot\mathbf{r_1}} e^{i\mathbf{k}'\cdot\mathbf{r_{12}}} \\ & \frac{e^{-\lambda|\mathbf{r_{12}}|}}{|\mathbf{r_{12}}|} e^{i\mathbf{k}\cdot\mathbf{r_1}} e^{-i\mathbf{k}\cdot\mathbf{r_{12}}} e^{-\alpha_v|\mathbf{r_1}|}, \end{aligned} \tag{A.7}$$

$$\begin{aligned} M &= \frac{e^2\alpha_c^{3/2}\alpha_v^{3/2}F_{cv}F_{k'k}}{4\pi^2\epsilon\epsilon_0 V} \int d^3\mathbf{r_{12}} e^{-i(\mathbf{k}-\mathbf{k}')\cdot\mathbf{r_{12}}} \frac{e^{-\lambda|\mathbf{r_{12}}|}}{|\mathbf{r_{12}}|} \\ &\times \int d^3\mathbf{r_1} e^{-i(\mathbf{k}'-\mathbf{k})\cdot\mathbf{r_1}} e^{-(\alpha_c+\alpha_v)|\mathbf{r_1}|}. \end{aligned} \tag{A.8}$$

In the scattering matrix we have two independent integrals, the solution of the first one

$$\int d^3\mathbf{r_{12}} e^{-i(\mathbf{k}-\mathbf{k}')\cdot\mathbf{r_{12}}} \frac{e^{-\lambda|\mathbf{r_{12}}|}}{|\mathbf{r_{12}}|}, \tag{A.9}$$

can be evaluated by setting $q = -k' + k$ we can write,

$$I \equiv \int d^3r e^{-iq\cdot r} \frac{e^{-\lambda|r|}}{|r|}, \tag{A.10}$$

$$I = \int d\phi \int d(\cos\theta) \int dr r^2 e^{-iq\cdot r} \frac{e^{-\lambda|r|}}{|r|}, \tag{A.11}$$

$$I = 2\pi \int dr r e^{-\lambda|r|} \int d(\cos\theta) e^{-iqr\cos\theta}, \tag{A.12}$$

$$I = 2\pi \int dr r e^{-\lambda|r|} \frac{1}{iqr} \left[e^{iqr} - e^{-iqr} \right] \tag{A.13}$$

$$I = \frac{2\pi}{iq} \left[\int dr e^{(-\lambda+iq)|r|} - e^{(-\lambda-iq)|r|} \right], \tag{A.14}$$

$$I = \frac{2\pi}{iq} \left[\frac{1}{(-\lambda+iq)} - \frac{1}{(-\lambda-iq)} \right], \tag{A.15}$$

$$I = \frac{2\pi}{iq} \left[\frac{(-\lambda-iq)-(-\lambda+iq)}{\lambda^2+q^2} \right], \tag{A.16}$$

$$I = -\frac{4\pi}{\lambda^2+q^2} = -\frac{4\pi}{[|\mathbf{k}-\mathbf{k}'|^2+\lambda^2]}. \tag{A.17}$$

The solution of the second integral given by

$$\int d^3\mathbf{r_1} e^{-i(\mathbf{k}'-\mathbf{k})\cdot\mathbf{r_1}} e^{-(\alpha_c-\alpha_v)|\mathbf{r_1}|}, \tag{A.18}$$

can be evaluated by setting $\alpha = \alpha_c + \alpha_v$ and $q' = k' - k$, we can write,

$$II \equiv \int d^3 r_1 e^{-iq' r_1 \cos\theta} e^{-\alpha|r_1|}, \tag{A.19}$$

$$II = \int d\phi \int d(\cos\theta) \int r_1^2 dr_1 e^{-iq' r_1 \cos\theta} e^{-\alpha|r_1|}, \tag{A.20}$$

$$II = 2\pi \int r_1^2 dr_1 e^{-\alpha|r_1|} \int d(\cos\theta) e^{-iq' r_1 \cos\theta}, \tag{A.21}$$

$$II = 2\pi \int r_1^2 dr_1 e^{-\alpha|r_1|} \frac{2\pi}{iq' r_1} \left[e^{iq' r_1} - e^{-iq' r_1} \right], \tag{A.22}$$

$$II = \frac{2\pi}{iq'} \int r_1 dr_1 \left[e^{(-\alpha+iq')|r_1|} - e^{(-\alpha-iq')|r_1|} \right], \tag{A.23}$$

$$II = \frac{2\pi}{iq'} \left[\frac{1}{(\alpha+iq')^2} - \frac{1}{(\alpha-iq')^2} \right], \tag{A.24}$$

$$II = \frac{2\pi}{iq'} \left[\frac{(\alpha^2 - q'^2 + 2i\alpha q') - (\alpha^2 - q'^2 - 2i\alpha q')}{(\alpha^2+q'^2)^2} \right], \tag{A.25}$$

$$II = \frac{2\pi}{iq'}\frac{4i\alpha q'}{(q'^2+\alpha^2)^2}, \tag{A.26}$$

$$II = \frac{8\pi\alpha}{(q'^2+\alpha^2)^2} = \frac{8\pi\alpha}{[|\mathbf{k}-\mathbf{k}'|^2+\alpha^2]^2}. \tag{A.27}$$

With the solution of these two integrals the square of the matrix element can be obtained as,

$$|M|^2 = \left[\frac{64e^4\alpha_c^3\alpha_v^3\alpha^2}{(\epsilon\epsilon_0 V)^2}\right]|F_{cv}|^2|F_{k'k}|^2\frac{1}{[|\mathbf{k}-\mathbf{k}'|^2+\lambda^2]^2}\frac{1}{[|\mathbf{k}-\mathbf{k}'|^2+\alpha^2]^4}. \tag{A.28}$$

With this matrix element we can calculate the probability as,

$$P(k) = \sum_{nc}\sum_{k'}\frac{2\pi}{\hbar}|M|^2\delta\left[\frac{\hbar^2k^2}{2m_k} - E_v - E_c - E_g - \frac{\hbar^2k'^2}{2m_{k'}}\right]f_{nc}, \tag{A.29}$$

$$\begin{aligned} P(k) &= \sum_{nc}\sum_{k'}\frac{2\pi}{\hbar}\frac{2m_{k'}}{\hbar^2}|M|^2\delta\left[\frac{m_{k'}k^2}{m_k} - \frac{2m_{k'}E_v}{\hbar^2} - \frac{2m_{k'}E_c}{\hbar^2}\right. \\ &- \left.\frac{2m_{k'}E_g}{\hbar^2} - k'^2\right]f_{nc}. \end{aligned} \tag{A.30}$$

Now, lets assume that all of the NC states are avaliable for QCII

$$\sum_{nc} f_{nc} = N_{nc} = nV, \tag{A.31}$$

where n is the density per unit volume and in terms of the NC filling ratio n is

$$n = \frac{f}{V_{nc}}, \tag{A.32}$$

where E_g is that bandgap of the NC which is absorbed into the value of E_c. Here E_v is taken as positive hole energy. Writing the $A^2 = \frac{m_{k'}k^2}{m_k} - \frac{2m_{k'}E_v}{\hbar^2} - \frac{2m_{k'}E_c}{\hbar^2} - \frac{2m_{k'}E_g}{\hbar^2}$, the probability can be written as

$$P(k) = \sum_{k'}\frac{4\pi m_{k'}}{\hbar^3}|M|^2\delta\left[A^2 - k'^2\right]nV. \tag{A.33}$$

There is no spin summation as the Coulomb interaction preserves spin. The integral form of the probability can be written as,

$$P(k) = \frac{V}{(2\pi)^3}\int d^3\mathbf{k}'\frac{4\pi m_{k'}}{\hbar^3}|M|^2\delta\left[A^2 - k'^2\right]nV, \tag{A.34}$$

$$\begin{aligned} P(k) &= \frac{V}{(2\pi)^3}\int d^3\mathbf{k}'\,\frac{4\pi m_{k'}}{\hbar^3}\left[\frac{64e^4\alpha_c^3\alpha_v^3\alpha^2}{(\epsilon\epsilon_0 V)^2}\right]|F_{cv}|^2|F_{k'k}|^2 \\ &\times \frac{1}{[|\mathbf{k}-\mathbf{k}'|^2+\lambda^2]^2}\frac{1}{[|\mathbf{k}-\mathbf{k}'|^2+\alpha^2]^4}\delta\left[A^2-k'^2\right]nV, \end{aligned} \tag{A.35}$$

$$\begin{aligned} P(k) &= \int d^3\mathbf{k}'\left[\frac{32e^4\alpha_c^3\alpha_v^3\alpha^2 m_{k'}}{\hbar^3\pi^2 V(\epsilon\epsilon_0)^2}\right]|F_{cv}|^2|F_{k'k}|^2\frac{1}{[|\mathbf{k}-\mathbf{k}'|^2+\lambda^2]^2} \\ &\times \frac{1}{[|\mathbf{k}-\mathbf{k}'|^2+\alpha^2]^4}\delta\left[A^2-k'^2\right]nV, \end{aligned} \tag{A.36}$$

$$C = \left[\frac{32e^4\alpha_c^3\alpha_v^3\alpha^2 m_{k'}}{\hbar^3\pi^2(\epsilon\epsilon_0)^2}\right]|F_{cv}|^2|F_{k'k}|^2 n, \tag{A.37}$$

$$\begin{aligned} P(k) &= \int d^3\mathbf{k}'\,C\frac{1}{[|\mathbf{k}-\mathbf{k}'|^2+\lambda^2]^2}\frac{1}{[|\mathbf{k}-\mathbf{k}'|^2+\alpha^2]^4} \\ &\times \delta\left[A^2-k'^2\right] \end{aligned} \tag{A.38}$$

$$\begin{aligned} P(k) &= \frac{\pi}{|A|}\int dx\int dk'\,k'^2 C\frac{1}{[k^2+k'^2-2kk'x+\lambda^2]^2} \\ &\times \frac{1}{[k^2+k'^2-2kk'x+\alpha^2]^4}\delta\left[|A|-k'\right], \end{aligned} \tag{A.39}$$

$$\begin{aligned} P(k) &= \pi|A|C\int dx\frac{1}{[k^2+|A|^2-2k|A|x+\lambda^2]^2} \\ &\times \frac{1}{[k^2+|A|^2-2k|A|x+\alpha^2]^4}, \end{aligned} \tag{A.40}$$

$u = k^2+|A|^2-2k|A|x$, $du = -2k|A|dx$

$$P(k) = -\frac{\pi C}{2k}\int_{(k+|A|)^2}^{(k-|A|)^2} du\frac{1}{[u+\lambda^2]^2}\frac{1}{[u+\alpha^2]^4}, \tag{A.41}$$

After solving this integral the final probability expression is obtained as,

$$\begin{aligned} P(k) &= -\frac{\pi C}{2k}\frac{1}{3(\alpha^2-\lambda^2)^5}\left[-\frac{9(\alpha^2-\lambda^2)}{(|A|-k)^2+\alpha^2}+\frac{9(\alpha^2-\lambda^2)}{(|A|+k)^2+\alpha^2}\right. \\ &- \frac{3(\alpha^2-\lambda^2)^2}{((|A|-k)^2+\alpha^2)^2}+\frac{3(\alpha^2-\lambda^2)^2}{((|A|+k)^2+\alpha^2)^2}-\frac{(\alpha^2-\lambda^2)^3}{((|A|-k)^2+\alpha^2)^3} \\ &+ \frac{(\alpha^2-\lambda^2)^3}{((|A|+k)^2+\alpha^2)^3}-\frac{3(\alpha^2-\lambda^2)}{((|A|-k)^2+\lambda^2)}+\frac{3(\alpha^2-\lambda^2)}{((|A|+k)^2+\lambda^2)} \\ &+ \left. 12\ln\left\{\frac{[(|A|-k)^2+\alpha^2]\,[(|A|+k)^2+\lambda^2]}{[(|A|+k)^2+\alpha^2]\,[(|A|-k)^2+\lambda^2]}\right\}\right]. \end{aligned} \tag{A.42}$$

A.0.2 Multiplication Process

We can write the matrix element for the other multiplication process in Fig. A.1 (b) as

$$\begin{aligned} M_t &= \int\int d^3r_1 d^3r_2 \frac{1}{\sqrt{V}} U^*_{k''}(r_1) e^{-ik''\cdot r_1} \frac{1}{\sqrt{V}} U^*_{k'}(r_2) e^{-ik'\cdot r_2} \frac{1}{4\pi\epsilon\epsilon_0} \frac{e^2}{|r_1 - r_2|} \\ &\times\ e^{-\lambda|r_1-r_2|} \frac{1}{\sqrt{V}} U_k(r_2) e^{ik\cdot r_2} U_v(r_1) \frac{\alpha_v^{3/2}}{\sqrt{\pi}} e^{-\alpha_v|r_1|}, \end{aligned} \tag{A.43}$$

$$\begin{aligned} M_t &= \frac{e^2 \alpha_v^{3/2}}{4\pi\epsilon\epsilon_0 V^{3/2}\sqrt{\pi}} \int\limits_{cell} U^*_{k''}(r_1) U_v(r_1) d^3r_1 \int\limits_{cell} U^*_{k'}(r_2) U_k(r_2) d^3r_2 \int\int d^3r_1 d^3r_2 \\ &\times\ e^{-ik''\cdot r_1} e^{-ik'\cdot r_2} \frac{e^{-\lambda|r_1-r_2|}}{|r_1-r_2|} e^{ik\cdot r_2} e^{-\alpha_v|r_1|}, \end{aligned} \tag{A.44}$$

$$F_{k''v} = \int\limits_{cell} U^*_{k''}(r_1) U_v(r_1) d^3r_1, \tag{A.45}$$

$$F_{k''k} = \int\limits_{cell} U^*_{k'}(r_2) U_k(r_2) d^3r_2, \tag{A.46}$$

$$\begin{aligned} M_t &= \frac{e^2 \alpha_v^{3/2}}{4\pi\epsilon\epsilon_0 V^{3/2}\sqrt{\pi}} F_{k''v} F_{k'k} \int\int d^3r_1 d^3r_2 e^{-ik''\cdot r_1} e^{-ik'\cdot r_2} \\ &\frac{e^{-\lambda|r_1-r_2|}}{|r_1-r_2|} e^{ik\cdot r_2} e^{-\alpha_v|r_1|}, \end{aligned} \tag{A.47}$$

If we write $r_{12} = r_1 - r_2$ and $r_2 = r_1 - r_{12}$ the matrix element yields,

$$\begin{aligned} M_t &= \frac{e^2}{4\pi\epsilon\epsilon_0 V^{3/2}} \frac{\alpha_v^{3/2}}{\sqrt{\pi}} F_{k''v} F_{k'k} \int\int d^3r_1 d^3r_{12} e^{-ik''\cdot r_1} e^{-ik'\cdot r_1} e^{ik'\cdot r_{12}} \\ &\frac{e^{-\lambda|r_1-r_2|}}{|r_1-r_2|} e^{-ik\cdot r_{12}} e^{ik\cdot r_1} e^{-\alpha_v|r_1|}. \end{aligned} \tag{A.48}$$

For the scattering matrix we have two independent integrals, the solution of the first one can be found as,

$$I \equiv \int d^3r_{12} e^{ik'\cdot r_{12}} \frac{e^{-\lambda|r_1-r_2|}}{|r_1-r_2|} e^{-ik\cdot r_{12}}, \tag{A.49}$$

$$I = \int d^3r_{12} e^{-i(-k'+k)\cdot r_{12}} \frac{e^{-\lambda|r_1-r_2|}}{|r_1-r_2|}, \tag{A.50}$$

writing the $q = -k^{'} + k$ and $r_{12} = r$ the integral yields,

$$I = \int d^3 r e^{-iq\cdot r} \frac{e^{-\lambda|r|}}{|r|}, \tag{A.51}$$

$$I = \int d\phi \int d(\cos\theta) \int dr r^2 e^{-iq\cdot r} \frac{e^{-\lambda|r|}}{|r|}, \tag{A.52}$$

$$I = 2\pi \int dr r e^{-\lambda|r|} \int d(\cos\theta) e^{-iqr\cos\theta}, \tag{A.53}$$

$$I = 2\pi \int dr r e^{-\lambda|r|} \frac{1}{iqr} \left[e^{iqr} - e^{-iqr} \right], \tag{A.54}$$

$$I = \frac{2\pi}{iq} \left[\int dr e^{(-\lambda+iq)|r|} - e^{(-\lambda-iq)|r|} \right], \tag{A.55}$$

$$I = \frac{2\pi}{iq} \left[\frac{1}{(-\lambda+iq)} - \frac{1}{(-\lambda-iq)} \right], \tag{A.56}$$

$$I = \frac{2\pi}{iq} \left[\frac{(-\lambda-iq) - (-\lambda+iq)}{\lambda^2+q^2} \right], \tag{A.57}$$

$$I = -\frac{4\pi}{\lambda^2+q^2}. \tag{A.58}$$

The matrix element can be written as,

$$\begin{aligned} M_t &= -\frac{e^2}{\epsilon\epsilon_0 V^{3/2}} \frac{\alpha_v^{3/2}}{\sqrt{\pi}} F_{k''v} F_{k'k} \frac{1}{(q^2+\lambda^2)} \\ &\times \int d^3 r_1 e^{-i(k^{''}+k^{'}-k)\cdot r_1} e^{-\alpha_v|r_1|}, \end{aligned} \tag{A.59}$$

$$\begin{aligned} M_t &= -\frac{e^2}{\epsilon\epsilon_0 V^{3/2}} \frac{\alpha_v^{3/2}}{\sqrt{\pi}} F_{k''v} F_{k'k} \frac{1}{(q^2+\lambda^2)} \\ &\times \int d^3 r_1 e^{-i(k^{''}-(k-k^{'}))\cdot r_1} e^{-\alpha_v|r_1|} \end{aligned} \tag{A.60}$$

$$\begin{aligned} M_t &= -\frac{e^2}{\epsilon\epsilon_0 V^{3/2}} \frac{\alpha_v^{3/2}}{\sqrt{\pi}} F_{k''v} F_{k'k} \frac{1}{(q^2+\lambda^2)} \\ &\times \int d^3 r_1 e^{-i(k^{''}-q)\cdot r_1} e^{-\alpha_v|r_1|} \end{aligned} \tag{A.61}$$

writting $q^{'} = k^{''} - q$ the matrix element yields,

$$\begin{aligned} M_t &= -\frac{e^2}{\epsilon\epsilon_0 V^{3/2}}\frac{\alpha_v^{3/2}}{\sqrt{\pi}}F_{k''v}F_{k'k}\frac{1}{(q^2+\lambda^2)} \\ &\times \int d^3r_1 e^{-iq^{'}\cdot r_1}e^{-\alpha_v|r_1|} \end{aligned} \tag{A.62}$$

The solution of the second integral can be found as,

$$II \equiv \int d^3r_1 e^{-iq^{'}r_1\cos\theta}e^{-\alpha_v|r_1|}, \tag{A.63}$$

$$II = \int d\phi \int d(\cos\theta) \int r_1^2 dr_1 e^{-iq^{'}r_1\cos\theta}e^{-\alpha_v|r_1|}, \tag{A.64}$$

$$II = 2\pi \int r_1^2 dr_1 e^{-\alpha_v|r_1|} \int d(\cos\theta) e^{-iq^{'}r_1\cos\theta}, \tag{A.65}$$

$$II = 2\pi \int r_1^2 dr_1 e^{-\alpha_v|r_1|}\frac{2\pi}{iq^{'}r_1}\left[e^{iq^{'}r_1} - e^{-iq^{'}r_1}\right], \tag{A.66}$$

$$II = \frac{2\pi}{iq^{'}}\int r_1 dr_1 \left[e^{(-\alpha_v+iq^{'})|r_1|} - e^{(-\alpha_v-iq^{'})|r_1|}\right], \tag{A.67}$$

$$II = \frac{2\pi}{iq^{'}}\left[\frac{1}{(\alpha_v+iq^{'})^2} - \frac{1}{(\alpha_v-iq^{'})^2}\right], \tag{A.68}$$

$$II = \frac{2\pi}{iq^{'}}\left[\frac{(\alpha_v^2 - q^{'2} + 2i\alpha_v q^{'}) - (\alpha_v^2 - q^{'2} - 2i\alpha_v q^{'})}{(\alpha_v^2 + q^{'2})^2}\right], \tag{A.69}$$

$$II = \frac{2\pi}{iq^{'}}\frac{4i\alpha_v q^{'}}{(q^{'2}+\alpha_v^2)^2} \tag{A.70}$$

$$II = \frac{8\pi\alpha_v}{(q^{'2}+\alpha_v^2)^2}. \tag{A.71}$$

As a result the matrix element becomes

$$M_t = -\frac{e^2}{\epsilon\epsilon_0 V^{3/2}}\frac{\alpha_v^{5/2}}{\sqrt{\pi}}F_{k''v}F_{k'k}\frac{1}{(q^2+\lambda^2)}\frac{8\pi}{(q^{'2}+\alpha_v^2)^2}, \tag{A.72}$$

and the square of it,

$$|M_t|^2 = \left[\frac{e^2}{\epsilon\epsilon_0 V}\right]^2 \frac{64\pi}{V}|F_{k''v}|^2|F_{k'k}|^2\frac{1}{(q^2+\lambda^2)^2}\frac{1}{(q'^2+\alpha_v^2)^4}\alpha_v^5. \tag{A.73}$$

Now, we can write the probability equation as,

$$P_{ii}^{(t)}(k) = \sum_{k'}\sum_{k''}\sum_{imp.}\frac{2\pi}{\hbar}|M_t|^2\delta[\frac{\hbar^2k'^2}{2m}+\frac{\hbar^2k''^2}{2m}+\frac{\hbar^2\alpha_v^2}{2m}-\frac{\hbar^2k^2}{2m}], \tag{A.74}$$

$$\sum_{imp.} = P_{NC}V, \tag{A.75}$$

$$\begin{aligned} P_{ii}^{(t)}(k) &= \frac{2\pi}{\hbar}\frac{2m}{\hbar^2}\left[\frac{e^2}{\epsilon\epsilon_0 V}\right]^2\frac{|F_{k''v}|^2|F_{k'k}|^2 64\pi\alpha_v^5}{V}P_{NC}V\frac{V}{(2\pi)^3}\frac{V}{(2\pi)^3}\int d^3k' \\ &\times \int d^3k''\frac{1}{(q^2+\lambda^2)^2}\frac{1}{(q'^2+\alpha_v^2)^4}\delta[k''^2+k'^2+\alpha_v^2-k^2], \end{aligned} \tag{A.76}$$

$$if \quad \tau^{-1} = \tfrac{1}{\pi}|F_{k''v}|^2|F_{k'k}|^2\left[\tfrac{e^2m^{1/2}}{\epsilon\epsilon_0\hbar^{3/2}}\right]^2 \tag{A.77}$$

$$\begin{aligned} P_{ii}^{(t)}(k) &= \tau^{-1}\frac{4P_{NC}\alpha_v^5}{\pi^3}\int d^3k'\int d^3k''\frac{1}{(q^2+\lambda^2)^2}\frac{1}{(q'^2+\alpha_v^2)^4} \\ &\times\delta[k''^2+k'^2+\alpha_v^2-k^2], \end{aligned} \tag{A.78}$$

if $q = k - k'$ $d^3q = -d^3k'$

$$\begin{aligned} P_{ii}^{(t)}(k) &= \tau^{-1}\frac{4P_{NC}\alpha_v^5}{\pi^3}\int d^3q\int d^3k''\frac{1}{(q^2+\lambda^2)^2}\frac{1}{(q'^2+\alpha_v^2)^4} \\ &\times\ \delta[k''^2+k^2+q^2-2k\cdot q+\alpha_v^2-k^2], \end{aligned} \tag{A.79}$$

$$\begin{aligned} P_{ii}^{(t)}(k) &= \tau^{-1}\frac{4P_{NC}\alpha_v^5}{\pi^3}(2\pi)^2\int q^2dq\frac{1}{(q^2+\lambda^2)^2}\int dx\int dx''\int k''^2dk'' \\ &\times\ \frac{1}{(k''^2+q^2-2k''\cdot q+\alpha_v^2)^4}\delta[k''^2+k^2+q^2-2k\cdot q+\alpha_v^2-k^2], \end{aligned} \tag{A.80}$$

$$\begin{aligned} P_{ii}^{(t)}(k) &= \tau^{-1}\frac{16P_{NC}\alpha_v^5}{\pi}\int q^2dq\frac{1}{(q^2+\lambda^2)^2}\int dx\int dx''\int k''^2dk'' \\ &\times\ \frac{1}{(k''^2+q^2-2k''qx''+\alpha_v^2)^4}\delta[k''^2+k^2+q^2-2kqx+\alpha_v^2-k^2], \end{aligned} \tag{A.81}$$

if $q \rightarrow \frac{q}{\alpha_v}$ and $k'' \rightarrow \frac{k''}{\alpha_v}$

$$\begin{aligned} P_{ii}^{(t)}(k) &= \tau^{-1}\frac{16P_{NC}\alpha_v^5}{\pi}\int \alpha_v^2 q^2 \alpha_v dq \frac{1}{\alpha_v^4[(q^2+(\lambda/\alpha_v)^2)^2]}\int dx \int dx'' \int dk'' \\ &\times \alpha_v^2 k''^2 \alpha_v \frac{1}{\alpha_v^8[(k''^2+q^2-2k''qx''+1)^4]}\frac{1}{\alpha_v^2}\delta[k''^2+q^2-2(kq/\alpha_v)x+1], \end{aligned} \tag{A.82}$$

$$\begin{aligned} P_{ii}^{(t)}(k) &= \tau^{-1}\frac{16P_{NC}}{\pi\alpha_v^3}\int q^2 dq \frac{1}{[q^2+(\lambda/\alpha_v)^2]^2}\int dx \int dx'' \int k''^2 dk'' \\ &\times \frac{1}{(k''^2+q^2-2k''qx''+1)^4}\delta[k''^2+q^2-2(kq/\alpha_v)x+1], \end{aligned} \tag{A.83}$$

$$\begin{aligned} P_{ii}^{(t)}(k) &= \tau^{-1}\frac{16P_{NC}}{\pi\alpha_v^3}\int q^2 dq \frac{1}{[q^2+(\lambda/\alpha_v)^2]^2}\int dx \int dx'' \\ &\times \int k''^2 dk'' \frac{1}{(k''^2+q^2-2k''qx''+1)^4}\frac{1}{2\sqrt{-q^2+2(kq/\alpha_v)x-1}} \\ &\times \delta[k''-\sqrt{-q^2+2(kq/\alpha_v)x-1}], \end{aligned} \tag{A.84}$$

if $B = \sqrt{-q^2+2(kq/\alpha_v)x-1}$

$$P_{ii}^{(t)}(k) = \tau^{-1}\frac{8P_{NC}}{\pi\alpha_v^3}\int q^2 dq \frac{1}{[q^2+(\lambda/\alpha_v)^2]^2}\int dx \int dx'' B^2 \frac{1}{(B^2+q^2-2Bqx''+1)^4}\frac{1}{B}, \tag{A.85}$$

$$P_{ii}^{(t)}(k) = \tau^{-1}\frac{8P_{NC}}{\pi\alpha_v^3}\int q^2 dq \frac{1}{[q^2+(\lambda/\alpha_v)^2]^2}\int dx \int dx'' \frac{B}{(B^2+q^2-2Bqx''+1)^4}, \tag{A.86}$$

$$P_{ii}^{(t)}(k) = \tau^{-1}\frac{8P_{NC}}{\pi\alpha_v^3}\int q^2 dq \frac{1}{[q^2+(\lambda/\alpha_v)^2]^2}\int dx \left[\frac{B}{6q(B^2+q^2-2Bqx''+1)^3}\right]_{1-}^{1}, \tag{A.87}$$

$$\begin{aligned} P_{ii}^{(t)}(k) &= \tau^{-1}\frac{8P_{NC}}{\pi\alpha_v^3}\int q^2 dq \frac{1}{[q^2+(\lambda/\alpha_v)^2]^2} \\ &\times \int dx \left[\frac{B}{6q(B^2+q^2-2Bqx''+1)^3}-\frac{B}{6q(B^2+q^2+2Bqx''+1)^3}\right], \end{aligned} \tag{A.88}$$

$B^2 = -q^2 - 1 + \frac{2kq}{\alpha_v}x$ and $dx = \frac{\alpha_v dB}{kq}$

$$\begin{aligned} P_{ii}^{(t)}(k) &= \tau^{-1}\frac{8P_{NC}}{\pi\alpha_v^2 k}\int qdq\frac{1}{[q^2+(\lambda/\alpha_v)^2]^2} \\ &\times \int dB\left[\frac{B^2}{6q(B^2+q^2-2Bqx''+1)^3} - \frac{B^2}{6q(B^2+q^2+2Bqx''+1)^3}\right], \end{aligned} \tag{A.89}$$

$$\begin{aligned} P_{ii}^{(t)}(k) &= \tau^{-1}\frac{8P_{NC}}{\pi\alpha_v^2 k}\int qdq\frac{1}{[q^2+(\lambda/\alpha_v)^2]^2} \\ &\times \frac{1}{48q}\left[\frac{2(-1+Bq-q^2)}{(1+B^2-2Bq+q^2)^2} + \frac{3(B-q)q}{1+B^2-2Bq+q^2} + \frac{2(1+Bq+q^2)}{(1+B^2+2Bq+q^2)^2}\right. \\ &+ \left.\frac{3(B+q)q}{1+B^2+2Bq+q^2} + 3q\arctan(B+q) + 3q\arctan(B-q)\right], \end{aligned} \tag{A.90}$$

If $C^2 = B^2 + q^2 + 1$

$$\begin{aligned} P_{ii}^{(t)}(k) &= \tau^{-1}\frac{8P_{NC}}{\pi\alpha_v^2 k}\int qdq\frac{1}{[q^2+(\lambda/\alpha_v)^2]^2} \\ &\times \left[\frac{1}{48q}\left(\frac{2(-1+Bq-q^2)}{(C^2-2Bq)^2} + \frac{3(B-q)q}{C^2-2Bq} + \frac{2(1+Bq+q^2)}{(C^2+2Bq)^2}\right)\right. \\ &+ \left.\frac{1}{48q}\left(\frac{3(B+q)q}{C^2+2Bq} + 3q\arctan(B+q) + 3q\arctan(B-q)\right)\right], \end{aligned} \tag{A.91}$$

$$\begin{aligned} P_{ii}^{(t)}(k) &= \tau^{-1}\frac{8P_{NC}}{\pi\alpha_v^2 k}\int qdq\frac{1}{[q^2+(\lambda/\alpha_v)^2]^2} \\ &\times \left[\frac{1}{48q}\frac{2(-1+Bq-q^2)(C^2+2Bq)^2 + 2(1+Bq+q^2)(C^2-2Bq)^2}{(C^2-2Bq)^2(C^2+2Bq)^2}\right. \\ &+ \frac{1}{48q}\frac{(3(B-q)q)(C^2+2Bq) + (3(B+q)q)(C^2-2Bq)}{(C^2+2Bq)(C^2-2Bq)} \\ &+ \left.\frac{1}{48q}\left(3q\arctan(B+q) + 3q\arctan(B-q)\right)\right], \end{aligned} \tag{A.92}$$

$$\begin{aligned} P_{ii}^{(t)}(k) &= \tau^{-1}\frac{8P_{NC}}{\pi\alpha_v^2 k}\int qdq\frac{1}{[q^2+(\lambda/\alpha_v)^2]^2} \\ &\times \left[\frac{1}{48q}\left(\frac{4Bq(C^4+4B^2q^2-4C^2-4C^2q^2)}{(C^4-4B^2q^2)^2} + \frac{(3Bq(2C^2-4q^2)}{(C^4+4B^2q^2)}\right)\right. \\ &+ \left.\frac{1}{48q}\left(3q\arctan(B+q) + 3q\arctan(B-q)\right)\right], \end{aligned} \tag{A.93}$$

$$\begin{aligned}
P_{ii}^{(t)}(k) &= \tau^{-1}\frac{8P_{NC}}{\pi\alpha_v^2 k}\int qdq\frac{1}{[q^2+(\lambda/\alpha_v)^2]^2} \\
&\times \frac{2}{48}\left[\frac{B}{(C^4-4B^2q^2)}\left(\frac{2(C^4+4B^2q^2-4C^2-4C^2q^2)}{(C^4-4B^2q^2)}+(3C^2-6q^2)\right)\right. \\
&+ \left.\frac{3}{2}\arctan(B+q)+\frac{3}{2}\arctan(B-q)\right], \qquad \text{(A.94)}
\end{aligned}$$

The final probability equation can be written as,

$$\begin{aligned}
P_{ii}^{(t)}(k) &= \tau^{-1}\frac{P_{NC}}{3\pi\alpha_v^2 k}\int dq\frac{q}{[q^2+(\lambda/\alpha_v)^2]^2} \\
&\times \left\{\frac{B}{(C^4-4B^2q^2)}\left[2\frac{(C^4+4B^2q^2-4C^2(q^2+1))}{(C^4-4B^2q^2)}+(3C^2-6q^2)\right]\right. \\
&+ \left.\frac{3}{2}(\arctan(B+q)+\arctan(B-q))\right\}. \qquad \text{(A.95)}
\end{aligned}$$

We can also express this probability as,

$$P_{ii}^{(t)}(k) = \tau^{-1}\frac{P_{NC}}{3\pi\alpha_v^2 k}\int dq\frac{q}{[q^2+(\lambda/\alpha_v)^2]^2}h(q), \qquad \text{(A.96)}$$

then $h(q)$ is

$$\begin{aligned}
h(q) &= \frac{B}{(C^4-4B^2q^2)}\left[2\frac{(C^4+4B^2q^2-4C^2(q^2+1))}{(C^4-4B^2q^2)}+(3C^2-6q^2)\right] \\
&+ \frac{3}{2}(\arctan(B+q)+\arctan(B-q)). \qquad \text{(A.97)}
\end{aligned}$$

A.0.3 Direct Tunnelling

Changing the α_v with α_c in Eq. A.96 we can easily obtain the probability of the direct tunnelling process(cf. Fig. A.1 (c)) as

$$P_{ii}^{(t)}(k) = \tau^{-1}\frac{P_{NC}}{3\pi\alpha_c^2 k}\int dq\frac{q}{[q^2+(\lambda/\alpha_c)^2]^2}h(q), \qquad \text{(A.98)}$$

where $h(q)$ is given by

$$\begin{aligned}
h(q) &= \frac{B}{(C^4-4B^2q^2)}\left[2\frac{(C^4+4B^2q^2-4C^2(q^2+1))}{(C^4-4B^2q^2)}+(3C^2-6q^2)\right] \\
&+ \frac{3}{2}(\arctan(B+q)+\arctan(B-q)). \qquad \text{(A.99)}
\end{aligned}$$

Appendix B

Theoretical Details on Auger Recombination and Carrier Multiplication

In this appendix, for documentation purposes we would like to provide some background information and further technical details on the Auger recombination and carrier multiplication.

B.0.4 Auger Recombination in Bulk Systems

Before starting the explanation and clarification of method used to calculate the Auger recombination (AR) and carrier multiplication (CM) (inverse AR) rate in NCs it would be more worthwhile to examine AR in bulk systems. Simply, AR involves three particles: an electron and a hole, which recombine in a band-to-band transition and give off the resulting energy to another electron or hole. In high purity bulk materials only the direct processes (see Fig. B.1) are of significance.

The matrix element M_{12} for the scattering in the direct process is

$$M_{12} = \frac{1}{V^2}\int\int u^*_{v\mathbf{k}'_1}(\mathbf{r_1})e^{-i\mathbf{k}'_1\cdot\mathbf{r_1}}u^*_{c\mathbf{k}'_2}(\mathbf{r_2})e^{-i\mathbf{k}'_2\cdot\mathbf{r_2}}V_c(|\mathbf{r_1}-\mathbf{r_2}|)u_{c\mathbf{k_1}}(\mathbf{r_1})$$

$$
\begin{aligned}
& \times \quad e^{-i\mathbf{k_1}\cdot\mathbf{r_1}} u_{c\mathbf{k_2}}(\mathbf{r_2}) e^{-i\mathbf{k_2}\cdot\mathbf{r_2}} d^3r_1 d^3r_2 && \text{(B.1)} \\
M_{21} \; = \; & \frac{1}{V^2} \int\int u^*_{v\mathbf{k}'_1}(\mathbf{r_2}) e^{-i\mathbf{k}'_1\cdot\mathbf{r_2}} u^*_{c\mathbf{k}'_2}(\mathbf{r_1}) e^{-i\mathbf{k}'_2\cdot\mathbf{r_1}} V_c(|\mathbf{r_1}-\mathbf{r_2}|) u_{c\mathbf{k_1}}(\mathbf{r_1}) && \\
& \times \quad e^{-i\mathbf{k_1}\cdot\mathbf{r_1}} u_{c\mathbf{k_2}}(\mathbf{r_2}) e^{-i\mathbf{k_2}\cdot\mathbf{r_2}} d^3r_1 d^3r_2 && \text{(B.2)}
\end{aligned}
$$

The integration of the planewave of the wavefunctions leads to a momentum conservation; this constraint reduces the AR and CM in *bulk* systems.

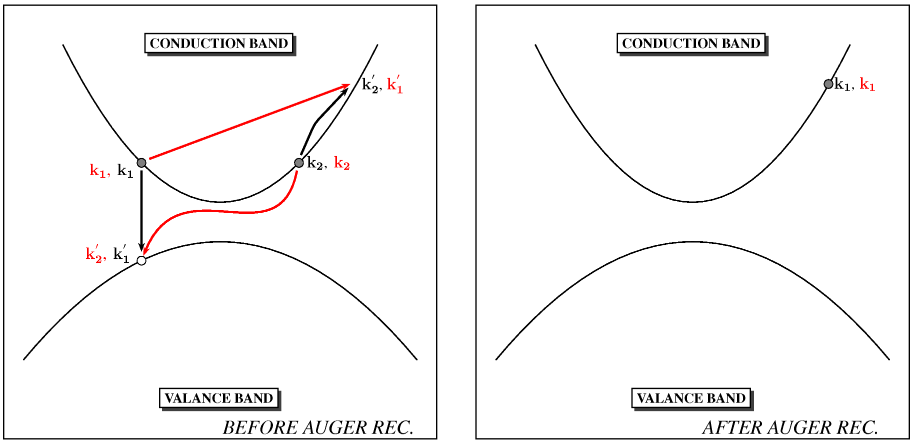

Figure B.1: A schematic of the Auger Recombination in Bulk Semiconductors.

In quantum mechanics there is an important distinction when scattering occurs between identical particles or distinguishable particles.

- If the particles are distinguishable the total matrix element is

$$|M|^2 = |M_{12}|^2 + |M_{21}|^2, \tag{B.3}$$

- If the particles are indistinguishable and are bosons (e.g. α-particles, photons, mesons) then the total matrix element is

$$|M|^2 = |M_{12} + M_{21}|^2, \tag{B.4}$$

- If the particles are indistinguishable but are fermions (e.g. electrons, neutrinos, protons, neutrons) the total matrix element is

$$|M|^2 = |M_{12} - M_{21}|^2. \tag{B.5}$$

We can essentially use the above formalism and apply it to the AR case. There are four processes and two of them are totally indistinguishable (initial electrons have the same spins) and two of them are distinguishable (initial electrons have the opposite spins). One has to square and add the contributions separately. The total matrix element becomes

$$|M|^2 = \left[|M_{12}|^2 + |M_{21}|^2 + |M_{12} - M_{21}|^2\right] \tag{B.6}$$

During the calculation of AR, we must take into account the occupation statistics of the various electrons and hole states involved in. For example in the Auger case, we need to weight the rate with the probability that states $\mathbf{k_2}$ is full, $\mathbf{k_1}'$ is empty and $\mathbf{k_1}$ is full. In general we have to use the Fermi-Dirac function to describe the occupation.

B.0.5 Theory of Auger Process in Nanocrystals

After solving the atomistic empirical pseudopotential Hamiltonian for the energy levels and the wave functions, the AR and CM probability can be extracted using the Fermi's golden rule,

$$W = \frac{1}{\tau} = \frac{2\pi}{\hbar} \sum_{fin} |\langle \mathrm{in}|\Delta H|\mathrm{fin}\rangle|^2 \delta(\Delta E). \tag{B.7}$$

We consider Auger final states with a finite lifetime $\hbar/\Gamma$ [thus evolving with time as $\Phi_f e^{-i\omega t - \Gamma t/2\hbar}$] to account for these interactions, which may cause their decay into lower energy states. We derive a phenomenological formula for the Auger rate (under standard time-dependent perturbation theory):

$$\mathrm{Im}\left\{\frac{1}{\pi}\frac{1}{x - i(\Gamma/2)}\right\} = \delta(x) \tag{B.8}$$

and using this identity Eq. B.7 yields

$$W = \frac{1}{\tau} = \frac{\Gamma}{\hbar} \sum_n \frac{|\langle n|\Delta H|i\rangle|^2}{(E_{f_n} - E_i)^2 + (\Gamma/2)^2} \tag{B.9}$$

where $|i\rangle$ and $|f\rangle$ are the initial and final Auger electronic state, E_f and E_i are their eigenenergies, Γ is the broadening parameter of the energy and ΔH is the

Coulomb interaction. In Eq. B.9, we have used multiple final states $\{n\}$ (where n includes spin as well), since each final state might have some contribution to the Auger rate $W = 1/\tau$.

Now we use τ_e (Conduction Type in Fig. 5.1 (a)) the Auger lifetime for the process of exciton + electron → electron, and with τ_h (Valence Type in Fig. 5.1 (b)) the process of exciton + hole → hole. To calculate the τ_e (τ_h), we must write the Slater determinant of the initial and final states. If two initial electrons (holes) have identical spin (indistinguishable) initial and final states can be written by using the Slater determinant

$$\Phi_{in} = \frac{1}{\sqrt{2}} \begin{vmatrix} \phi_i(\mathbf{r_1}, \sigma_i) & \phi_i(\mathbf{r_2}, \sigma_i) \\ \phi_j(\mathbf{r_1}, \sigma_j) & \phi_j(\mathbf{r_2}, \sigma_j) \end{vmatrix}, \Phi_{fin} = \frac{1}{\sqrt{2}} \begin{vmatrix} \phi_k(\mathbf{r_1}, \sigma_k) & \phi_k(\mathbf{r_2}, \sigma_k) \\ \phi_l(\mathbf{r_1}, \sigma_l) & \phi_l(\mathbf{r_2}, \sigma_l) \end{vmatrix},$$

and the Auger matrix element $|\langle \mathrm{in}|\Delta H|\mathrm{fin}\rangle|$ can be calculated as

$$\begin{aligned} M_I(i,j,k,l) &= \Big\langle \frac{1}{\sqrt{2}}(\phi_i(\mathbf{r_1},\sigma_i)\phi_j(\mathbf{r_2},\sigma_j) - \phi_j(\mathbf{r_1},\sigma_j)\phi_i(\mathbf{r_2},\sigma_i))\, |V(\mathbf{r_1}-\mathbf{r_2})| \\ &\quad \frac{1}{\sqrt{2}}(\phi_k(\mathbf{r_1},\sigma_k)\phi_l(\mathbf{r_2},\sigma_l) - \phi_l(\mathbf{r_1},\sigma_l)\phi_k(\mathbf{r_2},\sigma_k)) \Big\rangle\, \delta_{\sigma_i,\sigma_j}, \end{aligned} \tag{B.10}$$

and Eq. B.10 is equal to

$$\begin{aligned} M_I(i,j,k,l) = &+ \frac{1}{2}\langle \phi_i(\mathbf{r_1},\sigma_i)\phi_j(\mathbf{r_2},\sigma_j)|\, V_c(\mathbf{r_1}-\mathbf{r_2})\, |\phi_k(\mathbf{r_1},\sigma_k)\phi_l(\mathbf{r_2},\sigma_l)\rangle\, \delta_{\sigma_i,\sigma_j} \\ &- \frac{1}{2}\langle \phi_i(\mathbf{r_1},\sigma_i)\phi_j(\mathbf{r_2},\sigma_j)|\, V_c(\mathbf{r_1}-\mathbf{r_2})\, |\phi_l(\mathbf{r_1},\sigma_l)\phi_k(\mathbf{r_2},\sigma_k)\rangle\, \delta_{\sigma_i,\sigma_j} \\ &- \frac{1}{2}\langle \phi_j(\mathbf{r_1},\sigma_j)\phi_i(\mathbf{r_2},\sigma_i)|\, V_c(\mathbf{r_1}-\mathbf{r_2})\, |\phi_k(\mathbf{r_1},\sigma_k)\phi_l(\mathbf{r_2},\sigma_l)\rangle\, \delta_{\sigma_i,\sigma_j} \\ &+ \frac{1}{2}\langle \phi_j(\mathbf{r_1},\sigma_j)\phi_i(\mathbf{r_2},\sigma_i)|\, V_c(\mathbf{r_1}-\mathbf{r_2})\, |\phi_l(\mathbf{r_1},\sigma_l)\phi_k(\mathbf{r_2},\sigma_k)\rangle\, \delta_{\sigma_i,\sigma_j}, \end{aligned} \tag{B.11}$$

here Eq. B.11 can be simplified by changing the $r_1 \Longleftrightarrow r_2$ in the the third and fourth terms, yielding

$$\begin{aligned} M_I(i,j,k,l) = &+ \langle \phi_i(\mathbf{r_1},\sigma_i)\phi_j(\mathbf{r_2},\sigma_j)|\, V_c(\mathbf{r_1}-\mathbf{r_2})\, |\phi_k(\mathbf{r_1},\sigma_k)\phi_l(\mathbf{r_2},\sigma_l)\rangle\, \delta_{\sigma_i,\sigma_j} \\ &- \langle \phi_j(\mathbf{r_1},\sigma_j)\phi_i(\mathbf{r_2},\sigma_i)|\, V_c(\mathbf{r_1}-\mathbf{r_2})\, |\phi_k(\mathbf{r_1},\sigma_k)\phi_l(\mathbf{r_2},\sigma_l)\rangle\, \delta_{\sigma_i,\sigma_j}. \end{aligned} \tag{B.12}$$

Coulomb interaction doesnot change the spin of the particles so Eq. B.12 is equal to

$$\begin{aligned} M_I(i,j,k,l) = & + \langle \phi_i(\mathbf{r_1},\sigma_i)\phi_j(\mathbf{r_2},\sigma_j)|\, V_c(\mathbf{r_1}-\mathbf{r_2})\, |\phi_k(\mathbf{r_1},\sigma_k)\phi_l(\mathbf{r_2},\sigma_l)\rangle\, \delta_{\sigma_i,\sigma_j}\delta_{\sigma_i,\sigma_k}\delta_{\sigma_j,\sigma_l} \\ & - \langle \phi_j(\mathbf{r_1},\sigma_j)\phi_i(\mathbf{r_2},\sigma_i)|\, V_c(\mathbf{r_1}-\mathbf{r_2})\, |\phi_k(\mathbf{r_1},\sigma_k)\phi_l(\mathbf{r_2},\sigma_l)\rangle\, \delta_{\sigma_i,\sigma_j}\delta_{\sigma_i,\sigma_l}\delta_{\sigma_j,\sigma_k}. \end{aligned} \tag{B.13}$$

If two initial electrons (holes) have opposite spin (distinguishable), initial and final states can be written as

$$\Phi_{in} = \phi_i(\mathbf{r_1},\sigma_i)\phi_j(\mathbf{r_2},\sigma_j), \Phi_{fin} = \phi_k(\mathbf{r_1},\sigma_l)\phi_l(\mathbf{r_2},\sigma_k),$$

and the Auger matrix element $|\langle \text{in}|\Delta H|\text{fin}\rangle|$

$$M_D(i,j,k,l) = \langle(\phi_i(\mathbf{r_1},\sigma_i)\phi_j(\mathbf{r_2},\sigma_j)|\, V_c(\mathbf{r_1}-\mathbf{r_2})\, |(\phi_k(\mathbf{r_1},\sigma_l)\phi_k(\mathbf{r_2},\sigma_l)\rangle\, (1-\delta_{\sigma_i,\sigma_j}) \\ . \tag{B.14}$$

Similarly, Eq. B.14 is equal to

$$M_D(i,j,k,l) = \langle(\phi_i(\mathbf{r_1},\sigma_i)\phi_j(\mathbf{r_2},\sigma_j)|\, V_c(\mathbf{r_1}-\mathbf{r_2})\, |(\phi_k(\mathbf{r_1},\sigma_l)\phi_k(\mathbf{r_2},\sigma_l)\rangle\, (1-\delta_{\sigma_i,\sigma_j})\delta_{\sigma_i,\sigma_k}\delta_{\sigma_j,\sigma_l}. \tag{B.15}$$

For completeness, the spin-conserving screened Coulomb potential is given by

$$V_c(\mathbf{r_1},\mathbf{r_2}) = \frac{e^2}{\epsilon(\mathbf{r_1},\mathbf{r_2})|\mathbf{r_1}-\mathbf{r_2}|}, \tag{B.16}$$

here, the dielectric function $\epsilon(\mathbf{r_1},\mathbf{r_2})$ requires some special attention. The subject of the correct screened Coulomb interaction for NCs has been the center of discussion within the past decade. A number of researchers [161, 162, 163, 164] have reported the average dielectric constant of a quantum dot or NC to be smaller than the bulk case and linked the cause of this reduction to increase in energy gap in NC. However, further theoretical investigations [156, 165, 160, 149, 166] have concluded that dielectric constant of the NC is bulklike inside. On the basis of these reports, we use as the dielectric function [149]

$$\frac{1}{\epsilon(\mathbf{r_1},\mathbf{r_2})} = \frac{1}{\epsilon_{\text{out}}} + \left(\frac{1}{\epsilon_{\text{in}}} - \frac{1}{\epsilon_{\text{out}}}\right) m(\mathbf{r_1})m(\mathbf{r_2}), \tag{B.17}$$

where, the so-called mask function $m(\mathbf{r})$ is set to 1 when $\mathbf{r}$ inside of the NC and 0 when $\mathbf{r}$ outside of the NC.

Using the matrix elements M_I and M_D, we can write the total rate expression as,

$$W(i,j,k) \quad = \tfrac{\Gamma}{\hbar}\sum_{l} \frac{|M_I(i,j;k,l)|^2 + |M_D(j,i;k,l) + M_D(i,j;k,l)|^2}{(\Delta E)^2 + (\Gamma/2)^2}, \tag{B.18}$$

where the sum l run over the spin ↑, ↓ of the electron as well.

For $T \neq 0$, we take a Boltzmann average over the one of the initial electron and initial hole state. For example, in the case of the Conduction Type Recombination (see Fig.5.1 (a)), we take the average over all initial electronic (i) and initial hole (k) states with the probability ($e^{-(E_i - E_{\text{LUMO}})/k_BT}$ for conduction and $e^{-(E_{\text{HOMO}} - E_k)/k_BT}$ for valance) grater than the 1/20.

$$\frac{1}{\tau} = \frac{\sum\limits_{i,k} W(i,j,k) e^{-(E_i - E_{\text{LUMO}})/k_BT} e^{-(E_{\text{HOMO}} - E_k)/k_BT}}{\sum\limits_{i,k} e^{-(E_i - E_{\text{LUMO}})/k_BT} e^{-(E_{\text{HOMO}} - E_k)/k_BT}} \tag{B.19}$$

Because of the huge number of the possible transitions (it requires excessive simulation time), the other initial electron is kept fixed at LUMO. For this initial state we did not take the average over the spin, because our wavefunctions do not depend on it. The rate equation reduces

$$\frac{1}{\tau} = \frac{\sum\limits_{i,k} W(i,lumo,k) e^{-(E_i - E_{\text{LUMO}})/k_BT} e^{-(E_{\text{HOMO}} - E_k)/k_BT}}{\sum\limits_{i,k} e^{-(E_i - E_{\text{LUMO}})/k_BT} e^{-(E_{\text{HOMO}} - E_k)/k_BT}} \tag{B.20}$$

where lumo is valence band top state.

Biexciton types of AR shown in Fig. 5.1 (c) and (d) becomes particularly important under high carrier densities such as in NC lasers. Its probability can be expressed in terms of EE and EH type AR as [149],

$$\frac{1}{\tau_{\text{XX}}} = \frac{2}{\tau_{\text{EE}}} + \frac{2}{\tau_{\text{EH}}} \tag{B.21}$$

where τ_{EE} and τ_{EH} are EE and EH lifetimes.

Almost the same formalism applies to the carrier multiplication, hence it will not be repeated.